UNIVERSITÀ DI PARMA

UNIVERSITA' DEGLI STUDI DI PARMA

DOTTORATO DI RICERCA IN

Fisica

CICLO XXXVI

A correlative and multimodal microscopy approach to study the interaction of photosensitizers with biological samples

Coordinatore:
Chiar.mo Prof. Stefano Carretta

Tutori:
Chiar.mo Prof. Cristiano Viappiani
Chiar.mo Dott. Paolo Bianchini

Dottorando: Matteo Mariangeli

Anni Accademici 2020/2021 – 2022/2023

"...L'amore è l'unica cosa che riusciamo a percepire che trascenda le dimensioni di tempo e spazio."

A mia nonna Ivana

Contents

Introduction

Over the past century, significant medical advancements have greatly enhanced people's quality of life. Key developments include Alexander Fleming's discovery of antibiotics in 1928, pivotal in combating bacterial infections; the advent of chemotherapeutic agents as vital tools against cancer; and the ongoing effectiveness of vaccines in preventing or eradicating deadly viral diseases. However, these techniques have their limitations. For example, the overuse of antibiotics in recent decades has led to a surge in antibiotic-resistant bacteria, a major health concern today. Chemotherapy's lack of selectivity, harming both cancerous and healthy cells, remains a challenge for its efficacy and tolerance. Despite their efficiency against deadly viruses, including emerging ones like SARS-CoV-2, vaccines face challenges in production and don't always provide complete protection against pathogens.

In the last 30 years, new medical strategies have been developed to combat pathogens and cancer cells, either as standalone treatments or as adjuncts to established therapies. One such method is Photodynamic Therapy (PDT), which uses light and photosensitive molecules to target specific areas.

Antimicrobial PDT is advantageous with respect to traditional antimicrobials because it doesn’t rely on a singular action mechanism, reducing the risk of pathogen resistance. Common antimicrobials, with their single action mechanism and unregulated use, often contribute to resistant strain proliferation.

PDT's indiscriminate targeting also simplifies application, as it doesn't require an in-depth understanding of the microorganism's biology. This makes it a quicker, more versatile option against various pathogens, including emerging ones. Despite these benefits, the medical community remains cautious about using PDT against pathogenic microorganisms, even though it's a clinically approved cancer treatment. Consequently, funding and basic research in this area are limited, raising questions about hesitancy towards this approach [1].

The work of this thesis is framed in this context: many advanced microscopic and spectroscopic techniques were applied to understand how a photosensitizer works in physiological environments. We focused on photodynamic inactivation of viruses, a topic of heightened relevance in recent years, as seen in the fight against HIV, MERS, and SARS viruses. These viruses belong to the class of **Enveloped viruses**; hence they share a common feature: a phospholipidic envelope crucial for their protection and replication. Our research focused on characterizing the effects of **Hypericin,** a promising and versatile photosensitizer known to be effective against some enveloped viruses [2], on **SARS-CoV-2** and on specially designed **model membranes** that simulate the virus's envelope.

The **PART 1** of this work will be devoted to providing some general theoretical insights. This section will cover aspects of PDT and offer some details about Hypericin. Additionally, it will include information regarding the samples we used to characterize its effects. Ultimately, we will provide an overview of the biophysical techniques that were applied in the research. One class of technique we used was **fluorescence microscopy** that works by exploiting the properties of fluorescent molecules, which emit light (fluorescence) when they are excited by absorbable visible light. Such technique allows the visualization of structures and processes in biological specimens with high specificity and sensitivity. The second class of technique we employed was **Atomic Force Microscopy** (AFM) a scanning probe method that uses a sharp nanometric tip to interact with the sample. This method provides nanometric resolution in the xy plane and sub-nanometric resolution along the z-axis. Remarkably, AFM also allows to measure the nanomechanical properties of a sample by recording the forces between the tip and the material as a function of their relative distance. The two classes of techniques can be combined in the same microscope setup to compensate for each other's weaknesses and limitations. Such approach can be denoted as **correlative imaging**, a very powerful tool for a more comprehensive understanding of a specimen.

The **PART 2** of the work will include all the experimental data and it will be divided into three sections.

On the **first section** I will discuss our findings about the binding capabilities and the antiviral activity of Hyp with respect to SARS-CoV-2. We found out that Hyp effectively binds to the virus, and we estimated the maximum number of molecules involved in this binding. Our study also demonstrated the virucidal activity of Hyp against SARS-CoV-2 upon light irradiation. Intriguingly, we also discovered Hypericin's ability to reduce viral replication even in the absence of light, suggesting mechanisms of action unrelated to its photodynamic properties.

This finding is particularly noteworthy as the primary limitation of Photodynamic Therapy (PDT) is the requirement for light exposure at the target site, which isn't always feasible. A photosensitizer that remains effective in both light and darkness holds great promise for therapeutic applications.

Given Hyp's strong affinity for phospholipidic membranes, we Hypothesized that its effectiveness in the dark might be linked to alterations in the mechanical properties of the viral envelope, which could significantly impact the functionality of the pathogen.

In the **second section**, I will show the characterization of such multifaceted Hyp's antiviral mechanism of action by means of model membranes, specifically supported lipid bilayers (SLBs), which are designed to closely resemble the viral envelope. The mixture of phospholipids that we used allowed for a phase-separation. Denser regions in the bilayers, the so-called lipid rafts, were present; such domains are believed to be involved in many crucial biological processes.

We performed AFM measurements that revealed multiple actions either on the morphology and on the mechanical properties of the bilayer. Morphological changes were analyzed at different

concentrations and time scales, uncovering different effects; with the help of Fastscan AFM (up to 200 Hz) we could track the temporal dynamics of such changes.
The mechanical properties were assessed through the measurement of the Young Modulus, a parameter indicating the elasticity of a material, and by evaluating the force required to cause rupture. Additionally, by means of correlative AFM and confocal microscopy, we could be able to localize the photosensitizer in the bilayer, unveiling its preferential interaction properties for a specific lipid phase.
Finally, the **third section** will be devoted to the investigation of the effects of Hypericin on the mechanical properties of SARS-CoV-2; our purpose was to link these results to those we obtained on the SLBs. For this reason, we performed experiments to reveal the force to break the virus and the resistance to continuous AFM scanning, revealing interesting insights on the behavior of the virus.

PART 1: Theory and principles

1. Photodynamic therapy

Photodynamic therapy (PDT) is a minimally invasive medical treatment method that aims to produce toxic molecular species in close proximity of specific targets, mostly cancer cells, or pathogens like bacteria, fungi and viruses. Actually, the denomination of PDT is given to the application on cancer cells, by convention, while Photodynamic inactivation (PDI) is usually referred to microbial usage; PDT and PDI are theoretically identical, and the only thing that diversifies them is the target they are applied to.

PDT and PDI rely on the use of three fundamental elements:

- A light-sensitive and per se non-toxic molecule called photosensitizer (PS).
- light of a spectral range for excitation of the PS (typically vis-near IR).
- molecular oxygen ($^3O_2$), naturally dissolved in the physiological environment.

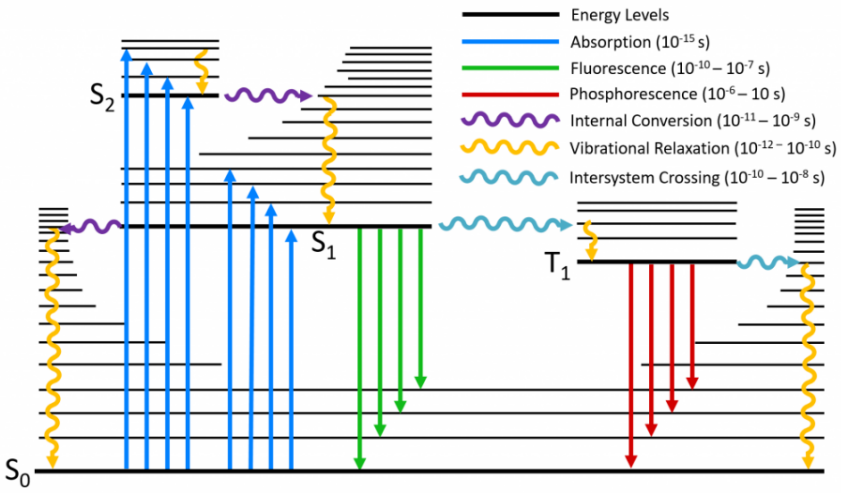

Figure 1.1: the description of the energy levels of a molecule and the transitions between them can be easily visualized by the Jablonski diagram. It is a very useful tool for understanding and explaining the behavior of molecules involved in light-matter interactions. The typical photophysical mechanisms are listed on the top right of the picture. Adapted from Edinburgh Instruments Ltd, [3].

It was Oscar Raab, a German medical student, who played a crucial role in the discovery of the principles underlying PDT [4]. Oscar Raab, working in Munich under the guidance of Professor Herman von Tappeiner, made a pivotal discovery in 1900. While investigating the effects of acridine dyes on protozoa, Raab observed a remarkable phenomenon. He found that in the presence of acridine red and light, there was a significant killing effect on the paramecium Infusoria, a discovery made by chance during a thunderstorm [5].

When the PS absorbs photons, the molecule is promoted from its ground singlet state (S_0) to an excited singlet state (S_n) (Figure 1.1). Subsequently, the PS loses the excess absorbed energy by various mechanisms, as described in the Jablonski diagram.

Of relevance to PDI, it can be converted to an excited triplet state (T_1), assuming the same spin multiplicity of molecular oxygen $^3O_2$.

This process of spin inversion, also called intersystem crossing, shouldn't normally be allowed because of the spin selection rule that prevents transitions between states of different spin multiplicity, but it is possible due to the spin-orbit coupling that occurs in some molecules.

The molecules can now interact with oxygen through two mechanisms, called type I and type II (Figure 1.2):

- **Type I**: The first is a photochemical process that involves the transfer of an electron from the excited molecule to molecular oxygen, resulting in the formation of superoxide radicals, such as O_2^{2-}, H_2O_2, OH^-, O_2^-.
- **Type II**: a photophysical process of energy transfer, where an electron exchange occurs between the excited donor molecule and the acceptor. As a result, the donor loses energy, and the acceptor transitions to the excited state; in this case, $^3O_2$ absorbs energy from the PS and transitions to the excited singlet state, $^1O_2$.

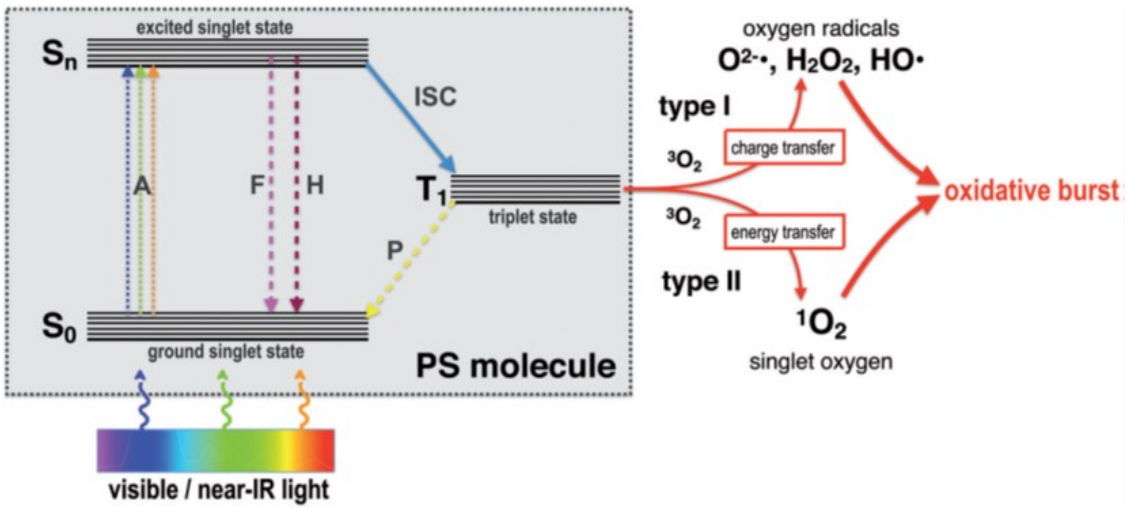

Figure 1.2: representation of the type I and type II interaction mechanism of the PS with $^3O_2$, from [6].

In particular, type II interaction between the PS in triplet state and $^3O_2$ is a Dexter energy transfer, which is a process involving the non-radiative transfer of energy between two molecules through quantum mechanical electron exchange interactions. This phenomenon is named after the scientist David L. Dexter, who first described it in the 1950s. Unlike Förster resonance energy transfer (FRET), which involves energy transfer through dipole-dipole interactions and operates over longer distances, Dexter energy transfer occurs through direct overlap of the electronic wavefunctions of the donor and acceptor molecules. This necessitates a very close proximity between the molecules, typically less than 10 angstroms.

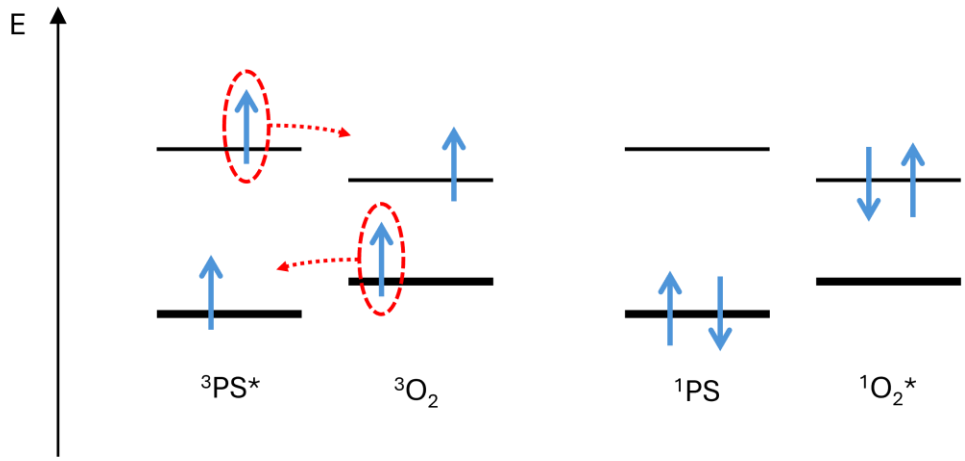

Figure 1.3: schematics of the electronic exchange that occurs in the triplet-triplet Dexter energy transfer, involving the PS as donor and $^3O_2$ as acceptor molecule. The electronic wavefunctions should overlap to allow the transition of electrons.

Reactive oxygen species (ROS), including singlet oxygen, are extremely dangerous agents for living cells and organisms, due to their strong oxidizing power, which attacks and weakens double bonds, such as those present in plasma membranes, nucleic acids, and five of the most common amino acids, Cys, His, Met, Trp, and Tyr. ROS can induce tumor cells' death in PDT and disrupt the tumor area, as well as damage the tumor vasculature and potentially initiate an antitumor immune response. Recent efforts to enhance these immune responses appear promising, potentially broadening PDT's application in the clinic [7][8]. ROS can also be exploited to eliminate unwanted guests such as viruses, bacteria, and fungi in PDI. Photodynamic Inactivation (PDI) of pathogens is a critical area of research, especially in the context of rising antibiotic-resistant bacteria and zoonotic viral pandemics.

Since cells and pathogens can develop resistance mechanisms to the radicals generated by type I interactions, for example, by upregulating the expression of superoxide dismutase (SOD, an enzyme capable of catalyzing enzymatic pathways to detoxify superoxide radical ($O_2^{\bullet -}$)), in some therapy applications it is preferable to have a PS with higher production of $^1O_2$ compared to other ROS.

As a matter of fact, in PDI and PDT the photosensitizer (PS) plays a crucial role. A good photosensitizer should have several key characteristics to be effective, the most important ones are:

- **High Photostability**: The PS should be stable under light exposure and not degrade quickly, losing its efficacy.
- **Strong Absorption of Visible Light**: A PS that strongly absorbs visible light is preferable, especially in the red and near-infrared spectral range (600-900 nm), where tissues are more penetrable; this makes the treatment more effective for a variety of applications.
- **High quantum yield of the triplet state**: the PS should have an excited triplet state with a long lifetime and sufficient energy (greater than 96 kJ/mol); this is directly reflecting the ability to produce ROS.
- **Low Dark Toxicity**: The PS should be non (or minimally)-toxic in the absence of light activation. This characteristic is important to ensure that it doesn't cause harm to the host organism or environment under normal conditions.
- **Chemical and Biological Compatibility**: The PS should be chemically and biologically compatible with the host organism and the environment in which it is used. It shouldn't interact negatively with other components of the treatment or the biological system.
- **Minimal Side Effects**: The PS should cause minimal or no side effects to the host organism or the surrounding healthy tissues during and after the treatment. High efficacy at low concentrations is required to minimize potential damage to healthy cells. Also, fast elimination of the molecule from the body is needed to avoid side effects.
- **Ease of Synthesis and Modification**: The synthesis of the PS should be straightforward, and it should be amenable to chemical modifications. This flexibility allows for the tailoring of PS properties to suit specific applications.
- **Appropriate Lipophilicity/Hydrophilicity Balance**: The PS should have a balanced lipophilicity and hydrophilicity to ensure good solubility and bioavailability. This balance also affects the PS's ability to penetrate cell membranes and reach target sites within pathogens.

The last of these points is critical because many photosensitizers are highly hydrophobic and thus poorly soluble in aqueous environments. A solution is often to introduce polar substituents to make them more soluble, as is often done with porphyrins, the most common photosensitizers. Hydrophobic molecules in an aqueous environment tend to minimize interactions with the solvent and form aggregates, which have very different photophysical properties from dissolved molecules. Aggregated photosensitizers poorly absorb light, and the few excited electronic states generated quickly quench, preventing the production of ROS. However, the best method to overcome this problem is to use a vehicle for their release that is biocompatible with the

therapy's target environment [9]. This approach has additional benefits. Photosensitizers are not inherently selective for their intended targets, necessitating a molecular targeting mechanism to ensure the therapy's effectiveness. Given that $^1O_2$ has a lifespan of about 3-4 μs [10][11] in aqueous environments and can only diffuse short distances of 100 to 200 nanometers, it needs to be in close proximity to the intended target. If not, there's a risk of unintentionally causing oxidative harm to healthy cells, which would counteract the therapeutic goals.

In PDT, it's crucial for the photosensitizer to differentiate between cancerous and normal cells. This is achieved through carriers that deliver the photosensitizer. These carriers take advantage of the tumor's unique physical and chemical properties for passive targeting. Alternatively, carriers can employ active targeting by capitalizing on the altered receptor densities found in tumor cells[12]. Various studies have also shown that photodynamic therapy (PDT) can enhance anti-tumor immunity [13]. Mice whose tumors were treated with PDT demonstrated an ability to resist subsequent tumor stimulation, indicating the presence of immunological memory. A current challenge is to demonstrate the extent to which PDT applied to tumors such as Non-Small-Cell Lung Carcinoma can stimulate the immune system to adapt and counteract cancer recurrence [14] [15].

This approach to exploit the immune system for the treatment of cancer is relatively new and is called cancer immunotherapy [16][17]. It is a revolutionary approach in the treatment of cancer, leveraging the body's own immune system to combat the disease. This field has seen significant advancements and has become a vital part of the oncologic therapeutic arsenal [18]. Unlike traditional treatments like chemotherapy and radiation, which directly target cancer cells, immunotherapy works by enhancing or modifying the immune system's response to cancer. It can either stimulate the immune system to work harder or smarter in attacking cancer cells, or it can provide the immune system with additional components, such as man-made immune system proteins.

We will not dig any deeper into this aspect of application of PDT, instead we will focus on the PDI inactivation of pathogens.

1.1 Application to Bacteria and Viruses: Photodynamic Inactivation

Although PDT is more commonly known for its application in cancer therapy, its photodynamic effect has extreme relevance in the context of implementation against pathogens.

Microbial infections (including those caused by bacterial, fungal, and viral pathogens) resulted in nearly 8.5 million deaths worldwide in 2016, with 700,000 directly attributed to drug-resistant infections. This number could rapidly increase in the coming years because, in the worst-case scenario, up to 10 million people could die each year due to antibiotic-resistant infections if left unchecked. The primary cause of microbial antibiotic resistance is the overuse and misuse of antibiotics in both human and animal applications [19].

These alarming statistics have rekindled interest in photodynamic inactivation (PDI), which has recently gained considerable attention. Reactive oxygen species produced can simultaneously attack various biomolecular sites in the target pathogen (proteins, lipids, nucleic acids...), offering multiple and variable action sites. This lack of specificity towards the target bypasses conventional resistance mechanisms and inhibits the development of resistance to the agents themselves [6] [20].

Antibacterial PDI can be used in the context of localized infections accessible to light, such as skin infections, chronic wounds, diabetic foot and leg ulcers, but the use of optical fibers also makes areas such as the upper respiratory tract, gastrointestinal tract, and ears accessible. However, only a few clinical trials have been conducted in this direction [1], and the method is currently clinically approved for the treatment of periodontal or endodontic dental infections [6].

PDI applied to viruses has historically been explored to a lesser extent, although antiviral effects have been known for some dyes/photosensitizers such as methylene blue and other phenothiazine derivatives since the 1960s, like acridine orange among others [20]. In the context of antiviral PDI, a recent study explored the effectiveness of methylene blue-based photodynamic inactivation against intracellular B-CoV and SARS-CoV-2 viruses. The study assessed the efficacy of PDI under various light sources in vitro, focusing on its potential as a treatment option for infections caused by these viruses [21].

Clinical applications of antiviral PDI have been controversial for some time, and more than half of the publications on this topic have been disseminated in the last 15 years, suggesting that despite a long history of photodynamic investigations, the use of antiviral PDI is still a young and rapidly growing field.

In the medical field, the main areas that have seen wider application of antiviral PDI are the purification of blood derivatives [22] and the treatment of a few viruses [23]. PDI has been used on various forms of Herpes Simplex Virus (HSV) infections, including oral, genital, ocular, and herpes zoster infections; on external Human Papillomavirus (HPV) manifestations [24], and there is also emerging evidence suggesting the efficacy of PDT in treating reactivated Varicella Zoster

Virus VZV, with case reports indicating significant clinical improvement and reduced recurrence after treatment [25].

Moreover, Recurrent Respiratory Papillomatosis (RRP) caused by HPV, is one of the few internal diseases currently being treated with PDI. The treatment is typically combined with standard removal or disruption methods, and studies have shown promising results with significant reduction in recurrence rates and manageable side effects [26].

Furthermore, antiviral PDI has also garnered significant interest in areas such as water [27], food [28] and surface decontamination [29].

Recently, PDI is being proposed as an alternative treatment in classical antiviral therapy based on drugs. Just like antibiotic resistance, resistance to antiviral drugs is currently a cause for concern [30] [31]. Therefore, photodynamic inactivation (PDI) of viruses is of interest as an alternative tool in antiviral treatments.

Additionally, recent studies have revealed systemic effects of photodynamic treatment, including the triggering of immune responses, just as we mentioned happening in PDT against tumors [23] [32][33]. This discovery enhances the appeal of PDI as not just an alternative, but also a complementary approach to conventional therapies.

Anyway, despite being an exciting and promising method, PDI is still largely in the research and development phase, especially concerning its application to various types of pathogens and in different settings. The implementation in clinical and other practical settings are dependent on the ongoing research, and will benefit from technological advancements, and be subject to regulatory approvals.

1.2 The Most Used Photosensitizers in Antiviral PDI

In the advancement of both antitumor and antimicrobial therapies, a variety of compounds known for their ability to generate reactive oxygen species have been explored. Among these, specific classes have shown remarkable effectiveness in inactivating numerous viral species, particularly in in vitro studies. The most notable classes include:

- Polyphenols such as curcumin;
- Riboflavin and its derivatives;
- Phenothiazinium derivatives, like methylene blue and toluidine blue;
- Fullerenes and carbon nanomaterials;
- Phenalenone derivatives;
- Tetrapyrroles, the most diverse class of photosensitizers, including porphyrins, phthalocyanines, chlorins and bacteriochlorins. These molecules have long played a decisive role in antitumor PDT;
- Xanthene derivatives: like Eosin Y, Erythrosine and Rose Bengal that are all derived from fluorescein;
- Quinones, such as Hypericin.

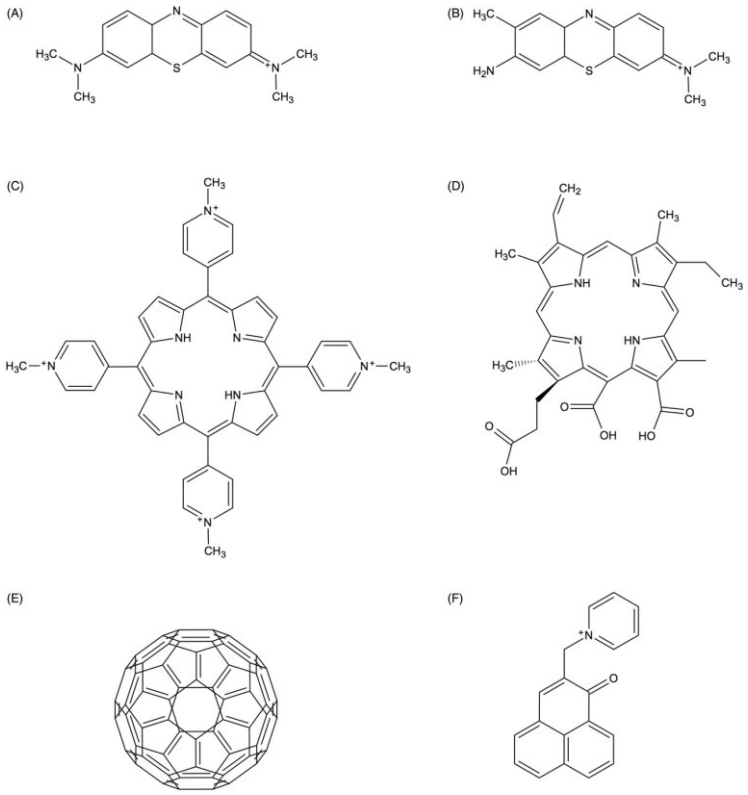

Figure 1.4: a few examples of photosensitizers used in PDI, image from [6]*. a) Methylene Blue; b) Toluidine Blue; c) TMPyP (a modified porphyrin); d) chlorin-e6; e) fullerene C60, f) SAPYR (a water-soluble phenalenone derivative). Adapted from* [6]*.*

1.3 Hypericin

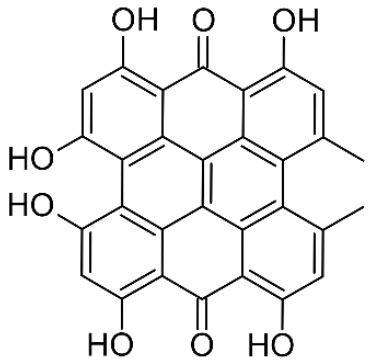

Figure *1.5: Structure of Hypericin.*

Hypericum perforatum, commonly known as St. John's wort, is an herb historically used in traditional medicine for healing wounds, treating burns, and alleviating mild to moderate depression. Its use in contemporary treatments for mild depression persists, although the exact mechanisms of action are not fully elucidated. It's thought to work by inhibiting the reuptake of excitatory neurotransmitters like serotonin, norepinephrine, and dopamine.

Hypericin (Hyp) (Figure 1.5) is the primary active compound found in Hypericum species and is considered key to the therapeutic effects of St. John's wort. It is a polycyclic aromatic hydrocarbon, specifically a naphthodianthrone, known for its hydrophobic nature and insolubility in water. Hypericin possess several photophysical characteristics when it is solubilized in an apolar environment.

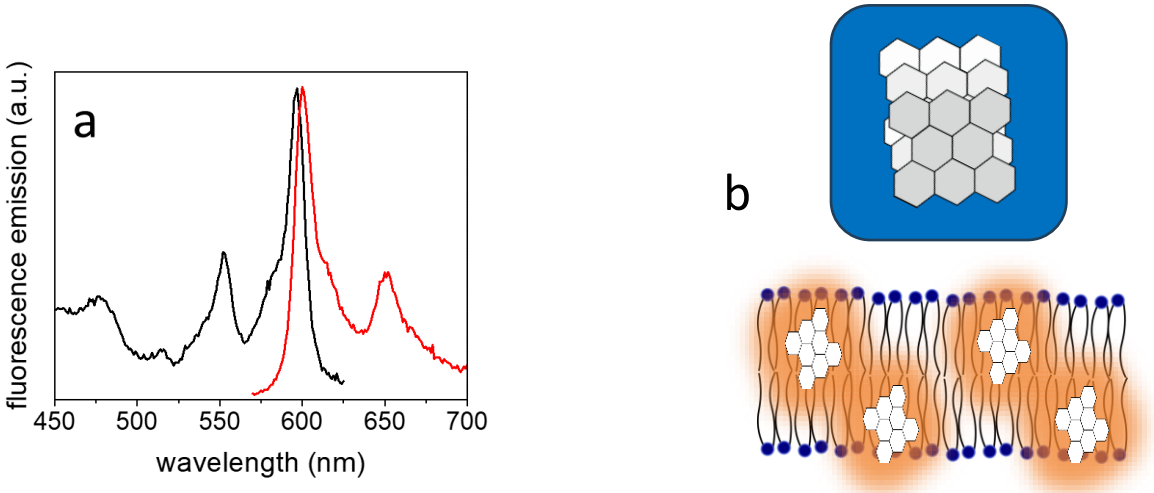

Figure 1.6: a) absorption and excitation spectrum of Hyp in a lipophilic environment [34]*. b) Hyp is poorly soluble in aqueous environments (top), while it recovers all its photophysical properties, fluorescence comprised (bottom). a) is adapted from* [34].

It is distinguished by its bright red color and strong absorption in both the visible and UV spectrums (Figure 1.6a). Owing to these intriguing properties, Hypericin has been the subject of increased medicinal and therapeutic interest in recent years. Photophysical studies reveal that Hypericin is an effective fluorophore, with a quantum yield ($\phi_F = 0.35$) in DMSO, making it suitable for fluorescence-based investigations.

Notably, Hypericin's most significant attribute is its potent ability to generate singlet oxygen, evidenced by a remarkable quantum yield of ($\phi_\Delta = 0.33$) [35]. This makes it a potent photosensitizing agent, opening avenues for its application in photodynamic therapy.

In recent years, research has demonstrated that Hypericin displays a preferential interaction with cancer cells over healthy ones, showing minimal toxicity to the latter [36]. Its photodynamic activity can induce the death of cancer cells. Furthermore, Hypericin has shown significant cytotoxic effects on tumor tissues even without light exposure. Various in vitro and in vivo cancer models have reported substantial inhibitory effects by Hypericin. However, there have been relatively few clinical trials conducted to evaluate its safety and actual clinical effectiveness in patients [37].

The effectiveness of Hypericin in photodynamic inactivation (PDI) has been studied in various contexts, against both bacteria and viruses.

Hyp was found effective against a variety of bacteria, interestingly for both Gram-negative such as *Escherichia Coli* [38] , or Gram-positive like *Staphylococcus Aureus* and *Enterococcus faecalis* [39] with a consistent effect also on biofilm aggregates of the latter [40].

Hyp has also demonstrated significant antiviral activity in various studies. The effectiveness of Hypericin in combating viruses is largely determined by its affinity towards viral components and the number of active molecules that attach to individual viruses. Studies have demonstrated that Hypericin can significantly inactivate several viruses when exposed to visible light and, in some cases, even in the absence of light [41][42] . This efficacy is particularly notable against a variety of lipid containing enveloped viruses [2], such as influenza A virus, herpes simplex, murine cytomegalovirus, Sindbis, hepatitis B and C, equine anemia, and HIV [43]; however, Hypericin is inactive against non-enveloped viruses, that don’t contain any phospholipid envelope [44].

Hyp, as we already said, is a hydrophobic chromophore, and therefore possesses a preferential localization in lipid membranes [45], mediated by its lipid solubility [46]. Hyp’s increasing evidence on the effectiveness against membrane-envelope viruses suggested its potential as a treatment for SARS-CoV-2 infections, an enveloped virus itself.

2. Enveloped virus

Coronaviruses are a diverse group of viruses that can infect many animals, including humans. They are characterized by specific features such as their type of nucleic acid, a lipid envelope, and a distinct shape. These viruses are single-stranded positive-sense RNA viruses, varying in size from 60 nm to 140 nm. Under a microscope, their spike proteins on the membrane give them a 'crown-like' appearance, leading to their name [47]. They belong to the Coronaviridae family within the Nidovirales order (Figure 2.1). These viruses are categorized into α-, β-, γ-, and δ-coronaviruses, with α- and β-coronaviruses primarily infecting mammals and γ- and δ-coronaviruses affecting birds and both mammals and birds, respectively. The most concerning for humans are the α- and β-coronavirus genera [48] [49].

Four human-affecting coronaviruses, HKU1, NL63, 229E, and OC43, generally cause mild respiratory illnesses. However, in the last twenty years, there have been significant outbreaks due to animal coronaviruses jumping to humans. The first was in 2002-2003 with the emergence of SARS-CoV, a β-coronavirus from bats, in China's Guangdong province. It used palm civets as an intermediary and led to 8422 infections and 916 deaths. A decade later, MERS-CoV, another bat-origin β-coronavirus, emerged in Saudi Arabia, where dromedaries were the intermediate hosts. This virus infected 2494 people and caused 858 deaths.

Category	**Coronaviruses**	**Humans**
Realm	*Riboviria*	
Order	*Nidovirales*	Primates
Suborder	*Cornidovirineae*	
Family	*Coronaviridae*	Hominidae
Subfamily	*Orthocoronavirinae*	Homininae
Genus	*Betacoronavirus*	*Homo*
Subgenus	*Sarbecovirus*	
Species	*Severe acute respiratory syndrome-related coronavirus*	*Homo sapiens*
Individuum	SARS-CoVUrbani, SARS-CoVGZ-02, Bat SARS CoVRf1/2004, Civet SARS CoVSZ3/2003, SARS-CoVPC4-227, SARSr-CoVBtKY72, SARS-CoV-2 Wuhan-Hu-1, SARSr-CoVRatG13, and so on.	Dmitri Ivanovsky, Martinus Beijerinck, Friedrich Loeffler, Barbara McClintock, Marie Curie, Albert Einstein, Rosalind Franklin, Hideki Yukawa, and so on.

Figure 2.1: taxonomy of Coronaviruses. Analogy with human taxonomy. The founders of virology and other eminent scientists represent individual human beings. Adapted from [49].

2.1 SARS-CoV-2

In December 2019, Wuhan, a city in China's Hubei province, reported 27 unexplained pneumonia cases. A common link among early patients was their proximity to Wuhan's Huanan Seafood Market [50].

Chinese authorities informed the WHO about the outbreak on December 31, 2019, following investigations into the patients' respiratory samples by specialized labs. The Wuhan market was shut down the next day. Tests near the market detected the virus, suggesting the market as a potential origin for the zoonotic virus spread. Moreover, the virus's ability to transmit between humans was confirmed by the rising number of cases unrelated to the market.

By January 7, this virus was identified as a novel coronavirus, sharing over 95% genetic similarity with bat coronaviruses and around 80% with SARS-CoV. Classified as "severe acute respiratory syndrome-related coronavirus" in the β-coronavirus genus, it was named SARS-CoV-2 [47]. Its close genetic relation to bat coronaviruses indicated a possible bat origin, with transmission to humans potentially involving an intermediary species.

2.1.1 Structure

SARS-CoV-2 is structurally very similar to other coronaviruses, and it's composed of a few fundamental components (Figure 2.2):

- **RNA Genome:** the genetic material of the virus, single-stranded RNA genome, which is positive-sense. This means the viral RNA can be directly translated into viral proteins by the host cell's ribosomes.
- **Nucleocapsid (N) Protein:** a protein that holds the RNA genome. They mainly play a role in virus assembly.
- **Membrane (M) and Envelope (E) Proteins:** proteins embedded in the lipid envelope.
- **Envelope:** a phospholipidic bilayer which is derived from the host cell membrane during viral replication and budding, from the lipids of the Endoplasmic Reticulum (ER) [51][52] (Table 1). It plays a crucial role in the virus's ability to infect host cells.

	Mol% of ER membrane lipids
Phosphatidylcholine	58%
Phosphatidyletanolamine	22%
Phosphatidylserine	3%
Phosphatidylinositol	10%
Sphingomyelin	3%
Cholesterol	0.018%

Table 1: lipid constituents of the viral envelope, which are identical to those found in the ER.

- **Spike (S) Proteins:** the most notable feature, a protein which protrudes from the virus surface, providing the characteristic crown-like appearance. These proteins are critical for the virus ability to infect host cells; their binding to the ACE2 receptor facilitates the virus entry into the host cell.

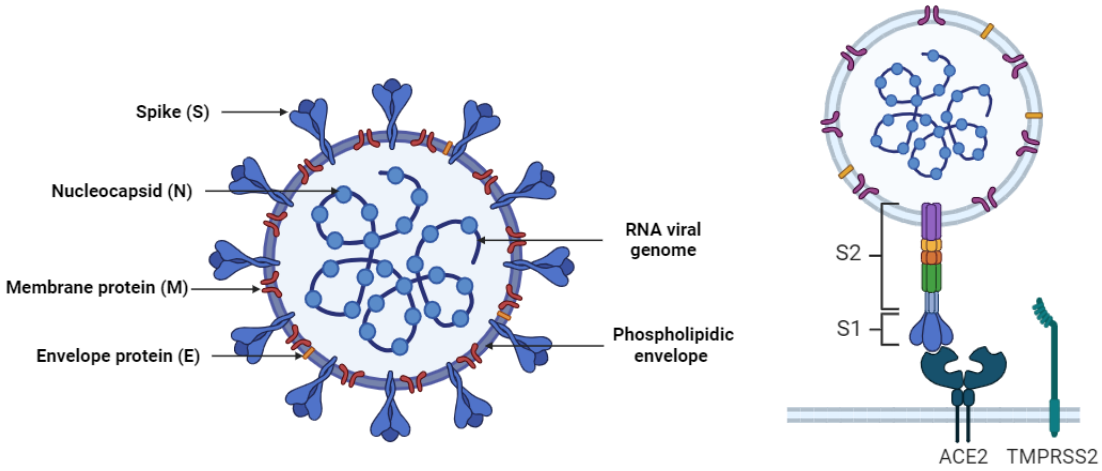

Figure *2.2: SARS-CoV-2 structure (left) and representation of the functional subunits of S, with focus on the binding between S1 and Ace2 (right). Created with BioRender.com.*

2.1.2 Interaction with human cells: the role of Spike and viral envelope

As we said, the Spike (S) is essential for introducing its genetic material into the cells of the host organism. It is a glycoprotein abundantly located on the virus's phospholipid envelope. The S protein exists in a metastable form, and it's designed to undergo significant rearrangements, enabling the fusion of the viral membrane with that of the host cell, thus facilitating viral entry [53]. It has a M_w = 440 kDa and it is composed of three identical subunits. These subunits form a trimeric structure, which is a common feature among coronavirus spike proteins. Each subunit in the trimer is divided into two main functional parts: the S1 and S2 subunits (Figure 2.2).

The S1 subunit of the virus targets and attaches to the host cell's receptor via a specific area called the receptor binding domain (RBD). The receptor in question on the host cell is the Ace2 protein, an angiotensin-converting enzyme, which plays a key role in regulating the hormone angiotensin. Ace2 is predominantly found in cells of the lungs, kidneys, intestines, and heart.

The splitting of the S1 and S2 subunits is key to the subsequent activation of the S2 subunit; this process is facilitated by the action of a serine protease known as TMPRSS2 [54]. This enzyme induces irreversible conformational changes, enabling the activation process of S2.

S2 subunit actually plays a critical role in mediating the viral fusion and entry process into the host cell. It exploits several domains, that are responsible for bringing the viral and cell membranes close enough to fuse, and plays a role in disrupting and connecting the lipid bilayers of the host cell membrane, essential for viral fusion and entry [55]. In this framework, the viral envelope plays a fundamental role in the infection, as well. Indeed, the viral envelope plays a

multifaceted role in viral entry, from facilitating the initial attachment to the host cell to mediating the fusion process that allows the viral genome to enter the host cell. The field of research in this domain is constantly advancing, offering new understanding of the mechanisms behind viral cell infection and identifying possible targets for the development of antiviral treatments.

2.2 Supported lipid bilayers

Biological membranes are crucial in all living organisms, at the basis of many vital physiological processes. These membranes are primarily made up of lipids, including phospholipids and cholesterol, forming what is known as the phospholipid bilayer. They also contain carbohydrates and various membrane proteins. This assembly acts as a selective barrier, distinguishing the internal environment from the external milieu in both eukaryotic and prokaryotic cells, including bacteria. The lipid bilayer is not just a protective layer for cells and their internal compartments; it is also pivotal in cellular communication and membrane transport, hosting many of the mechanisms involved in these processes, and plays a key role in certain organelles like mitochondria and the nucleus.

Additionally, some viruses are composed of an outer phospholipid envelope, which incorporates critical membrane proteins, as we saw for coronaviruses.

In recent decades, several models have been developed to better understand the properties of biomembranes. One of the most prominent and widely used models is the Supported Lipid Bilayer (SLB), a lipid bilayer positioned on a solid surface, making it ideal for analysis using microscopic techniques such as AFM and fluorescence microscopy.

The aim of a model system like that, is to replicate the molecular activities that occur in membranes as closely as possible. This means maintaining the structure and fluidity of lipid bilayers by including phospholipids and, in some cases, also incorporating other components such as cholesterol, proteins, and carbohydrates to better replicate the complexity of biological membranes.

In systems with solid supports, membrane stability is preserved thanks to a layer of water, about 1-2 nm thick, trapped between the substrate and the bilayer [56]. It is also necessary to maintain a layer of water on top of the bilayer, to ensure proper stability (

Figure 2.3).

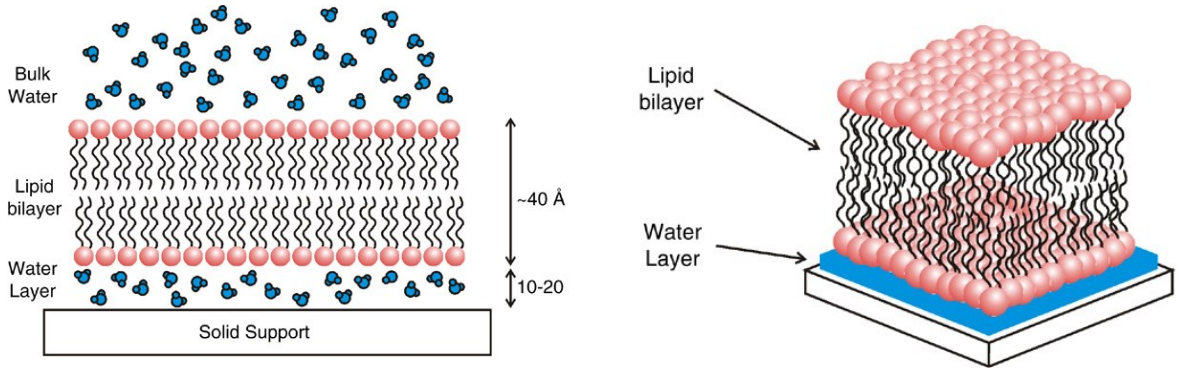

Figure *2.3: visualization of a generic supported lipid bilayer. Reprinted with permission from Elsevier,* [56]. *Copyright © 2006 Elsevier Ltd. All rights reserved.*

The range of substrates that can effectively support phospholipid bilayers is somewhat narrow. To maintain a high-quality membrane, characterized by minimal defects and high lipid mobility, the surface must be hydrophilic, smooth, and clean.

Substrates that can be used include fused silica, borosilicate glass, and oxidized silicon [57], however the most established and used solid support is **mica**, a crystal that offers all the ideal features.

Lipid bilayers in nature are always characterized by specific mixture of phospholipids, depending on the function of the membrane. Indeed, the specific composition of phospholipids in a membrane can greatly influence the membrane's properties, such as fluidity, permeability, and the ability to host various proteins. The composition can vary depending on the type of cell and its environment. Moreover, bilayers are often asymmetric, i.e. the lipid compositions of the two leaflets are different, reflecting the distinct functions of each side of the membrane.

Phospholipids that can be found in membranes can be grouped as follows:

- **Glycerophospholipids:** The most common phospholipids, which consist of a glycerol backbone bound to two fatty acid chains and a phosphate group. The phosphate group is further connected to an alcohol. Examples include Phosphatidylcholine (PC), Phosphatidyletanolamine (PE), Phosphatidylserine (PS), Phosphatidylinositol (PI).
- **Sphingolipids:** Instead of having glycerol as backbone, they possess a sphingosine backbone. Important examples include sphingomyelin (SM), ceramides, glycolipids (like gangliosides, which is particularly abundant in the brain cells).

Among the phospholipids, there are differences based on the number of double bonds that can be found in the hydrocarbon tails. They can be **saturated** If all the carbon atoms in the hydrocarbon chain are connected by single bonds (C-C), or **unsaturated**, if there are one or more double bonds (C=C) in the hydrocarbon chain.

Such difference deeply influences the physio-chemical properties of the lipids. The presence of double bonds in unsaturated lipids inhibit the close packing of their chains, which in turn makes the lipid bilayer more resistant to freezing. At room temperature they tend to be in a **liquid** (fluid) phase, or L_α [58].

Furthermore, since the hydrocarbon chains of unsaturated lipids are spaced further apart, lipid bilayers that incorporate them tend to be thinner compared to those composed solely of saturated lipids. Saturated lipids, on the other hand, are found in a stiffer phase at room temperature, **gel** phase, or L_β.

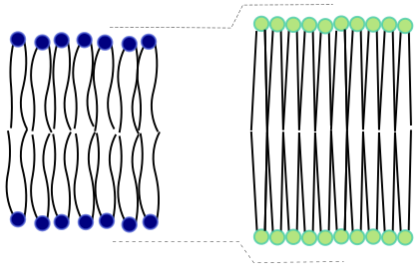

Figure *2.4: unsaturated phospholipids (blue) at liquid phase (L_α), and saturated (green) in gel phase (L_β) forming a thicker and stiffer double layer.* ***The typical difference in thickness between L_α and L_β is ~2nm*** [59].

Another fundamental component of membrane, although not a phospholipid, is Cholesterol, a sterol which is distributed among the phospholipids within both layers of the membrane. It is known to have many effects on the membrane: among them, it influences the membrane organization and the phase transitions, having a regulatory effect on the fluidity of the membrane [60]. Its presence promotes the formation of "intermediate" phases, i.e. L_d (liquid disordered) and L_o (liquid ordered phase) phases which we can respectively define as L_α and L_β containing Cholesterol. Whenever there are saturated and unsaturated lipids, as well as Cholesterol, a phase separated lipid bilayer is formed. It is believed that regions enriched of sphingolipids and Cholesterol are responsible for the presence of the L_o phase in membranes, forming the so-called **lipid rafts** [61]. These regions are believed to serve as anchoring platforms for proteins and are involved in various processes such as signal transduction, sorting and trafficking [61] [62]
Because of their biological relevance, it is important, when modelling a SLB, to ensure their formation, by inducing a phase-separation in the bilayer.
When analyzed with microscopy techniques such as atomic force microscopy (AFM), the phase separation, i.e. the presence of lipid rafts, pops up as a difference in height (Figure 2.5)

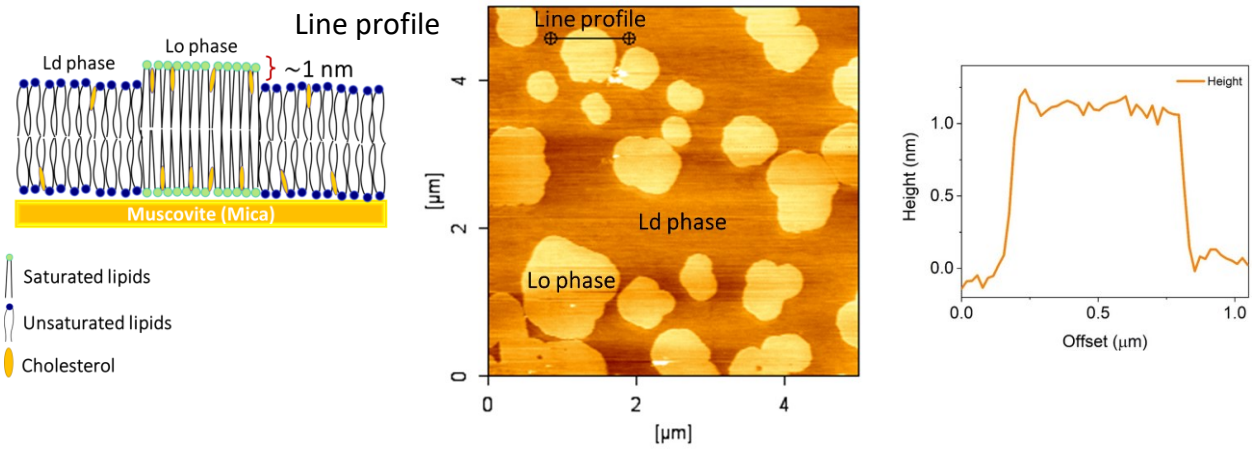

Figure *2.5: a) the difference in height between the two lipid phases is visualized with AFM (b). The clearer regions are the lipid rafts. c) on the line profile we can observe a difference of ~1 nm.*

3. Fluorescence microscopy

Optical microscopy, (or light microscopy), is a series of techniques used to view small samples and objects that are not visible to the naked eye, by using visible light. A system of lenses collects and focuses the light to create a magnified image of the sample. The resolution of a microscope is the ability of a microscope to distinguish two points as separate entities and, for light microscopy, it is limited by the diffraction of light. Indeed, when the light passes through a circular aperture, such as a circular lens of a microscope, the light waves interfere with each other, resulting in a diffraction pattern which is called the Airy pattern. Such intensity distribution appears as a bright central spot surrounded by a series of concentric dark (zero-intensity points called Airy disks) and bright rings. The 84% of light intensity can be found in the central peak (the Airy spot). The Airy pattern exemplifies the optimal performance attainable by an instrument constrained by diffraction.

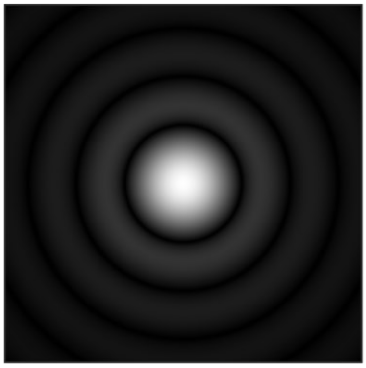

Figure *3.1: the Airy diffraction pattern. Adapted from Wikipedia* [63].

When this pattern of light intensity is replicated on the image plane, it is also referred as the point spread function (PSF), that describes the response of an imaging system to a point source of light or point object.

Ernst Abbe formulated a criterion, the **Abbe** diffraction criterion, that gives a definition of the maximum achievable resolution [64]. Such criterion states that the ability to resolve detail in the object being imaged is limited by the wavelength of light used and the numerical aperture of the microscope's lens system:

$$d_{x,y} = \frac{\lambda}{2NA} \tag{1}$$

$$d_z = \frac{2\lambda}{NA^2} \tag{2}$$

Where $d_{x,y}$ is the lateral resolution, and d_z is the axial resolution. λ is the wavelength of the light, while NA is the numerical aperture of the objective lens (Figure 3.2), which is linked to the light-gathering ability of the lens. In other words, it characterizes the range of angles over which the system can accept or emit light. Mathematically, NA is defined as:

$$NA = n \cdot sen\theta \tag{3}$$

Where n is the refractive index of the medium in which the lens is working (e.g., air, water, oil) and θ is the half-angle of the maximum cone of light that can enter or exit the lens.

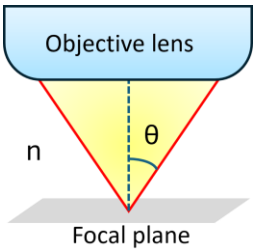

Figure *3.2: drawing of the numerical aperture of a microscope's objective.*

Therefore, for an optical microscope, which exploits light in the range of wavelengths, 400-700 nm, the resolution limit is roughly the half of the shortest usable wavelengths, ~200 nm.
Another important criterion to define the resolution of a microscope was given by **Rayleigh** in the late 19th century [65]. However, it does not constitute a strict boundary for resolution, but it's based more on the human perception of resolution.
The minimum resolvable distance between two objects is defined as the point where the peak of the Airy pattern of one source coincides with the first minimum of the Airy pattern of the second source. Such distance can be defined as:

$$d = 1.22 \cdot \frac{\lambda}{2NA} \tag{4}$$

Among the light microscopy techniques that have evolved during the years, the most popular and widely used is fluorescence microscopy. Such technique has the capability to image samples noninvasively at very high resolution, that makes it a valuable technique in biological and biophysical research. Fluorescence is a form of photoluminescence that occurs when a molecule that absorbs light of a certain wavelength almost immediately re-emit light at a longer wavelength. When a photon is absorbed, the molecule is promoted from the ground state S_0 to an excited state S_n of higher energy. The transition may occur only if the energy of the incoming photons corresponds to the energy difference between S_n and S_0.

The molecule then loses some energy through various non-radiative mechanisms (internal conversion, vibrational relaxation) to the lowest vibrational level of the first excited state S_1. From this energy level the radiative fluorescence emission can occur (Kasha's rule). The loss of energy associated with non-radiative relaxation leading to the lowest vibrational level of S_1 means that the emission of photons occurs at a longer wavelength than absorption. Such molecules, which can emit fluorescence with high efficiency, are called fluorophores. In fluorescence microscopy, the sample is illuminated with a specific wavelength of light (excitation) that the fluorophore absorbs, its consequent emission which happens at a different wavelength (Stokes shift) is recorded. This spectral separation is exploited by the instrument, and by means of some optical components, the excitation and emission can be separated, so that only the emission from the fluorophore is detected. Because of that the most common configuration exploits only one objective lens, for either the excitation and the emission light (**epifluorescence**).

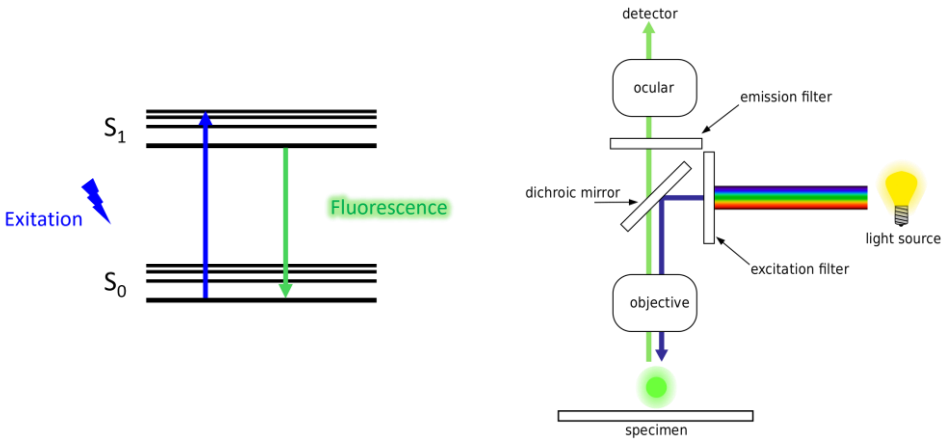

Figure *3.3: a) illustration of the photophysical mechanism of fluorescence, b) scheme of an epifluorescence widefield microscope. b) is adapted from Wikipedia,* [66].

Since the fluorophores can be chemically attached to target molecules through several direct or undirect methods, e.g., antibody labeling or genetic expression of fusion proteins, this microscopy technique achieves high specificity, allowing for sensitive detection of biological processes at the cellular and molecular levels.

One of the most straightforward implementations of fluorescence microscopy is represented by the widefield microscope. This modality involves the uniform illumination of the entire specimen under observation. The entire field of view is excited simultaneously, allowing for the observation of fluorescently labeled structures within the sample. The image is formed by the light coming from the sample and is captured either through an eyepiece for direct observation or onto a camera sensor. This approach is relatively simple and fast, making it suitable for a variety of applications where rapid imaging of larger areas is required. The main limitation is represented by the background fluorescence since all planes of the sample are illuminated and emit light simultaneously, potentially reducing image resolution and contrast.

3.1 Confocal Laser Scanning Microscopy

Confocal laser scanning microscopy is an advanced optical imaging technique, which major feature is the optical sectioning, i.e. the ability to image only a specific plane (or optical section) of the specimen at a time. In this way it overcomes the limitation previously described of the widefield fluorescence microscope.

To achieve sectioning confocal microscopy uses a point illumination. The light is focused to a small point on the specimen and scanned across the specimen in a raster pattern (both laterally and axially) to build up a three-dimensional (3D) image, one point at a time. The light emitted or reflected from that spot is collected and focused onto a single-point detector (PMT, APD, SPAD, etc.). The excitation source is constituted by a laser which provide intense, monochromatic, and coherent light, ideal for precise illumination and for exciting fluorescent dyes.

Such a microscope involves the use of two pinholes, small and circular apertures; one is placed after the excitation source and the other before the detector. The two pinholes are configured such that their focal planes coincide (or belong to conjugated focal planes), as well as the object, from which the name “con-focal” [67] [68].

The light from the in-focus plane of the specimen passes through the pinhole and is detected, while those coming from planes above or below the focal point is mostly out-of-focus when it reaches the pinhole and is thus not detected. By excluding the out-of-focus light it’s possible to achieve the optical sectioning. A correct pinhole size should yield a PSF with a maximum diameter corresponding to the central bright spot of the Airy disk, i.e. $\leq$ 1 Airy Unit (AU). In addition, by reducing the dimension of the pinhole is also possible to slightly improve the resolution, either lateral [69] or axial [70] [71], but in expense of the signal-to-noise ratio [72].

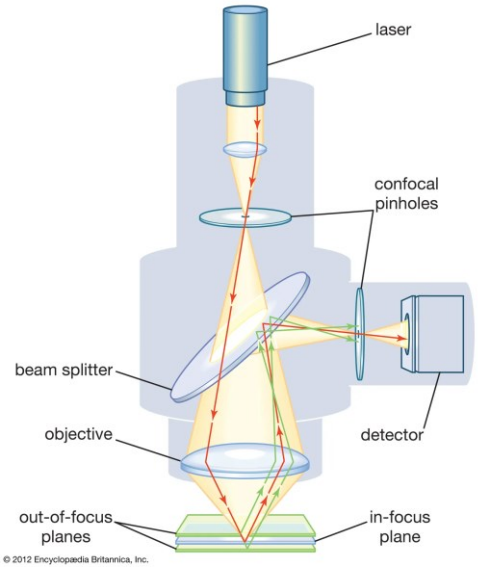

Figure *3.4: typical architecture of a confocal microscope. Adapted from Encyclopedia Britannica* [73]. *Copyright © 2012 Encyclopedia Britannica, Inc.*

3.2 Super-resolution and STED microscopy

Over the course of the last decades, microscopists have made many efforts in developing new techniques to improve the resolution of fluorescence microscopes, breaking the limit imposed by diffraction, with the aim to explore biological structures and processes happening at the nanoscale. Many super-resolution techniques have been proposed to circumvent this limit. These methodologies employ various strategies to go beyond the diffraction limit, but they all rely on the same principle: the selective switching between the "on" and the "off" states of the fluorophores. This process can be **stochastic** or **deterministic** [74].

Stochastic techniques like STORM (STochastic Optical Reconstruction Microscopy) [75][76] or PALM (fluorescence PhotoActivation Localization Microscopy) [77] perform a random activation and subsequent localization of individual fluorescent molecules. At any moment, only a few fluorophores are in the "on" state, allowing their positions to be determined with high precision. Repeating this process over time and locating the positions of such molecules allows for the reconstruction of a super-resolution image.

On the other hand, deterministic techniques like STED (Stimulated Emission Depletion) [78] or SSIM (Saturated Structured Illumination Microscopy) [79] spatially select which are the fluorophores that should be on the "on" or "off" state by means of a controlled illumination.

The groundbreaking work on super-resolution microscopy techniques was worth the Nobel Prize in Chemistry to S. Hell, E. Betzig and W.E. Moerner in 2014 [80].

The STED microscope is a laser scanning microscope, with an architecture very similar to the confocal. The main difference relies on the presence of an additional laser beam, the STED beam, which is shaped as a doughnut featuring a zero-intensity center. This beam is designed to quench the fluorescence emission in the periphery of the illuminated area by stimulating the excited molecules to return to the ground state by stimulated emission, leaving only the molecules in the very center of the doughnut-shaped beam to be detected.

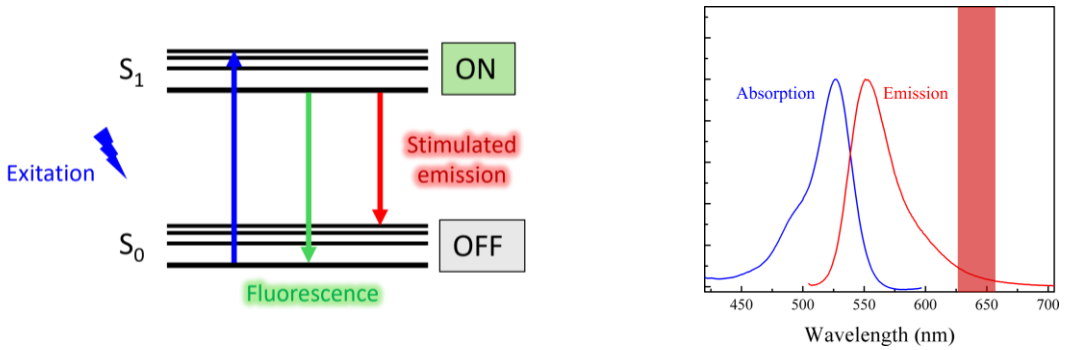

Figure *3.5: stimulated emission is a competitive process with respect to the spontaneous emission (fluorescence) (left). Example of an ideal range of wavelength for the STED laser, at given spectra is indicated with the red bar that lies on the tail of the emission spectrum (right). The image on the right is adapted from* [81] *Copyright © 2022 Angstrom Technologies, Inc. All rights reserved.*

STED imaging requires a correct temporal and spatial alignment of the STED beam. Indeed, the STED beam should be synchronized with the excitation beam to avoid that fluorescence occurs before the STED pulse reaches the molecule. Additionally, since any imperfections on the zero-intensity at the center of the beam impacts negatively on the signal to noise ratio, special care should be given to the beam polarization [82] Also, the wavelength of the STED beam is crucial. The stimulated emission efficiency depends on the emission spectrum of the fluorescent molecule and the laser wavelength should be chosen properly. A wavelength that aligns with the maximum of the emission spectrum should give the maximum of efficiency of this transition. However, the absorption and emission spectrum are not enough spectrally separated (Stokes shift) to avoid absorption in correspondence of the maximum of emission. For this reason, the STED wavelength must be more red-shifted and should align with the tail end of the emission spectrum of the fluorophores. At such wavelengths the stimulated emission is less efficient and occurs at higher powers, requiring the STED beam to be some order of magnitudes more powerful than the excitation laser.

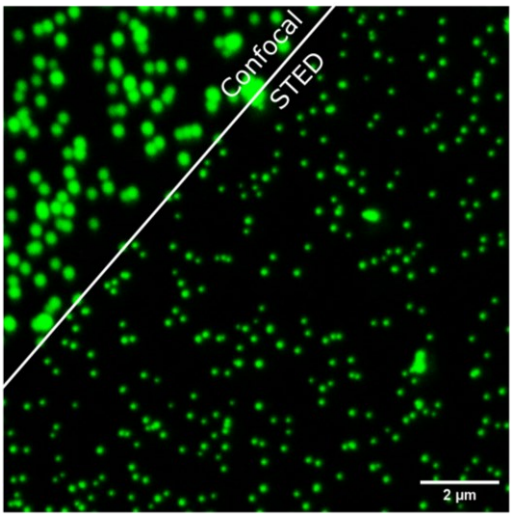

Figure *3.6: images of Abberior STAR green, fluorescent beads (d = 40 nm) acquired with a Leica SP5. λ_{ex} = 488 nm, λ_{STED} = 592 nm. We can notice the improvement of lateral resolution with STED.*

The resolution of STED microscopy can be tuned with the power of the STED beam and, theoretically has no limits except the molecule itself (Figure 3.7).
Mathematically, the resolution of a STED microscope can be written by modifying the Equation (26) as follows:

$$d = \frac{\lambda}{2NA\sqrt{1 + \frac{I}{I_{sat}}}} \tag{5}$$

Where *I* represents the maximum intensity of the STED laser and I_{sat} is the saturation intensity that corresponds to the intensity of the STED laser which is necessary to quench the 50% of the spontaneous emission of the fluorophores.

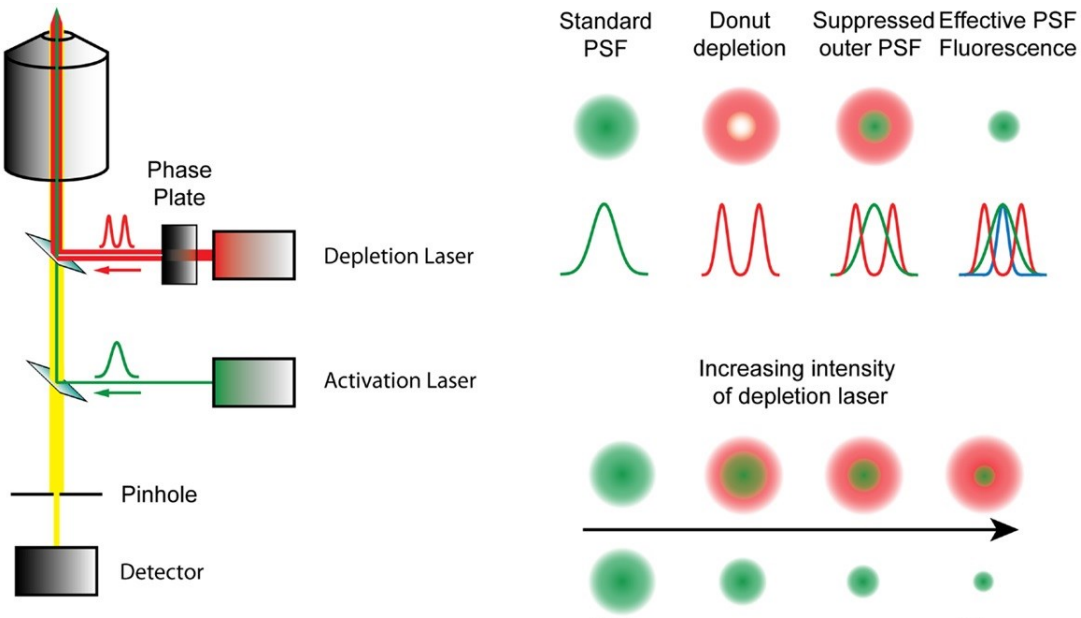

Figure *3.7: simplified architecture of a STED microscope. The resolution improves with the power of the STED beam. Adapted from* [83]. *Copyright © 2013 Hiersemenzel, Brown and Duncan.*

Equation (5) shows that when the intensity *I* of the STED laser approaches or surpasses the saturation intensity I_{sat}, the resolution d improves. The higher the power of the STED laser, the more it restricts the area of fluorescence, thus improving the resolution of the microscope. However, there is a practical limit to how much the intensity *I* can be increased, as extremely high intensities can lead to photobleaching and photodamage to the sample.

3.3 Fluorescence correlation spectroscopy

Fluorescence correlation spectroscopy (FCS) is technique firstly introduced in the 70's ([84]) that provides a way to study the dynamics and interactions of molecules in solution at a single-molecule level. It operates by monitoring fluctuations in the intensity of light emitted by biomolecules as they move in and out of a focused beam of light [85]. Typically, FCS is integrated in confocal setups, therefore the volume in which the molecules diffuse is represented by the confocal volume, usually < 1 fl. This volume is the minimum achievable volume given a certain pinhole size, a wavelength λ and a numerical aperture, hence it is determined by the PSF of the confocal microscope. However, among the many applications of FCS, the most established one is the "single point" FCS, where the confocal volume is not scanning over the sample, but it's in a fixed position.

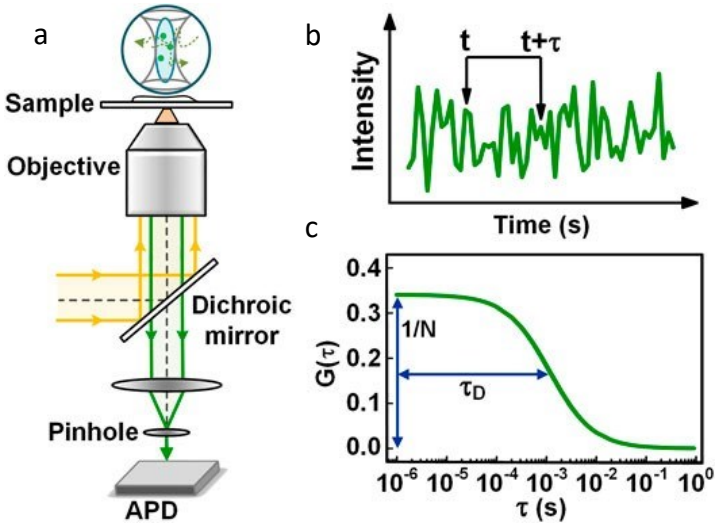

Figure *3.8: a) represent the typical confocal system on which FCS is implemented. The molecule move freely on the sample, and they are detected when they diffuse on the confocal volume. b) example of the intensity fluctuations δF(t) used to generate the autocorrelation function. c) typical autocorrelation curve calculated from the fluctuations. 1/N (ACF amplitude) and τ_D (ACF width) are depicted. From* [85]. *Copyright © 2021 Yu, Lei, Ma, Liu, Zheng, Dan and Gao.*

These fluctuations in fluorescence intensity, while appearing random, are actually spontaneous variations around a mean value. They are indicative of the number of fluorescent particles undergoing motion within the confocal volume. The analysis of these fluctuations is done through an autocorrelation function, which correlates the fluorescence intensity at a given time t with the one at a later time t+τ.

This function reveals several vital parameters: the average number of fluorescent particles N in the focal volume, the diffusion time τ_D and the diffusion coefficient D, a parameter which describes how far a particle can travel via diffusion.

If we define a fluorescence fluctuation as:

$$\delta F(t) = F(t) - \langle F(t) \rangle \tag{6}$$

Where $\langle F(t) \rangle$ is the average intensity at time t, then we can define the normalized autocorrelation function (ACF) as:

$$G(\tau) = \frac{\langle \delta F(t) \delta F(t+\tau) \rangle}{\langle F(t) \rangle^2} \tag{7}$$

The **amplitude** (Figure 3.8) of the correlation curve G(0), is inversely proportional to the average number of fluorescent molecules N within the observed volume:

$$G(0) = \frac{1}{\langle N \rangle} \tag{8}$$

The ACF can also be written as:

$$g(\tau) = \frac{\langle F(t) F(t+\tau) \rangle}{\langle F(t) \rangle^2} = G(\tau) + 1 \tag{9}$$

Such theoretical model has to be aligned with the experimental autocorrelation function that yields the key parameters we want to extract. If we model the diffraction-limited observation volume as a 3D Gaussian profile represented by our PSF, we can describe the $g(\tau)$ by using a 3D diffusion model. This model for a single diffusing species yields:

$$g(\tau) = \frac{1}{N} \cdot \left(1 + \frac{\tau}{\tau_D}\right)^{-1} \cdot \left(1 + \frac{\tau}{\gamma^2 \tau_D}\right)^{-1/2} \tag{10}$$

γ takes account of the size of the confocal volume. In other words:

$$\gamma = \frac{z}{w_{xy}} \tag{11}$$

Where z equals to half of the axial PSF and w_{xy} of the lateral PSF (Figure 3.9).

From Equation (10) we can retrieve τ_D (the diffusion time) that corresponds to the point of inflection of the correlation curve (Figure 3.8). In particular, τ_D is linked to the diffusion time D by the following equation:

$$D = \frac{w_{xy}^2}{4\tau_D} \tag{12}$$

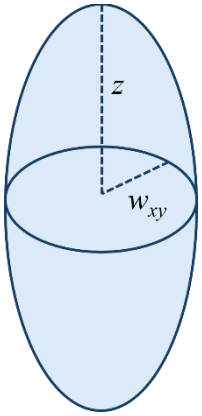

Figure *3.9: schematic representation of the excitation focal volume, i.e. the 3D PSF of the system.*

4. Atomic Force Microscopy

In the early 80's two scientists, G. Binnig and H. Rohrer, worked on a very sophisticated microscope, called Scanning Tunneling Microscope (STM) [86]for which they were awarded with the Nobel Prize in Physics in 1986 [87].
In the very same year G. Binnig (together with C.F. Quate and C. Gerber) published a paper describing a new microscope, which was closely related to the STM, called the Atomic Force Microscope [88]. Both microscopes belong to the class of Scanning Probe Microscopes (SPMs), instruments used to obtain topographical images and information about a surface, at the atomic level. They operate by means of the physical scanning of a probe over the sample.

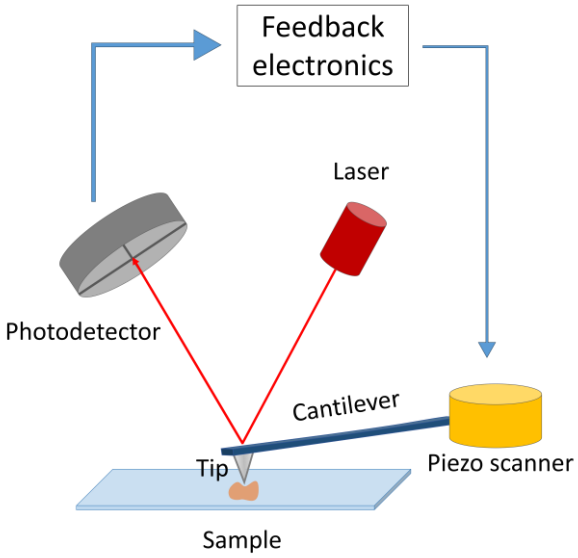

Figure *4.1: schematical representation of the main components of an AFM microscope.*

Specifically, AFM detects the forces between a very sharp nanometric tip, and the atoms of the sample. The tip is attached to a reflective tiny cantilever (typically $\sim 10^2$ µm long and $\sim 10^1$ µm wide) that works as a sensor of the interactions and bends whenever a force is detected. The bending of the cantilever is quantified by means of a laser that hits the cantilever surface and, as a result, is reflected on a four-quadrant photodiode. The vertical or horizontal deflection of the laser is proportional to the bending of the cantilever which, in turn, is sensitive to the forces between the tip and the sample. The vertical movement of the probe is controlled by a closed feedback-loop, which keeps the probe-sample interaction at a constant force. In this way the topography of the sample can be recorded.
In the ideal case, the tip-sample interaction occurs between a single atom from the tip extremity and a single atom on the sample.

The model that describes the interaction between two atoms at a certain distance r is given by the Lennard-Jones potential:

$$V(r) = 4\varepsilon\left[\left(\frac{\sigma}{r}\right)^{12} - \left(\frac{\sigma}{r}\right)^{6}\right] \tag{13}$$

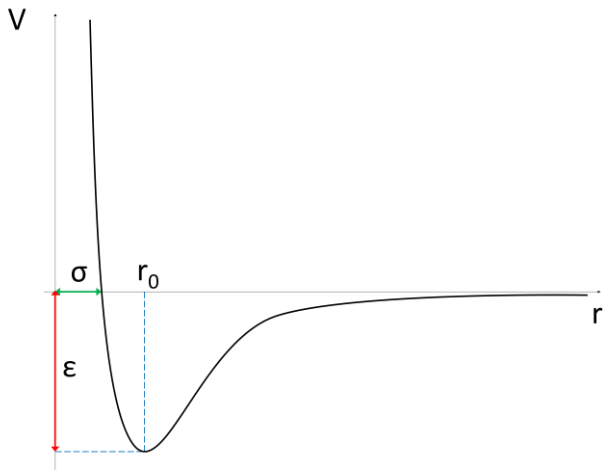

Figure *4.2: representation of the Lennard-Jones potential. ε represents the deepness of the potential well, while σ is the intersection of V(r) with the x axis.*

The first term is positive and goes with r^{-12}. It quantifies the repulsion at short distance, given by the Pauli exclusion principle. The second term that goes with r^{-6} is negative and describes the attractive forces between the atoms that dominate at long distances. The contribution to that term is given by the Van der Waals forces. The minimum of the potential is an equilibrium distance between the atoms and is represented by r_0.
In practical terms, the interaction between the tip and the sample is more complex than that described by this model, and it is also determined by the environement in which the AFM is operating. Indeed, apart from its great spatial resolution, especially on the z-axis where it can distinguish sub-nanometric features [89], one of the most important features of the AFM is the possibility to be implemented in physiological conditions.
In fact, AFM can operate either in **air** or in **liquid** environments, where the latter condition is necessary to study biological samples under native conditions.
To operate in two different environments, it's necessary to carefully pick the right cantilevers. In fact, the force which the probe exerts on the sample is dependent on the physical characteristics of the cantilever, that determine its tendency to bend.

The rigidity of the cantilever is determined by its **spring constant** k and the force exerted on the sample can be written as:

$$F = k\Delta x \tag{14}$$

Hence, F is linearly proportional to the rigidity of the cantilever, which is determined by the spring constant k.
More rigid cantilevers (k = 20 - 50 N/m) are good for imaging in air, on the contrary low spring constant cantilevers (k = 0.06 - 0.3 N/m) are recommended for imaging in liquid.
Atmospheric air has always a certain concentration of water vapour which can cause adhesion forces between the tip and the samples that are very difficult to overcome with soft cantilevers. On the other hand, imaging in liquid always raises a certain degree of hydrodynamic friction (damping), which is much higher with rigid cantilevers; in this case the employment of soft cantilevers is the best choice.
Depending on the sample to image and on the specific application, there are many modalities that can be implemented on a AFM setup. Among them the **contact** mode was the first ever to be employed. In contact mode, the AFM probe is in constant physical contact with the sample surface during scanning. The cantilever bends as it traces the surface topography, maintaining a constant force between the tip and the sample. Such constant contact is not ideal in the context of imaging soft biological samples, since it may cause physical damage. A way to overcome this problematic is to use other gentler modalities. The ones that we will see in the course of this thesis are **tapping** mode, **QI** (Quantitative Imaging) and **Jumping** mode. Tapping mode is a modality in which the cantilever is made to oscillate at its resonance frequency. This feature allows the tip to touch the sample by gently tapping it, reducing the lateral dragging forces. QI and Jumping mode are very similar modalities in which the probe taps the surface and records spectroscopic data, i.e. a **Force-Distance (F-D)** curve. An F-D curve plots the forces sensed by the probe as it approaches, contacts, and then retracts from a surface. These curves are used to acknowledge the mechanical properties of the sample, and they are interesting especially for deformable soft samples, rather than “infinitely rigid” materials. In fact, as the tip touches a soft sample it exerts a certain pressure (or **indentation**) that can be able to deform it. Getting to know the entity of such deformation is important for example to assess the rigidity of a sample. Another important aspect of the sample that can be traced by F-D curves is the presence of **adhesion** forces. In fact, as the tip retracts, it can reveal attractive Van der Waals forces that are a sign of stickiness of a material.
The possibility of having spectroscopic data along with an image is indeed another significant hallmark of AFM.

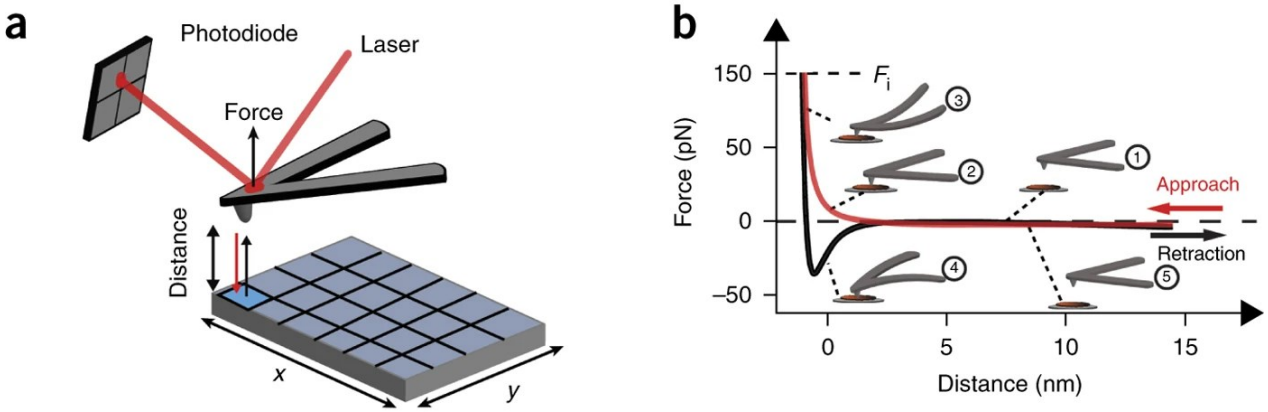

Figure *4.3: a) illustration of the interaction between the tip and the sample and b) an example of either approach and retract F-D curves. All the phases of the interaction are depicted in temporal order from 1 to 5. Adapted with permission from Springer Nature* [90]. *Copyright © 2014, Springer Nature Limited.*

5. AFM-Fluorescence correlative microscopy

We described fluorescence microscopy techniques and AFM. Those methodologies are very powerful tools to study biological samples at the nanoscale. As a matter of fact, the two techniques retrieve distinct information from the sample. AFM has the advantage to be a label-free technique, that provides detailed topographical and mechanical properties of the surface of a sample at the nanometer scale. However, AFM doesn't have any chemical specificity on the sample. Fluorescence microscopy has typically a slightly worse spatial resolution than AFM and it needs fluorophores to have a contrast. On the other hand, it has the advantage to be chemically specific, allow for optical sectioning and have a faster acquisition time than AFM.

Combining the two techniques is essential for addressing questions related to morphology at a sub-diffraction level, complemented by the specific and functional information of fluorescence [91] and to compensate for each other's limitations.

In addition, in recent years it has been possible to combine them in the very same platform (Figure 5.1) leading to a more efficient correlative imaging. In this way it's feasible to obtain images of the very same ROI in a sample in a sample. Usually, a sample is first imaged using fluorescence microscopy and then the same sample area is scanned with AFM to provide a high-resolution topographical map.

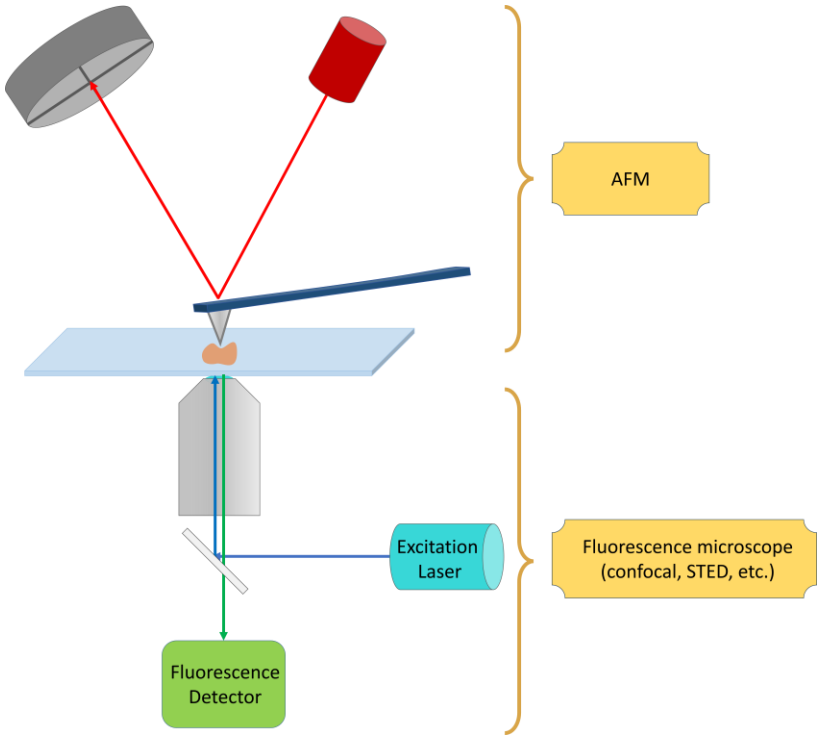

Figure *5.1: illustration of a system in which an AFM and a fluorescence inverted microscope are integrated. This is a scheme of the system that we used in the correlative measurements that we will show in the thesis.*

PART 2 : Results

1. SARS-CoV-2

We mentioned the importance of the usage of broad-spectrum antivirals in therapy. Molecules that hit indistinctively many targets, or a common target from different pathogens, can be more effective compared to drugs exploiting only a specific interaction. A common feature like the viral envelope can be exploited for such purpose. Hypericin (Hyp), a potent natural photosensitizer that we already described, is a promising candidate. It has been extensively studied and it demonstrated significant inactivation of various viruses upon exposure to visible light, including some efficacy under dark conditions. Notably, its effectiveness is contingent on its aggregation state. In fact, monomeric Hyp, stabilized by suitable organic solvents such as ethanol or DMSO, generates singlet oxygen and other reactive oxygen species upon photoexcitation but is inactive in water, where its low solubility leads to formation of molecular aggregates. However, its photoactivity in aqueous media can be restored when it binds to other species, preventing aggregation, such as membranes or proteins with hydrophobic pockets. Binding affinity, alongside the intrinsic heterogeneity of single viral particles, influences Hyp's overall efficacy. Addressing the behavior of individual viral particles is gaining attention for improving antiviral drugs.

Despite Hyp-based antiviral treatments proposed earlier, quantitative measurements regarding binding affinity and loading on single viral particles are lacking. Our study began trying to answer such questions, by using SARS-CoV-2 as an enveloped virus, and employing fluorescence spectroscopy and microscopy. Moreover, some viral assays were also performed, in order to demonstrate the inactivation of the virus under photoactivation and dark conditions.

1.1 Hypericin binding to SARS-CoV-2

Before trying to assess which were the photodynamic effects of Hyp, we had to confirm whether the molecule was binding to the virus and at which efficiency. The hydrophobic core of Hyp facilitates extended aggregation in aqueous solvents, and as a result in this conditions Hyp is inactive from a photo-physics standpoint. In fact, even though it absorbs visible photons when aggregated, molecular excited singlet and triplet states are rapidly quenched, resulting in minimal fluorescence emission and negligible generation of reactive oxygen species.

The presence of viral particles, and in particular of a phospholipidic environment (i.e. the viral envelope) solubilize Hyp, leading to a significant recovery of fluorescence emission upon photoexcitation.

To assess the impact of SARS-CoV-2 particles on Hyp fluorescence emission, viral particles were initially fixed with formaldehyde, washed, and concentrated through ultracentrifugation.

Figure 1.1a illustrates the interaction of Hyp molecules with SARS-CoV-2 particles in an aqueous environment: the presence of viral particles solubilizes Hyp aggregates, allowing virus-bound Hyp molecules to regain significant fluorescence emission upon photoexcitation, as qualitatively

confirmed by fluorescence spectroscopy measurements. Furthermore, the high fluorescence anisotropy of Hyp exposed to SARS-CoV-2 particles (Figure 1.2) suggests the prevention of rotational averaging, as expected for a fluorophore bound to a bulky viral particle.

Fluorescence emission was then employed to directly visualize the loading of Hyp on SARS-CoV-2 particles through fluorescence microscopy.

In an initial imaging experiment, previously fixed SARS-CoV-2 particles were incubated with Hyp in an aqueous buffer, subsequently seeded on a glass coverslip, and imaged with a confocal microscope.

Confocal images reveal concentrated Hyp emission in bright fluorescent spots, indicating binding to SARS-CoV-2 particles. Due to the limited spatial resolution of a confocal setup, particles loaded with Hyp exhibit indistinct fluorescent spots, making it challenging to definitely determine whether they exist isolated or form small clusters. Therefore, to achieve higher spatial resolution, STED microscopy was applied. Panels b and c of Figure 1.1 show images obtained with confocal and STED microscopy, respectively, demonstrating increased resolution and improved discrimination of single viral particles, even in small clusters.

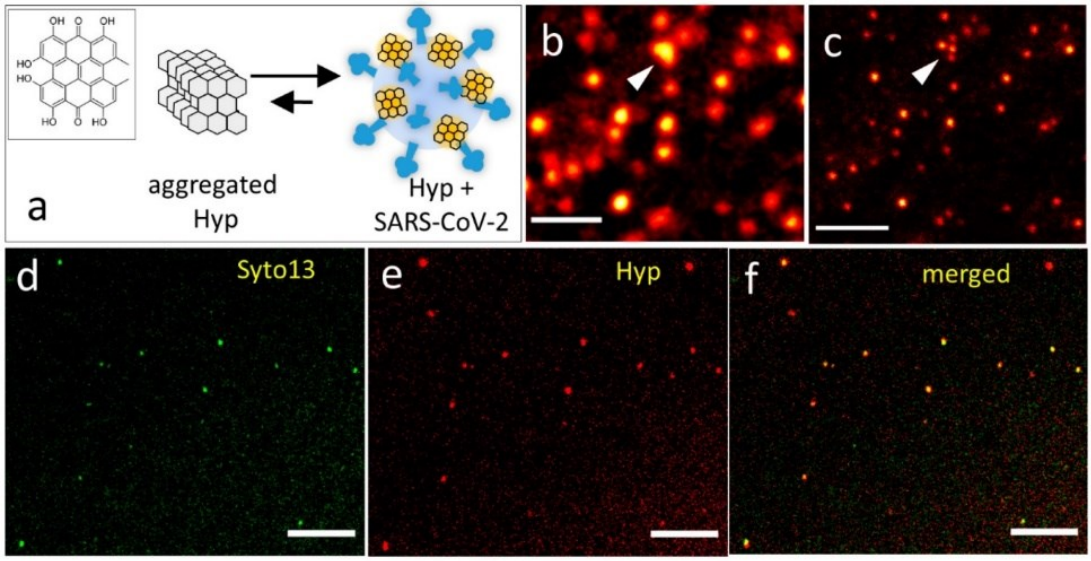

Figure *1.1: a) illustration of Hyp interaction with SARS-CoV-2 in aqueous solution: aggregated Hyp (left) is non-fluorescent, while Hyp bound to SARS-CoV-2 particles (right) exhibits fluorescence. The inset displays the chemical structure of Hyp. b,c) Confocal (b) and corresponding STED (c) images of SARS-CoV-2 particles exposed to Hyp (red). Arrows highlight a cluster of viral particles, clearly resolved through STED Imaging. Scale bars: 500 nm. d–f) Confocal images of the same FOV illustrating SARS-CoV-2 particles labeled with the RNA probe Syto13 and Exposed to Hyp. Separate channels for Syto13 (d, green) and Hyp (e, red) are presented, along with the merged two-color image (f), displaying overlapping regions in yellow. Scale bars: 5 µm.*

To show that Hyp attaches to intact virions containing RNA, we carried out a second imaging experiment. In this setup, SARS-CoV-2 particles that had been fixed beforehand were stained with Syto13, a nucleic acid labeling dye, and then treated with Hyp. These particles were

subsequently placed onto a glass coverslip and observed using a confocal microscope. Due to the distinct emission spectra of Hyp and Syto13, it was possible to concurrently visualize both within the same field of view. In both images, the emissions from Syto13 (Figure 1.1d−f) and Hyp (Figure 1.1e) appear as bright spots of a size limited by diffraction, and a significant number of these spots overlap in the two detection channels (Figure 1.1f). This overlap provides evidence that Hyp predominantly attaches to intact SARS-CoV-2 particles that contain RNA. The small proportion of fluorescent spots that do not overlap may be due to the incomplete staining of viral RNA with Syto13. However, the possibility of some particles being debris or slightly damaged cannot be completely discounted.

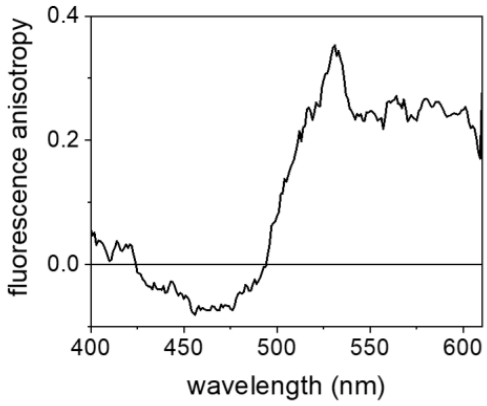

Figure *1.2: fluorescence anisotropy on a solution of 50 nM Hyp and ∼1 nM SARS-CoV-2 particles. The observed data indicate that when Hypericin is mixed with the viral particles, it becomes solubilized and exhibits its distinctive fluorescence emission. The presence of non-zero anisotropy suggests that the rotational movement of Hyp molecules is restricted, which is likely a result of their interaction with the large viral particles.*

1.2 Hypericin Affinity for the viral envelope

To further explore how Hyp interacts with SARS-CoV-2, we used FCS to analyze SARS-CoV-2 particles after exposure to varying concentrations of Hyp, from 1 to 100 nM. With FCS it's possible to assess the levels of fluorescent molecules in a solution and determines their 3D diffusion properties. As unbound Hyp lacks fluorescence, the detected diffusing species correspond to viral particles loaded with Hyp. A representative FCS correlation curve is depicted in Figure 1.3a. Fitting the FCS curves confirmed the presence of slow-diffusing particles (average diffusion coefficient D = (2.4 ± 1.2) μm²/s), with a hydrodynamic diameter of approximately 150 nm, aligning with the expected size of SARS-CoV-2. The concentration of Hyp-loaded viral particles, determined from the amplitude of correlation curves, was roughly 1 nM, displaying some variability attributed to the presence of rare, challenging-to-remove species with slower diffusion, such as aggregates or residual debris.

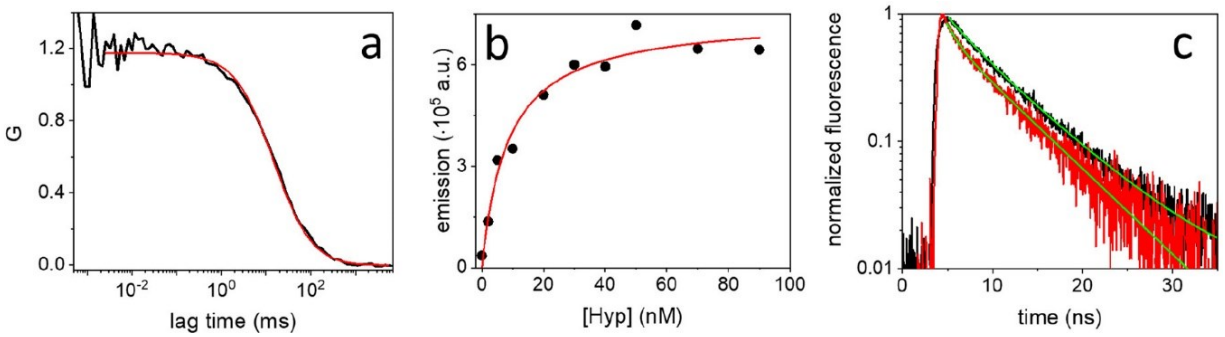

Figure *1.3: a) this figure shows a representative FCS correlation curve (black) obtained from a solution containing SARS-CoV-2 particles treated with 5 nM Hyp. The fitting of this data, depicted in red, was done using a model for a single diffusing species. b) This part illustrates the integrated fluorescence emission of Hyp at progressively increasing concentrations, while maintaining a constant amount of SARS-CoV-2 particles (black circles). The fitting of these data points, shown in red, was conducted using a binding model. c) Displayed here are the normalized time-resolved fluorescence decays for Hyp when it is bound to DLPC liposomes (black) and to SARS-CoV-2 particles (red). The green lines indicate the fitting results, which were done using a biexponential model for both sets of decay data.*

Subsequently, the same solutions were subjected to a fluorometer to measure ensemble fluorescence emission. Figure 1.3b illustrates the total emission (black circles) obtained by integrating the entire emission spectrum at increasing concentrations of Hyp (0–90 nM) and constant SARS-CoV-2 particle concentration (~1 nM, as determined by FCS). The observed fluorescence sharply rises between 0 and 20 nM of Hyp, appearing to saturate at about 30-40 nM. Beyond this concentration, the SARS-CoV-2 particles reach their capacity for binding additional Hyp, leading to the formation of non-fluorescent aggregates. Using the concentration of SARS-CoV-2 particles determined from FCS, we estimated the saturation molar ratio to be around 30:1 (Hyp to SARS-CoV-2). Additionally, by fitting the experimental data to a pre-established equation, we quantified the binding affinity of Hyp to SARS-CoV-2 particles,

determining an apparent equilibrium dissociation constant (K_D) of 8.5 nM at this specific virus concentration.

Figure 1.3c displays the normalized fluorescence decay profiles for 5 nM Hypericin (Hyp) bound to approximately 1 nM SARS-CoV-2 particles (shown in red), and for 10 nM Hyp bound to approximately 2 nM DLPC liposomes (depicted in black), which act as a comparative model for the membrane context. These measurements are made at concentrations significantly lower than saturation levels, where individual Hyp molecules bound are sufficiently spaced apart, making their interactions with other Hyp molecules on the same particle negligible. Visually, the decay curves in Figure 1.3c are strikingly similar, with notable differences primarily in the initial phase of the decay. Both sets of data were most accurately modeled using a biexponential function, resulting in two distinct lifetimes (τ_1 and τ_2) for Hyp bound to either SARS-CoV-2 particles or liposomes. While the longer lifetimes (τ_2) are consistent across both, the shorter lifetimes (τ_1) show variation. The longer lifetime is indicative of a large population of Hyp molecules situated in a microenvironment less polar than water, common to both liposomes and viruses, likely within the phospholipid bilayer. In contrast, the shorter lifetime components may reflect molecules that are more exposed to the aqueous surroundings, possibly near membrane proteins.

Hyp in:	*τ_1(ns)*	*τ_2(ns)*
SARS-CoV-2 particles	1.2 ± 0.1	6.3 ± 0.3
DLPC liposomes	2.3 ± 0.5	6.8 ± 0.4

In fact, Hyp might bind to spike proteins, particularly to the exposed receptor binding domain (RBD) of the spike protein, on the surface of SARS-CoV-2 particles. We utilized a recombinant soluble version of RBD to investigate Hyp's potential specific binding. FCS measurements on Hyp exposed to RBD revealed no binding to monomeric RBD in the nanomolar concentration range. However, high-affinity binding ($K_D \sim 60$ nM) was observed for large RBD aggregates at low concentrations, which do not correspond to the biologically relevant monomeric state of these proteins.

While the primary binding target of Hyp appears to be the viral envelope, the possibility of lower-affinity interactions with other viral proteins cannot be completely ruled out, although they are less likely at the employed concentrations.

1.3 Hypericin Distribution on SARS-CoV-2 Particles

Fluorescence emission in this study originates solely from Hyp bound to SARS-CoV-2 viruses, meaning the emission intensity from a single virus particle is approximately proportional to the number of Hyp molecules it contains. This allows for the discernment of variations in Hyp content on individual SARS-CoV-2 particles using fluorescence imaging. To facilitate this, viral particles (around 1 nM) were first incubated with various Hyp concentrations (5−90 nM) and then placed on a glass coverslip without washing. A consistent amount of PBS buffer was added before imaging to ensure optimal visualization, complete glass surface coverage, and maintenance of the Hyp:virus ratio. Figure 1.4a shows a typical image from this procedure.

The analysis of these images involved quantifying the emission intensity from single viral particles. Initially, a threshold was set to identify bright spots, corresponding to particles with an intensity above the background level, which included detector noise and residual Hyp sticking to the glass. The intensities of the identified particles were then categorized to construct the probability distributions shown in Figure 1.4b.

These distributions primarily feature viral particles with intensities between 430 and 500 arbitrary units (au), along with a tail of higher intensity values. Particles with intensities below around 400 au were indistinguishable from the background (see Figure S8), and those just above this threshold (400−430 au) showed more variability across different images. The distributions in Figure 1.4b lack a distinct shape, indicating a heterogeneous distribution of Hyp across individual viral particles. This variation likely results from the random nature of the binding process and potential differences in membrane surface accessibility among individual particles.

While the method for sampling individual viral particles is direct, it faces sensitivity challenges at very low Hyp concentrations (<10 nM), where emission from a single particle is due to only a few molecules, and some particles may remain unlabeled and invisible to fluorescence imaging. More intricate techniques, such as correlative light and electron microscopy, would be required for a thorough sampling that includes unlabeled or faintly emitting particles. Nonetheless, a trend is observable by examining average single-particle intensity values derived from the distributions (Figure 1.4c). These averages show a qualitative increase in intensity with rising Hyp concentration. Despite considerable variability, fitting these data with the same model as in Figure 1.3b yields an apparent KD of 7 nM (Figure 1.4c, in red), aligning with the bulk measurement results. Importantly, this kind of data on drug loading at the single-viral-particle level is unattainable with ensemble measurement methods.

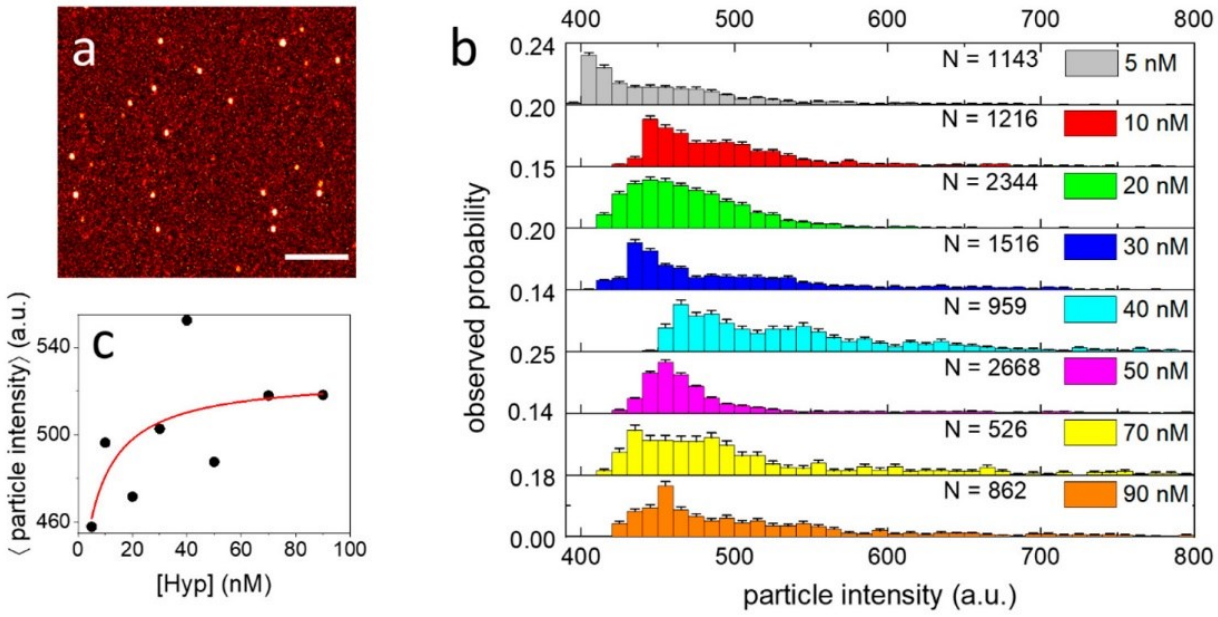

Figure *1.4: a) this is a representative image showing SARS-CoV-2 particles after exposure to Hyp for single-particle intensity analysis. The scale bar in the image is 5 µm. b) The image displays probability distributions of single viral particle fluorescence intensities for SARS-CoV-2 particles exposed to various concentrations of Hyp: 5 nM (gray), 10 nM (red), 20 nM (green), 30 nM (blue), 40 nM (cyan), 50 nM (magenta), 70 nM (yellow), and 90 nM Hyp (orange). 'N' indicates the total number of viral particles analyzed in each distribution. The width of each distribution bin is set at 10 a.u. c) The graph illustrates the average fluorescence intensity values of single viral particles at increasing concentrations of Hyp. The red line in the graph represents the outcome of the fitting process using a binding model. The Hyp concentrations mentioned correspond to those used during incubation with the SARS-CoV-2 particles.*

1.4 Effectiveness of Hypericin Against SARS-CoV-2

To assess the effectiveness of Hyp against SARS-CoV-2, viral infectivity assays were conducted. In these experiments, active SARS-CoV-2 particles underwent initial incubation with Hyp at concentrations of 3, 30, and 300 nM. Subsequently, samples were subjected to either dark conditions or irradiated with blue light to photoexcite Hyp, enabling the differentiation of both dark and photoinduced effects. Following treatment, viral samples were serially diluted and incubated with a monolayer of Vero E6 cells under dark conditions to determine residual infectivity. The 50% tissue culture infective dose per mL (TCID50/mL), representing the viral titer at the dilution where cell viability is reduced by 50%, was then measured.

Figure 1.5 provides a summary of the measured TCID50/mL values for viruses incubated with Hyp under dark conditions (red bars) or photoexcited conditions (blue bars). Reference values (TCID50/mL ~ 10^5, gray bars) were obtained for fully infective viral samples that were not treated with Hyp but were directly incubated with Vero E6 cells after serial dilution.

Under the employed conditions, a remarkable reduction in infectivity (TCID50/mL from 105.5 to <101) was observed for SARS-CoV-2 exposed to both 300 and 30 nM Hyp and photo-irradiated.

A clear antiviral effect was evident even at 3 nM Hyp, upon light exposure, causing a 2.2-log reduction in viral titer (TCID50/mL from $10^{5.2}$ to 10^3) compared to untreated viruses. These results

affirm that even low concentrations of photoexcited Hyp are effective against SARS-CoV-2, consistent with the observed high affinity of Hyp for viral particles.

This efficacy of Hyp compares favorably with recently reported photoinactivation studies on SARS-CoV-2 using methylene blue and radachlorin as photosensitizing molecules.

Antiviral activity was also observed under dark conditions, albeit to a lesser extent than in photoexcited samples. In the dark, infectivity reduction was negligible for viruses exposed to 3 nM Hyp (TCID50/mL $10^{5.5}$) and moderate for viruses exposed to 30 nM Hyp (TCID50/mL from $10^{5.5}$ to $10^{4.6}$). Significantly, at 300 nM Hyp, a 3-log reduction in TCID50/mL value (from $10^{5.5}$ to $10^{2.5}$) was induced compared to untreated viruses. Importantly, no toxicity was observed in control experiments conducted on Vero E6 cells exposed to Hyp or DMSO, in the absence of viruses and in the dark, confirming that cells are not directly damaged by Hyp or the small amount of DMSO added to deliver Hyp. To evaluate Hyp's effectiveness against SARS-CoV-2, viral infectivity assays were performed. In these tests, active SARS-CoV-2 particles were first incubated with Hyp at 3, 30, and 300 nM concentrations. The samples were then either kept in dark conditions or exposed to blue light to activate Hyp, allowing for the observation of effects both in the absence and presence of light. Post-treatment, these viral samples were diluted serially and added to a monolayer of Vero E6 cells, maintained in dark conditions, to assess remaining infectivity. The viral concentration causing a 50% reduction in cell viability (TCID50/mL) was measured.

Figure 1.5 presents the TCID50/mL values for viruses treated with Hyp in the dark (shown with red bars) and under light activation (blue bars). For comparison, reference values (TCID50/mL ~ 10^5, gray bars) were obtained from fully infective viral samples that hadn't been treated with Hyp but were directly incubated with Vero E6 cells after dilution.

Under these experimental conditions, a significant decrease in infectivity was noted for SARS-CoV-2 exposed to 300 and 30 nM Hyp and then photo-irradiated, with TCID50/mL values dropping from $10^{5.5}$ to less than 10^1. Even at 3 nM Hyp with light exposure, a notable antiviral effect was seen, evidenced by a 2.2-log reduction in viral titer (TCID50/mL from $10^{5.2}$ to 10^3) compared to untreated viruses. These findings confirm the efficacy of photoactivated Hyp against SARS-CoV-2, even at low concentrations, aligning with its high affinity for the virus.

The effectiveness of Hyp in these conditions is comparable to or even surpasses other photoinactivation studies on SARS-CoV-2 using different photosensitizers like methylene blue and radachlorin.

Antiviral activity was also observed without light exposure, though it was less pronounced than in photoexcited samples. In darkness, the infectivity reduction was minimal for viruses treated with 3 nM Hyp (TCID50/mL $10^{5.5}$) and moderate for 30 nM Hyp (TCID50/mL from $10^{5.5}$ to $10^{4.6}$). Notably, a substantial 3-log reduction in TCID50/mL (from $10^{5.5}$ to $10^{2.5}$) was seen with 300 nM Hyp compared to untreated viruses. Importantly, control experiments with Vero E6 cells exposed

to Hyp or DMSO in the absence of viruses and light confirmed no direct cellular toxicity, ensuring that the observed effects were specific to the viral interaction with Hyp.

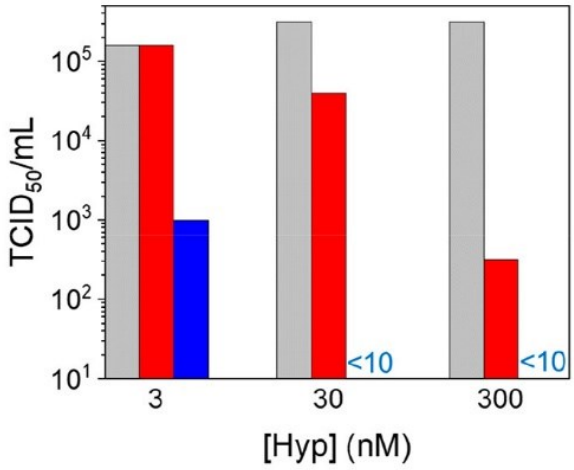

Figure *1.5: the graph illustrates the Viral Titer, measured in TCID50/mL, on Vero E6 cells infected with SARS-CoV-2 viruses that were previously exposed to rising concentrations of Hyp. The samples were either kept in the dark (depicted in red) or irradiated with 20 J/cm² of blue light (depicted in blue). Reference TCID50/mL values obtained from Vero E6 cells infected with SARS-CoV-2 but not exposed to Hyp are represented in gray.*

1.5 Conclusions

These results highlight the dual-action nature of Hyp as an antiviral agent, resolving the inconsistencies seen in previous reports. When photoactivated while bound to the virus, Hyp likely induces substantial damage to the viral particles through the generation of reactive oxygen species, a phenomenon noted in similar studies. Since a single Hyp molecule can absorb multiple photons during treatment, this process requires only a limited number of Hyp molecules on each viral particle to be effective. In contrast, the absence of light suggests an alternative mechanism for the observed reduction in viral infectivity. This dark mechanism seems to require a higher concentration of Hyp on the viral particles to be significant. One hypothesis is that Hyp's integration into the viral envelope might interfere with its fluidity, subsequently increasing the energy barriers needed for the virus to fuse with host cell membranes. However, further research is necessary to fully understand these mechanisms and their potential combined effects.

1.6 Material and methods

1.6.1 Fluorescence microscopy.

The colocalization measurements shown in Figure 1d–f and the single-particle intensity analysis illustrated in Figure 1.4 were performed using a Nikon A1MP inverted confocal microscope. This microscope is equipped with four excitation lasers at 405, 488, 561, 640 nm wavelengths, and it incorporates three alkaline photomultiplier tubes (PMTs) for detection. Specifically, for these experiments, Hyp was excited with the 561 nm laser and Syto13 with the 488 nm laser. The 561 nm laser is a continuous-wave diode-pumped solid-state laser from Melles Griot, while the 488 nm laser is a continuous-wave diode semiconductor laser from Coherent. Fluorescence emissions were detected using two different bandpass filters: a 605/70 nm filter for Hyp and a 515/30 nm filter for Syto13.

STED imaging, as presented in Figures 1b and c, was conducted using the Leica Microsystems STELLARIS 8 STED system. This microscope features a supercontinuum White Light Laser (WLL) in excitation, and for these particular measurements, an excitation wavelength of 561 nm was selected using an Acousto-Optical Tunable Filter (AOTF). The STED wavelength was 775 nm.

Sample preparation. The stock suspension containing fixed viral particles was initially centrifuged for 3 minutes at 5000 rpm to eliminate the largest aggregates. The viral particles were then diluted 50-fold in PBS buffer with a pH of 7.4.

For single-particle intensity measurements (referenced in Figure 1.4), pre-diluted viral particles were combined with various concentrations of Hyp (ranging from 5 to 90 nM). 20 µL of each mixture was then placed on a sterile cell culture dish with a glass bottom. Following a 10-minute incubation period, 100 µL of PBS was added directly, without any intermediate washing steps, to achieve the desired volume for imaging. This volume ensures uniform coverage of the glass surface with the solution. The sample was then sealed to prevent evaporation and imaged immediately. This procedure was consistently applied to all samples to ensure comparability.

For the colocalization measurements (as in Figure 1.1d–f), pre-diluted viral particles were first mixed with Hyp (to a final concentration of 50 nM), then added to a sterile cell culture dish and combined with Syto13 (also to a final concentration of 50 nM). These samples were imaged immediately without any intermediate washing steps, using a sequential scanning mode to avoid bleed-through during the acquisition process.

In all samples, the final concentration of DMSO was kept negligible (<2%).

1.6.2 Spectroscopy

Absorption spectra were obtained using a Jasco V-650 spectrophotometer from Jasco Europe. For steady-state fluorescence excitation, emission, and anisotropy measurements, we utilized the SF5 spectrofluorometer (Edinburgh Instruments Ltd., Livingston, U.K.) This instrument is fitted with both excitation and emission polarizers, which facilitate the detection of fluorescence anisotropy.

Sample preparation. We first centrifuged the stock suspension of fixed viral particles for 3 minutes at 5000 rpm to remove larger aggregates. The particles were then diluted 50-fold in PBS buffer with a pH of 7.4. A small volume of Hyp concentrated in DMSO was added to the suspension, achieving a concentration 50 times higher than the desired final concentration, resulting in a final DMSO concentration of 2%. After a 5-minute incubation period at room temperature in dark conditions, 50 µL of this mixture was transferred into a quartz cuvette with a path length of 0.3 cm for fluorometric analysis. Emission spectra were acquired by exciting the sample at 553 nm, while for excitation and anisotropy spectra, emission was collected at 650 nm.

1.6.3 Fluorescence Correlation Spectroscopy.

Fluorescence Correlation Spectroscopy (FCS) experiments were conducted using a Microtime 200 system from PicoQuant. This system integrates an inverted confocal microscope (Olympus IX71) and is equipped with two Single Photon Avalanche Diodes (SPADs) operating in cross-correlation mode. For the excitation of Hypericin (Hyp), we employed a 475 nm picosecond diode laser, which was operated at a frequency of 20 MHz. The fluorescence emission from Hyp was captured through a 675/25 nm bandpass filter and then equally divided between two detection channels using a 50/50 beam splitter. This configuration enabled the simultaneous recording of both correlation curves and time-resolved fluorescence decays. These decays were measured using the technique of time-correlated single photon counting (TCSPC), providing detailed insights into the fluorescence characteristics of Hyp when interacting with the target.

Sample preparation.

Around 40 µL of the same solution prepared for spectroscopic analysis was employed in the FCS system. Each measurement was conducted over a period of 5 minutes, with multiple repeats (3–5 times) for each sample to ensure reliability. The preparation of all samples followed the same method, and measurements were carried out under uniform conditions. The use of low sample concentrations was critical to ensure that the measurements were not affected by potential artifacts arising from the optical density of the samples at the excitation wavelength.

The analysis of the collected data was performed using SymphoTime software, developed by PicoQuant. The time-resolved fluorescence decays were effectively modeled using a biexponential fit, providing detailed insights into the fluorescence characteristics of the sample.

Similarly, the correlation curves were accurately fitted with a model that assumes a single type of diffusing species. This approach was in line with the theoretical framework and equations used in the study, ensuring a comprehensive and accurate interpretation of the FCS data.

1.6.4 Single-Particle Intensity Analysis

The single-particle intensity data presented were obtained using consistent parameters, including a 1024 × 1024 image size, a pixel dwell time of 6.2 µs, a pixel size of 80 nm, and 4 line averages. The acquisitions were performed with a comparable axial position of the focal plane. For each sample, 8–10 acquired images underwent analysis using ImageJ.

The analysis involved a sequential process. Initially, a Gaussian filter with a standard deviation (σ) of 180 nm was applied to diminish uncorrelated background noise and enhance the discrimination of fluorescent particles. Instances where certain portions of the images were notably out of focus, likely due to irregularities on the glass surface, were excluded from the analysis.

Subsequently, a particle analyzer tool was employed, recognizing particles with a circularity in the range of 0.9-1, a minimum intensity above a threshold value (ranging from 400 to 420 arbitrary units), and a minimum area (8–10 pixels). The results of this analysis were subjected to visual inspection, and particles (<1%) displaying unrealistic features, such as those indicative of aggregates, were excluded.

Finally, the mean intensity values of each selected particle were stored and utilized for the reconstruction of distributions.

1.6.5 Viral Infectivity Assays and Virus Fixation

The isolation of the SARS-CoV-2 virus and subsequent experiments to assess the antiviral efficacy of Hyp against SARS-CoV-2-infected cells were conducted within biosafety level 3 (BSL3) laboratories at the virology department in Istituto Zooprofilattico Sperimentale of Emilia Romagna and Lombardia. The virus isolation process involved the inoculation of an infected biological human sample into Vero E6 cell lines. The SARS-CoV-2 HCoV-19/Italy/310902/46/2020 strain (GISAID code: EPI_ISL_9011947), belonging to clade 20A (Nextstrain naming), was propagated in the same cell line and incubated at 37 °C with 5% CO2. The viral titer (TCID50/mL) was verified using the Reed-Muench assay. To investigate the antiviral efficacy of Hyp, different Hyp concentrations were prepared by diluting Hyp in DMSO.

Three experiments were performed at concentrations of 300, 30, and 3 nM of Hyp. For each Hyp concentration tested, five samples were prepared: SARS-CoV-2 + Hyp light, SARS-CoV-2 + Hyp dark, SARS-CoV-2, Hyp, and DMSO.

In the experimental setup, 900 µL of viral suspension was mixed with 100 µL of Hyp to achieve the desired Hyp concentration. One aliquot of this mixture underwent lamp illumination for 15 minutes with an intensity of 22 mW/cm^2, corresponding to a fluence of 20 J/cm^2 (SARS-CoV-2 +

Hyp light). Another aliquot of the same mixture was kept in the dark for the same duration to assess dark effects (SARS-CoV-2 + Hyp dark).

Two additional control samples were included: 900 µL of Dulbecco's Modified Eagle Medium (DMEM) with 100 µL of Hyp (Hyp) and 900 µL of DMEM with 100 µL of DMSO (DMSO). These controls were designed to evaluate the potential cytotoxic effects of Hyp and DMSO on the Vero E6 cell line. Lastly, a virus reference sample comprising 900 µL of virus with 100 µL of DMEM (SARS-CoV-2) was included to verify the actual virus titer used in the experiment.

The prepared samples (SARS-CoV-2 + Hyp light, SARS-CoV-2 + Hyp dark, and SARS-CoV-2) were inoculated into 96-well plates with preformed monolayer Vero E6 cells (>85%) in 10-log dilutions from dilution −1 to −8. The virus titer was calculated using the Reed and Muench method and expressed as TCID50/mL. Control samples Hyp and DMSO were inoculated into 24-well plates of Vero E6 cells to assess potential toxicity of Hyp and DMSO on Vero E6 cells.

For the fixation of SARS-CoV-2 virions, the culture medium from infected Vero E6 cells, inoculated as described above, was collected at 72 hours after infection. The medium was clarified by centrifugation at 3200g for 20 minutes and fixed with 4% formaldehyde for 30 minutes at room temperature. The fixed SARS-CoV-2 virions were concentrated from the medium by ultracentrifugation through a 20% (w/w) sucrose cushion (120 minutes at 147,000g in a Beckman TY50.2 Ti rotor; Beckman Coulter Life Sciences). Pelleted particles were resuspended in PBS and stored in aliquots at −80 °C.

The isolation of the SARS-CoV-2 virus and the subsequent experiments to evaluate the effectiveness of Hyp against SARS-CoV-2-infected cells were conducted in the biosafety level 3 (BSL3) laboratories of the Virology Department at the Istituto Zooprofilattico Sperimentale of Emilia Romagna and Lombardia. The process of virus isolation involved introducing an infected human biological sample into Vero E6 cell lines. The SARS-CoV-2 strain HCoV-19/Italy/310902/46/2020 (GISAID code: EPI_ISL_9011947), was cultivated in the same cell line and maintained at 37 °C in a 5% CO2 atmosphere. The viral titer, expressed as TCID50/mL, was determined using the Reed-Muench method.

To assess the antiviral properties of Hyp, we prepared different concentrations of Hyp by diluting it in DMSO. Experiments were carried out with Hyp at concentrations of 300, 30, and 3 nM. For each concentration, five sample types were prepared: SARS-CoV-2 with Hyp exposed to light (SARS-CoV-2 + Hyp light), SARS-CoV-2 with Hyp kept in the dark (SARS-CoV-2 + Hyp dark), SARS-CoV-2 alone, Hyp alone, and DMSO alone.

In the experimental setup, 900 µL of the viral suspension was mixed with 100 µL of Hyp to achieve the intended concentration. One portion of this mixture was exposed to lamp illumination for 15 minutes with an intensity of 22 mW/cm2, which corresponds to a fluence of 20 J/cm2 (SARS-CoV-2 + Hyp light). Another portion was kept in darkness for the same time period to observe any effects without light exposure (SARS-CoV-2 + Hyp dark).

Two control samples were included: one consisting of 900 µL of Dulbecco's Modified Eagle Medium (DMEM) mixed with 100 µL of Hyp (Hyp control) and another with 900 µL of DMEM and 100 µL of DMSO (DMSO control). These controls were set up to check for any cytotoxic effects of Hyp and DMSO on Vero E6 cells. Additionally, a reference sample containing 900 µL of the virus and 100 µL of DMEM (SARS-CoV-2) was prepared to confirm the virus titer used in the experiments.

The prepared samples (SARS-CoV-2 + Hyp light, SARS-CoV-2 + Hyp dark, and SARS-CoV-2) were inoculated into 96-well plates containing a pre-formed monolayer of Vero E6 cells (>85%) in a 10-fold serial dilution from −1 to −8. The control samples (Hyp and DMSO) were inoculated into 24-well plates with Vero E6 cells to evaluate the potential toxicity of Hyp and DMSO.

For the fixation of SARS-CoV-2 virions, the culture medium from the infected Vero E6 cells, inoculated as described earlier, was collected 72 hours post-infection. It was then clarified by centrifugation at 3200g for 20 minutes and fixed with 4% formaldehyde for 30 minutes at room temperature. The fixed virions were concentrated from the medium through ultracentrifugation using a 20% sucrose cushion for 120 minutes at 147,000g in a Beckman TY50.2 Ti rotor. The concentrated particles were then resuspended in PBS and stored in aliquots at −80 °C.

Rights of the images presented: All the Figures of this chapter were taken and adapted from [34].

2. Supported Lipid Bilayers

Biological membranes of eukaryotic cells are complex structures, very crowded environments that comprises phospholipids composing the lipid bilayer, cholesterol, transmembrane proteins like channels, receptors, etc.

Enveloped viruses also have a similar structure with a double layer and some important proteins for their replication and binding to the host cell, like the spike glycoprotein. This is composed of two functional subunits, S1 and S2 that are active in different phases of the viral infection, from the binding to the ACE-2 receptor in human cells, to the fusion of the envelope to the host cell membrane. The mechanical property of the envelope is also crucial for the two membranes to be fused together. It is widely established that Hyp affinity to phospholipidic envelope is in the order of a few nM, as we also found out in relation to the binding to SARS-CoV-2. We decided to use model systems like lipid bilayers without the concern of oversimplification. In fact, the specificity of the interaction depends on the chemical properties of Hyp, as already mentioned, having a highly hydrophobic core. On the other hand, the affinity of Hyp for hydrophobic cavities or clefts in proteins has been reported to be in the μM range. Therefore, it is reasonable to state that Hyp binding to membranes is not particularly affected by the presence of specific proteins.

As we already explained in the theoretical chapter of the thesis, solid supported lipid bilayers are artificial lipid bilayer membranes that represent a widely exploited model system, a very useful tool to study physio-chemical properties involving biological membranes.

We employed SLBs to investigate the influence of Hyp on viral phospholipidic membranes, akin to those found in the SARS-CoV-2 envelope. To emulate this membrane, we utilized a specific lipid composition characterized by phase separation between a liquid-disordered phase and a denser phase known as liquid-ordered or lipid rafts.

Enveloped viruses are not able to directly synthetize the lipids they use to compose their external membrane. Therefore, they need to rely on some host cell compartment lipids; in the case of SARS-CoV-2, similarly to other viruses of the same family, it was found that its envelope forms thanks to the lipids of the endoplasmic reticulum (ER) [51] For that reason, we chose a composition of lipids to be as close as possible to those of the ER, but not exactly identical. The purpose of that was to avoid instability in the structure, because notably very highly complex SLBs (more than 4 components) are more prone to be intrinsically unstable, and subjected to higher variability in different experiments.

Therefore, we intended to have a stable platform in order to have consistent results, using as parameters to evaluate the effects of Hyp only its concentration, the power of the light involved, the time of acquisition and application of the light, etc. , but nothing involving differences in the SLB composition.

By means of AFM in either the imaging and force spectroscopy configurations, by optical fluorescence microscopy, we characterized the effects of Hyp on the overall stability of the bilayer, on the mechanical properties.
Thanks to measurements of correlation between the two techniques, we were also able to add some information about the specificity of interaction involving Hyp.

2.1 AFM measurements of Lipid Bilayers

The impressive z-axis resolution that is given by AFM [89], along with the possibility of studying samples at physiological conditions, makes it the ideal experimental platform to study supported lipid bilayers[92] [93] [56]. These samples have, in fact, a very low thickness, ranging from 4 to 6 nm. The instrument can be therefore sensitive to the sub-nanometric variation in height [89] typical for these samples. Such features of the sample height differences are critical to detect because they are typically very informative on the features of the sample and can reveal some of the effects induced by the presence of an external ligand.

2.2 AFM imaging

At first, we wanted to have a general picture of the bilayer's characteristics at the lipid composition and concentrations we chose. We focused the attention on the morphological characteristics of the lipid rafts (if present), the relative height with reference to the more liquid phase, as well as the total height of the bilayer. The presence of the cholesterol in our bilayer should be responsible for a phase separation between two phases, L_o and L_d. We can be confident about our bilayer being composed of L_o / L_d phases, by checking the height difference, that should be of about 1 nm [94].
The image showed the presence of the lipid rafts with a height of ~1 nm over the liquid phase, so we could be quite sure that we were dealing with a bilayer composed certainly of L_o and L_d phases. Nevertheless, sometimes we also saw the coexistence of a third, thicker phase of circa 2 nm, (though typically in very small areas) consistent with a gel and denser phase, also called L_β . This is most likely due to the quite low concentration of cholesterol (Chol) that we used. Possibly, Chol is unequally distributed, therefore some unsaturated lipids keep staying in L_β at room temperature, and are not affected by the action of Chol that should favor the transition $L_\beta \rightarrow L_o$. Thus, we can say that our bilayer is made of mainly L_o and L_d phases, but the probability of having a minimal fraction of lipids in the L_β phase is non vanishing.
On a few occasions, and sometimes also in the very same sample (Figure 2.1) we also found bilayers having some defects, because of small variability in the sample preparation, regarding for example the temperature, the quality of the mica layer, etc.
This situation is not ideal because we would like to simulate an intact membrane. However, we didn't exclude those samples because Hyp could show a different behavior on a membrane with preexisting defects [95].

Hyp stock that we had was 1 mM in DMSO; there is evidence that it influences the structure and characteristics of lipid bilayer membranes [8]. Since we were interested only in studying the effects of Hyp we wanted to test what was happening adding a small volume of pure DMSO, consistent on the amount we would have used for a possible dilution of our Hyp stock.

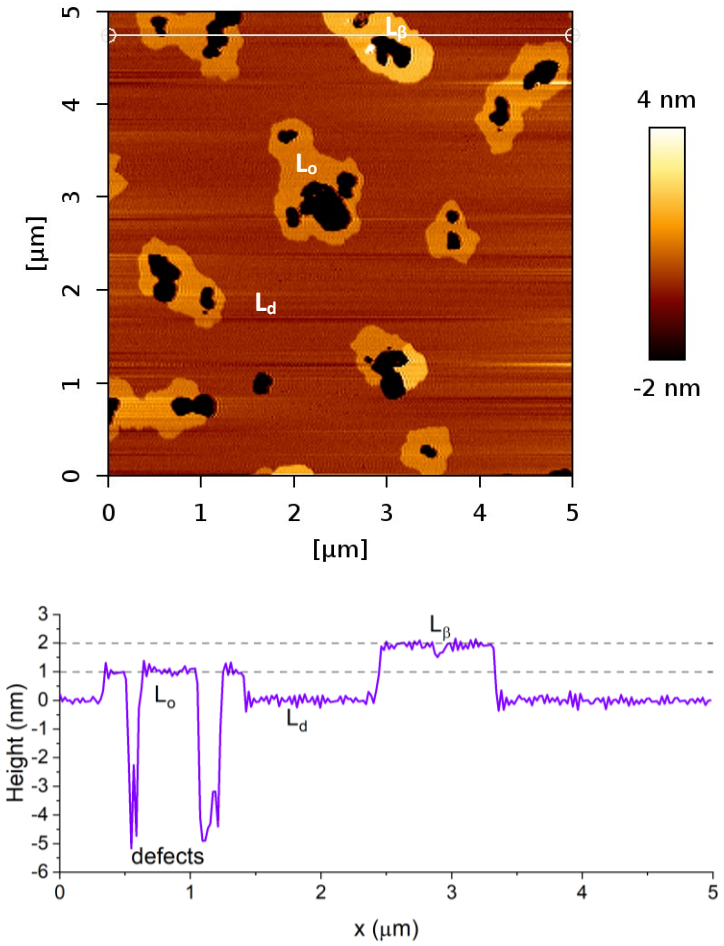

Figure *2.1: representative AFM image and line profile trace of our bilayer in presence of either defects (black regions), and of all the three phases L_d, L_o, L_β.*

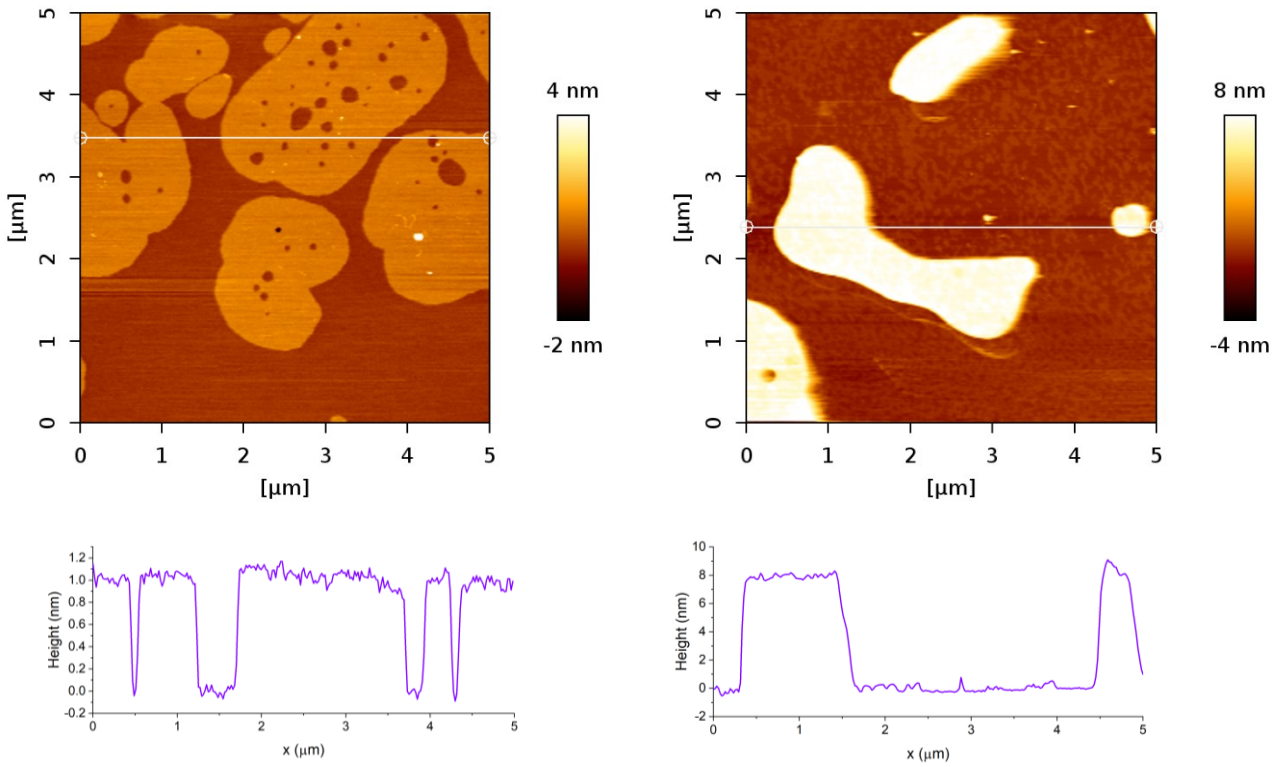

Figure *2.2: AFM images and line profiles of the same region of the sample. We can notice a complete rearrangement of the bilayer structure when 20 µL of pure DMSO are added (right) with respect to the clean bilayer (left).*

The Figure 2.2 clearly shows the complete rearrangement of the structure, no more consistent with the starting bilayer. These measurements clearly indicated that we could not add Hyp from a stock solution in DMSO, but we had to use a stock solution in water, even though Hyp is not very soluble and can form aggregates. This can create problems concerning the effective final concentration of Hyp on the sample; we will discuss this more in detail within the material and method section.

2.2.1 AFM imaging with Hyp+light

We started by analyzing the photodynamic effects of Hyp on the bilayer at different concentrations, by using a mercury arc lamp to excite the molecule and produce ROS. We weren't absolutely sure about what to expect with respect to the morphology of the bilayer, nonetheless, due to the disruptive effects of singlet oxygen, it is likely that Hypericin can cause irregularities on the bilayer, possibly nanoscopic holes [96] Before proceeding on the actual experiment we performed one control experiment to assess that light itself is not affecting somehow the morphology of the membrane.

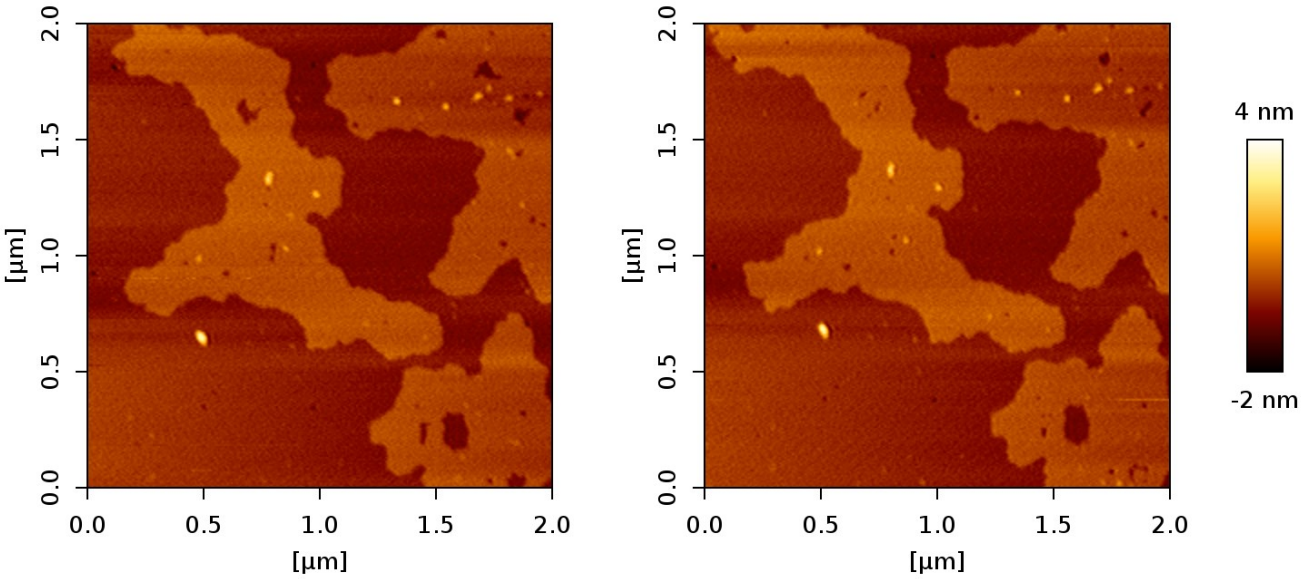

Figure *2.3: bilayer in dark condition (left) and with light irradiation, using a mercury arc lamp (right). No Hyp was added in either measurement.*

The control measurement is shown in Figure 2.3. We can clearly see that no appreciable effect is caused by the presence of the sole light. In fact, the two images are almost identical except for some discardable differences that are most likely due tiny movements of the bilayer.
In general, every time we were making AFM acquisition on the very same area of our bilayers and in the same conditions, some tiny differences showed up over time. They could involve the appearance (or disappearance) of tiny holes, as well as their change in shape, coalescence of lipid rafts and variation on their borders. All of these (slight) differences are proportional to the time of acquisition required for a standard AFM image (0.7-1 Hz, normally 256x256 px).
The lipids are free to move, either on the lipid rafts or in the more fluid phase; also, the bilayer is lying on a very tiny layer of water which can favor an overall drifting of the structure.
The image in light was made after 5 min of continuous irradiation, therefore there was some time for the lipids to move and for the bilayer to slowly rearrange.

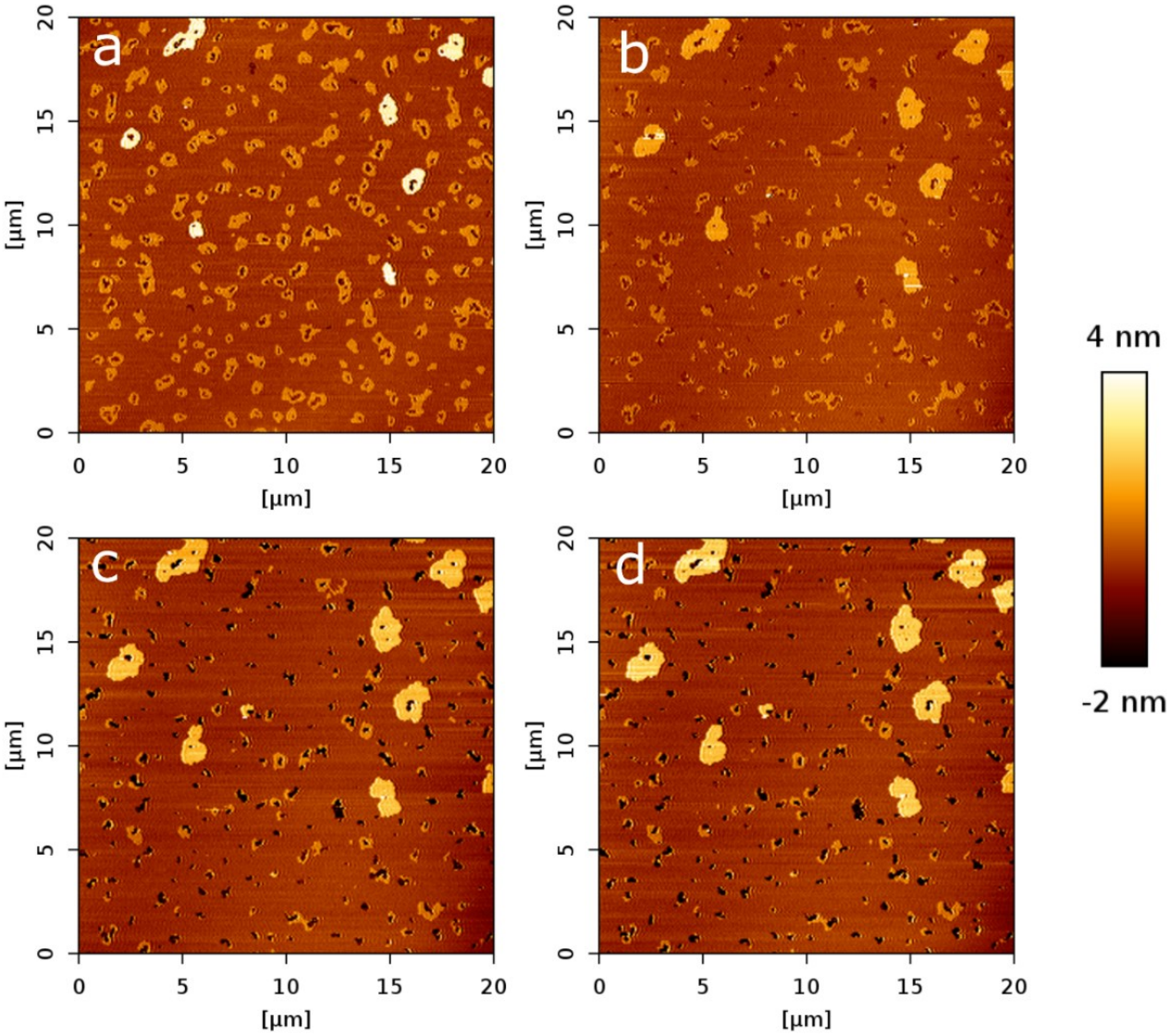

Figure *2.4: images of the bilayer at the same ROI. The images were acquired while irradiating at 0 nM (a), 25 nM (b), 50 nM (c) and 100 nM (d).*

The image in Figure 2.4 represent the bilayer at different concentrations of Hyp. We can see that the bilayer without Hyp already exhibits the three phases, as well as some defects. By adding Hyp there is an extensive effect on the imaged area, particularly on the amount of lipids in the L_o phase. Also, the number and the size of the defects are increasing, in line with the photodynamic effect induced by the molecule.

Similarly, the lipid rafts in the gel phase are also getting bigger, possibly indicating that a redistribution of the local concentration of cholesterol could be triggered by Hyp.

Moreover, in many L_β lipid rafts we found a behavior like the one shown in Figure 2.5, that is many tiny holes appearing as soon as the concentration of Hyp increased.

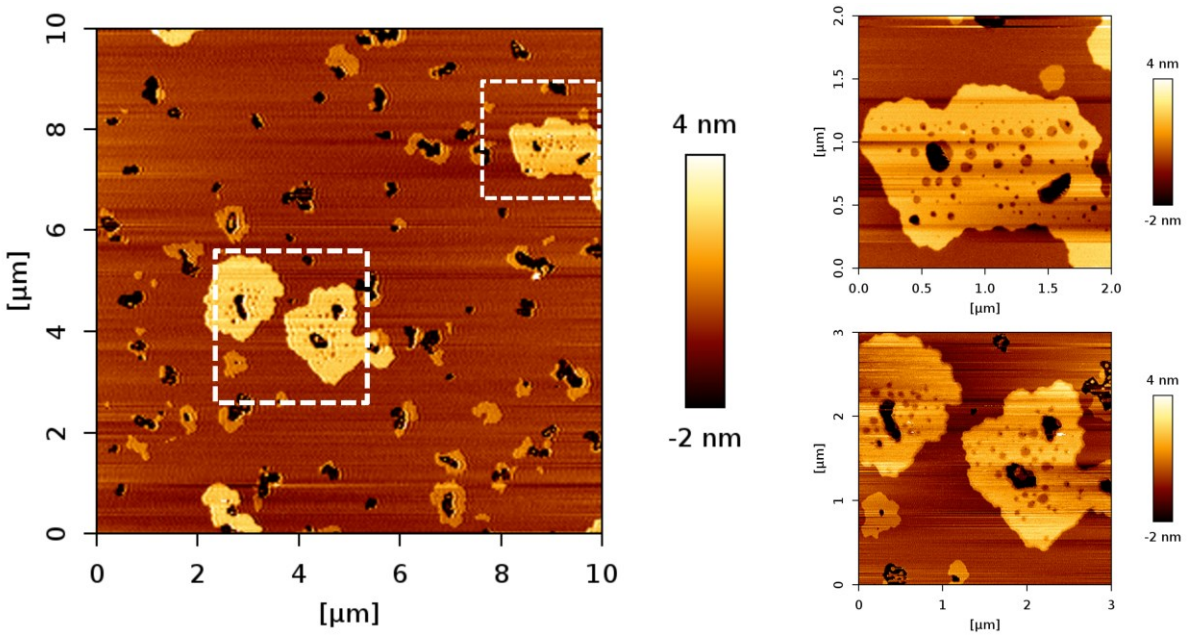

Figure *2.5: the effect on the gel phase at 100 nM concentration is visualized here. The inset images b) and c) clearly show the nanoscopic holes on the surface of the L_β rafts. We can appreciate that they possess a peculiar shape, almost round. Those irregularity areas in this phase were never detected in measurement without Hyp+light.*

2.2.2 AFM imaging with Hyp in the dark

Because we were aiming to study if Hyp affects the membrane even in absence of light, we performed some set of experiments with the very same conditions as those employed in the measurements shown in Figure 2.4 and Figure 2.5; the only difference was that we didn't employ any light irradiation.

We are not able to appreciate any relevant difference in the morphology and the general arrangement of the bilayer as shown in Figure 2.6: we can't see either any holes appearing in the image, or redistribution of the bilayer phases. In fact, we can only appreciate two phases involved, L_d and L_o in all the 4 images with substantially the same occupancy ratio on the area of the image.

There are some differences in the shape of the lipid rafts in the 4 images, but they are most likely due to the regular diffusion of lipids and to the drift of the bilayer.

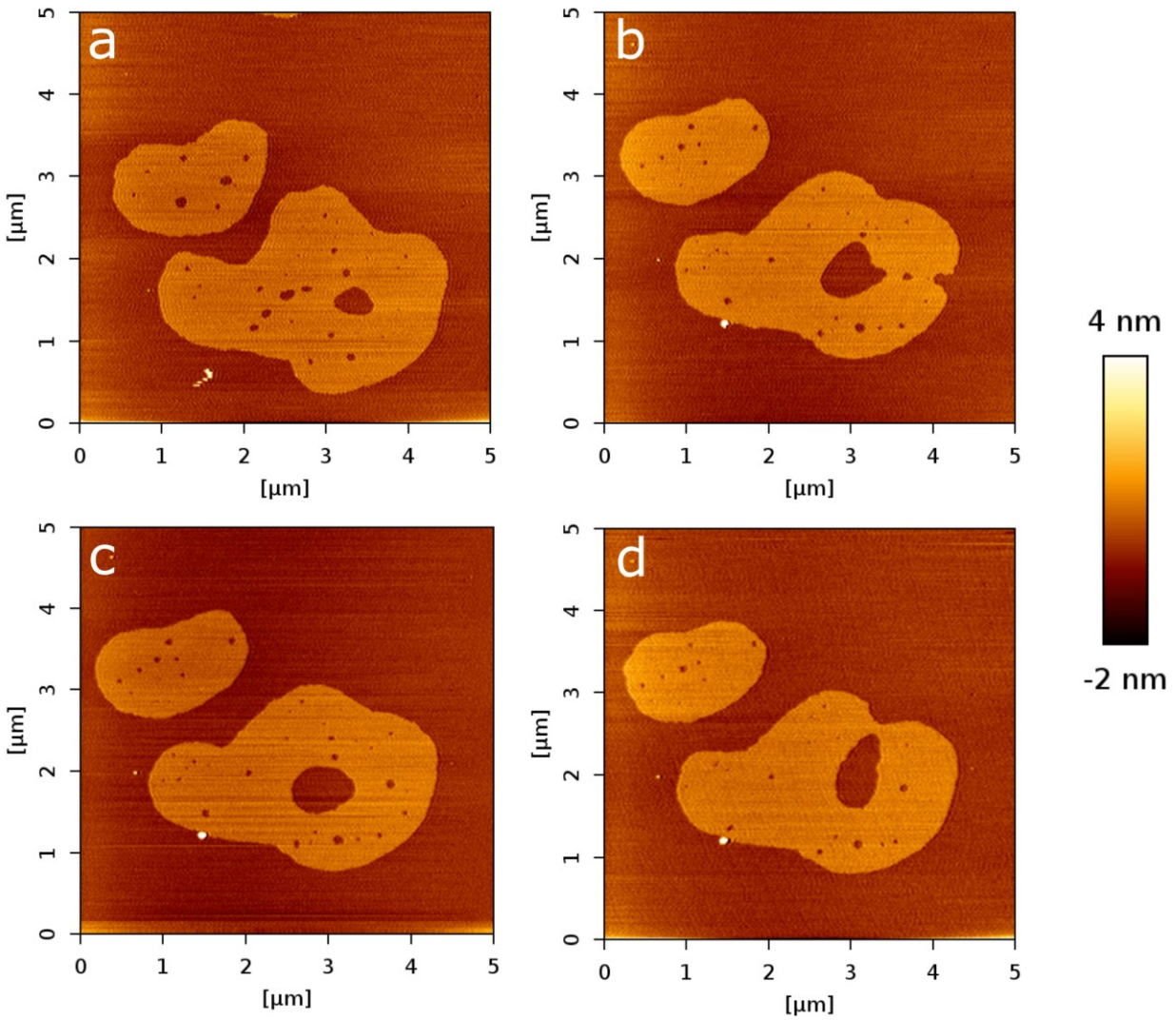

Figure *2.6: images of the bilayer at the same ROI. The images were acquired without light irradiation at 0 nM (a), 25 nM (b), 50 nM (c) and 100 nM (d).*

At first glance, this result could suggest that the morphological effects induced by the PS in the dark are negligible. However, it is rational to expect that imaging techniques may not be sensitive enough to detect subtle differences between light and dark conditions.

In fact, if an effect in the dark is produced, it is most probably linked to the mechanical properties of the membrane, as it should be for viral particles.

One of AFM advantages among others, is that it offers the possibility of obtaining spectroscopic information; by measuring the forces as the tip approaches and retracts from the surface we can have access to the nano-mechanical properties of a sample, such as stiffness, adhesion, and elasticity.

2.3 AFM mechanical properties

2.3.1 Measurements of the Young Modulus

Since we were mainly interested in the variation of stiffness that could be induced by Hyp, we obtained values of the Young Modulus (E), also called the elastic modulus, for the model membrane. E can be regarded as a measure of the stiffness of a material: a high Young modulus means high stiffness, i.e. low deformation under load. Conversely, a material with a low Young modulus is more flexible or elastic. Operatively, it is defined as the ratio of stress (force per unit of area) to strain (change of length per unit of length) in a material under tension or compression:

$$E = \frac{\sigma}{\varepsilon} \tag{15}$$

Where σ is the stress, and ε is strain [97], the Young Modulus is dimensionally expressed in units of pressure, specifically Pascal (Pa) or $(\mathrm{N/m^2})$.
To extract the values of E from AFM we performed nanoindentation measurements from which we obtained Force-Distance (F-D) curves. Nanoindentation means that a very small and pointed indenter (our tip) is pressed into the surface of a material to measure its mechanical properties. We chose to fit our curves using the Hertz-Sneddon model [98] [99][100].
This is a very common model for this kind of applications [101], and is based on a certain set of assumption and approximations. These include [102]:

1. The deformation occurs within the elastic regime, meaning that the material will return to its original shape after the removal of the force.
2. The magnitude of the deformation is small compared to the radius of the contact area where the force is applied.
3. The applied force is perpendicular to the surface, indicating the absence of any shear forces in the interaction.
4. The sample is considered to be semi-infinite, implying that its depth is significantly larger than the extent of the deformation or contact area.

The pressure applied by the tip is dependent on its shape, therefore its characteristics is included in the model. In our case the tip can be considered a circular paraboloid, which is unambiguously dependent on only one geometrical parameter, which is its radius, R. The formula of the force can be expressed as follow:

$$F = \frac{4}{3}\frac{E\sqrt{\delta^3 R}}{(1-\nu^2)} \tag{16}$$

Where E is the Young Modulus, R is the radius of the tip, δ is the indentation and ν is the Poisson ratio. This value is defined as the ratio between transverse strain and longitudinal strain. Typically for slightly compressible materials like liquids and rubbers, where stress predominantly leads to changes in shape, the Poisson's ratio approaches 0.5 [103][97].
The value for the Poisson ratio that we will then consider from now on is 0.5, therefore we can rewrite Equation (17) as:

$$F = \frac{16}{9} E \sqrt{\delta^3 R} \tag{17}$$

The assumptions introduced in the Hertz-Sneddon model might result in notable inaccuracies in the calculation of Young modulus. Anyway, our interest doesn't lie in finding the absolute value of the Young moduli, but rather on the distinction between the case with and without Hyp.
Notably, employing solid supports has many advantages, for example they primarily contribute to the increased robustness and longevity of the phospholipid bilayer membrane. However, a significant limitation is that the supported membrane does not exist in complete separation from the substrate beneath it [6].
Therefore, among all of the assumptions, the number 4 is the one that could affect adversely even comparative measurements. In fact, the lipid phases involved possess different heights, making it necessary to introduce a correction that accounts for the thickness of the sample, thus for its vicinity to the solid substrate.
The solution to exclude the also called "bottom effect artifact" [104] has been extensively discussed [105] [106] and it was recently proposed a model that completely corrects it [107]. For the same tip geometry, it yields the following force–indentation expression:

$$F_G = F_0 \left(\frac{1}{h^0} + \frac{1.133\sqrt{\delta R}}{h^1} + \frac{1.497\delta R}{h^2} + \frac{1.469\delta R\sqrt{\delta R}}{h^3} + \frac{0.755(\delta R)^2}{h^4} \right) \tag{18}$$

Where h is the height of the sample and F_0 is the force expressed in the Equation (17).
By using this formula for each force curve, we were able to reconstruct the corrected value of the Young moduli.

In order to obtain the most accurate possible value for h, we performed some measurements with partially intact bilayer. If the defects in the bilayer are not wide enough, there is no certainty that the tip is effectively touching the solid substrate underneath. What we did to ensure the presence of sufficiently wide holes, was to generate them by ourselves, by rinsing the bilayers very strongly after the measurements. We acquired 5 images with plenty of holes for each field of view, for which we had a height distribution. The distance between the peaks gave us the values for the height of the phases.

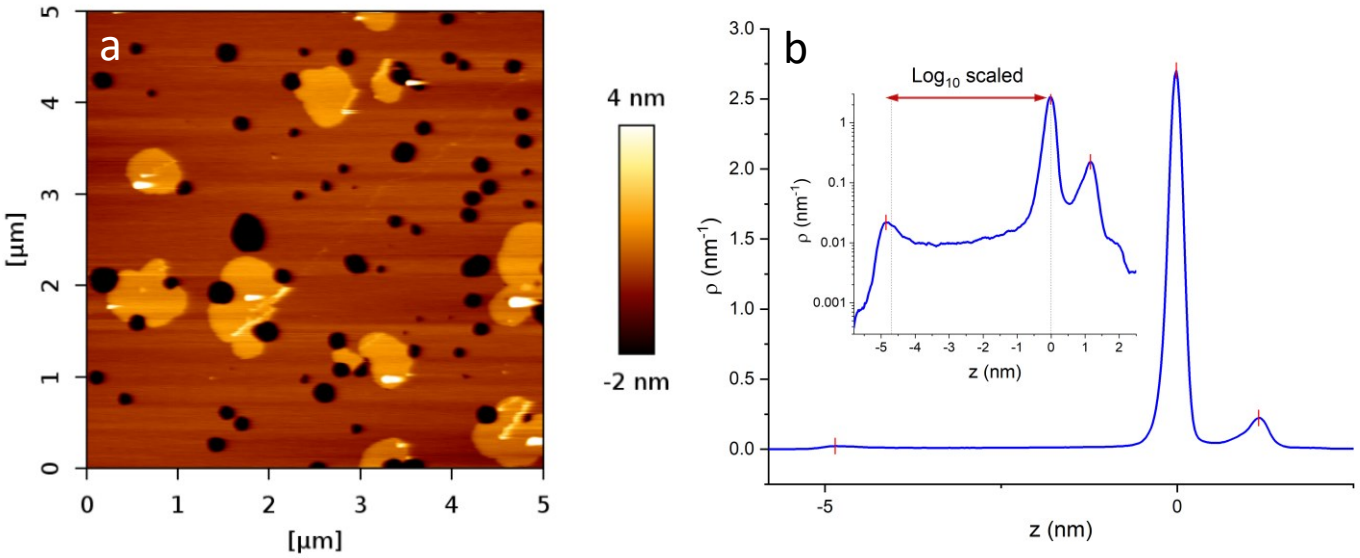

	Height (nm)
L_d	4.84 ± 0.06
L_o	6.02 ± 0.06

Figure *2.7: a) representative image of topography of the sample we exploited to quantify the height of the bilayer. The holes are clearly visible, and they were obtained by strongly rinsing the sample with ultrapure water. The image is 512 px x 512 px. b) Height distribution obtained from one of the images we analyzed. We can distinguish three peaks whose values were obtained by means of a "peak fit". They are better visualized on the inset on the top right, where the y-axes is log-scaled. The distance between the peaks defines the height of L_d and L_o. In particular, the table is showing the mean values obtained by means of the 5 images mentioned above.*

We performed Quantitative Imaging (QI) [108] measurements in order to extract mechanical properties from the sample directly from the images. QI allows to record F-D curves at each pixel of the image, giving information about the local interaction between the tip and the sample. Therefore, for all the measurements we obtained 16,384 force curves (128x128 pixels), enough to have a relevant statistic about the mechanical properties of the sample.
Operatively, we fitted the F-D curve using the model of Equation (18) on the very first nm after the contact of the tip to the sample; we will deepen the description of the analysis on the material and method section.
In order to be as accurate as possible, we acquired QI images of a phase per time, using small fields of view of 500 nm – 1 µm. For each sample, we analyzed separately the phases involved, especially the L_o and L_d phases. In fact, typically areas with lipids in the L_β phase where not always present and, if so, their size were insufficient to select a ROI and discriminate from the adjacent phases.
For each sample we differentiate the cases of: No Hyp, Hyp in dark, Hyp with light.
We used a much higher concentration of Hyp with respect to those described in 2.2 for this kind of measurements. The reasons for that were dependent on the system that we used for the QI: the microscope was equipped with a weaker lamp, and therefore the concentration of Hyp was raised to a reasonably high value, in order to balance the loss in photodynamic effects induced by the low light power. Moreover, we believed that whether Hyp was producing an effect on the rigidity in dark, this should have been practically undetectable in a bilayer at the concentrations used in the 2.2 paragraph. Actually, we showed that for a single viral particle, because of its dimension and geometry, only 30-40 molecules of Hyp could be accommodated.
It is reasonable to expect that the effect on the stiffness happens when saturation condition is reached. This means that a higher concentration is needed for a much more extended system such as a lipid bilayer.

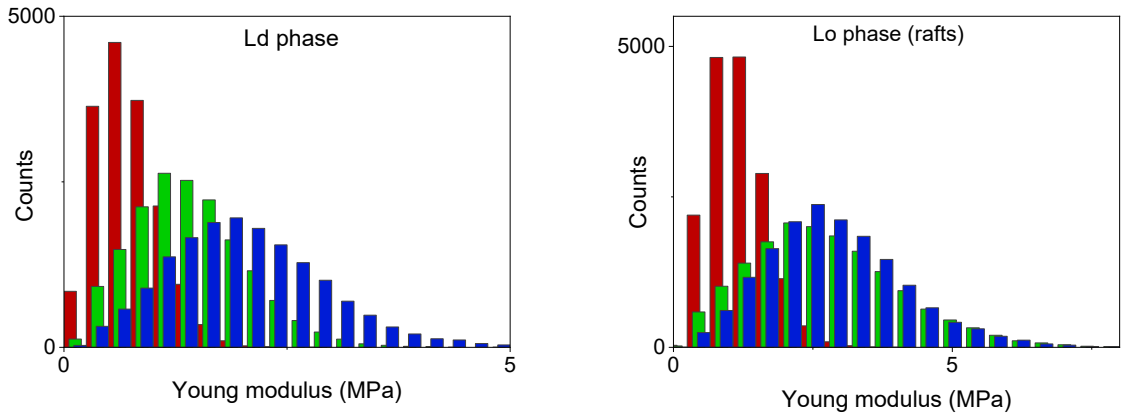

Figure *2.8: histograms of the distribution of the Young moduli corrected for the height of the bilayer in the three different conditions, i.e. without Hyp (red), with 1 µM of Hyp in dark (green), with 1 µM Hyp during irradiation (blue). We separated the two phases in two different graphs, the liquid ordered phase on the left, the ordered phase on the right.*

Hyp]	*E of L_d phase (MPa)*	*E of L_o phase (MPa) - rafts*
0 µM	0.68 ± 0.11	1.13 ± 0.03
1 µM in dark	1.31 ± 0.14	2.49 ± 0.08
1 µM in light	1.89 ± 0.16	2.66 ± 0.05

Table 2: the table outlines the values of the Young moduli (E) extracted by fitting the distributions with a gaussian function.

The results of the measurements are summarized in Figure 2.8 and in Table 2: the table outlines the values of the Young moduli (E) extracted by fitting the distributions with a gaussian function. Apparently, there is a trend indicating the stiffening action of Hyp on the bilayer, both in the dark and during light irradiation. This is in accordance with the previously discussed hypothesis.
Also, the differences in the L_d and L_o phases are significant, indicating that the L_o phase has a more pronounced stiffness.
The QI measurements from which we obtain these results are not trivial to be performed. Even though the number of force curves acquired should be good enough to have a relevant statistic, the measurements could be affected by some systematic errors.
The chosen parameters can be critical for a proper outcome, also, the dirtiness that the tip can collect during imaging can affect the real stiffness. This issue is also both tricky to quantify and to prevent. In fact, there is no way to completely discard this issue, because of how the measurements are carried out: we analyzed with the same parameters and the same tip before and after addition of Hyp.
The increase of the Young modulus induced by Hyp is considerable, but we can't completely discard the possibility that it has also been affected by dirtiness on the cantilever.
In order to have more evidence about the effects of the PS, we decided to employ another AFM methodology to assess the mechanical properties of the bilayer.

2.3.2 AFM mechanical properties: breakthrough measurements

Besides accessing the information about the elastic modulus, an essential approach to comprehending the stiffness of a bilayer is to study its breakthrough properties. When acquiring force curves there can be a noticeable jump of the AFM tip through the film, which occurs when it surpasses a specific threshold force, that we will call breakthrough force (F_b) [109][110].
This value represents the maximum force that a membrane can endure before being penetrated by the sharp tip; it is a key metric for assessing the mechanical stability of the SLB in question, and it's a parameter closely associated with the arrangement and organization of lipids within the membrane [93].
F_b can be directly determined by the force curves. A rupture event results in a noticeable discontinuity in the force-distance graph, indicating a local breakdown of the bilayer and the

penetration of the tip into the SLB. Following this event, the tip presses against a solid substrate, maintaining a steady distance from the sample [111].
Another informative metric that can be extracted by the breakthrough discontinuity in the force curves is the distance the tip travels during bilayer penetration, which we name the breakthrough length (L_b). Assuming that the tip contacts the underlying substrate post-bilayer rupture, L_b indicates the thickness of the SLB at its point of maximum deformation.
Moreover, like for any other kind of force curve, the indentation (I) can be extracted. Based on what we discussed about L_b , we can say that : $I + L_b = \text{total bilayer thickness}$.

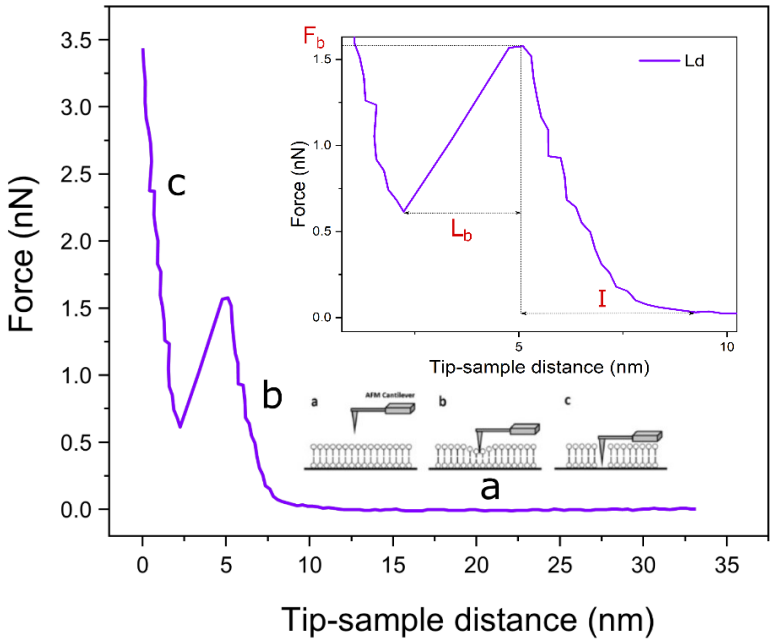

Figure *2.9: representative image of a F-D curve with a rupture event, and relative schematic picture. a) Part of the curve where the tip is approaching the sample; b) indentation of the tip onto the bilayer; c) the tip is now touching the substrate; hence the slope is practically vertical. Zoomed inset of the F-D curve, highlighting the discontinuity region. The parameters I, F_b, L_b are directly extracted from the spectra.*

In this case the F-D curves to extract the breaktrough parameters were obtained by using a different experimental apparatus and AFM modality; as a matter of fact we didn't apply QI approach, but a rather similar mode called Jumping mode (JM), also called pulse force mode [112] [113] JM is used for imaging biomolecules under physiological conditions, and it is particularly advantageous when imaging samples that are weakly bonded to the substrate. It has been effectively applied to a variety of biological systems such as DNA [114], Alzheimer paired helical filaments and different kinds of viruses [115][116][117], membrane, demonstrating its versatility and effectiveness in various contexts [118] In fact, in this modality lateral and normal forces are minimized, making it preferable over other modes for certain samples. The rationale behind choosing this particular method will be further elucidated, but primarily it relates to our

intention to utilize AFM on SARS-CoV-2 virus particles. We will discuss in more detail in the course of this thesis.

In any case, the sample preparation, the tips as well as the solid substrate were exactly the same as those already used, therefore it is reasonable to expect a comparable behavior of the bilayer, not being dependent on the microscope.

The illumination in this case was coming from the top by means of an external halogen lamp, and a FITC excitation filter.

Similarly to the Figure 2.8, we show in Figure 2.10 the distributions obtained for the two phases L_d and L_o for the usual three conditions. The physical quantity we were interested in, to evaluate the mechanichal resistance to the penetration of the tip, was the breakthrough force. The concentration of Hyp was the same used for the measurements of the Young modulus.

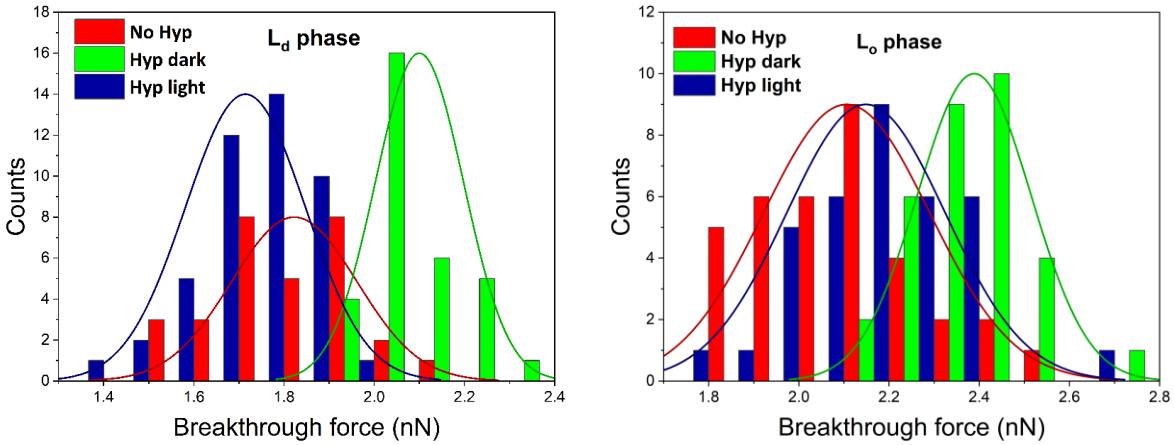

Figure *2.10: distributions of breakthrough force values of the bilayer for the two phases L_d and L_o. As in* Figure *2.8, red bars represent the case without Hyp, the green 1 µM of Hyp in dark, the blue 1 µM Hyp during irradiation.*

Hyp]	*F_b of L_d phase (nN)*	*F_b of L_o phase (nN) - rafts*
0 µM	1.82 ± 0.14	2.11 ± 0.18
1 µM in dark	2.10 ± 0.09	2.39 ± 0.13
1 µM in light	1.71 ± 0.13	2.15 ± 0.17

Table 3: the values of breakthrough forces extracted from a Gaussian fit are reported.

The findings indicate that the L_o phase exhibits greater stiffness compared to the L_d phase. In this occurrence, adjusting for the sample's height was unnecessary, as the point of sample breakage is independent from the substrate. Both phases exhibit a noticeable stiffening effect due to the presence of Hyp, with a significant contrast observed between the values without Hyp and those with Hyp in darkness. The presence of Hyp results in an approximate 13%-15% increase in the F_b value for both phases. Notably, under illumination, this value shifts back, seemingly contradicting the measurements of the Young Moduli.

However, the two measurement could reflect distinct mechanical properties of the membrane. Indeed, Young modulus is primarily concerned with elastic deformation, where the material returns to its original shape after the removal of stress. Brekthrough force, however, is often associated with plastic deformation or fracture, where the material undergoes permanent deformation or failure. Therefore, the Young modulus provides an indication of a material's resistance to elastic deformation, while the breakthrough force is mainly correlated to plastic properties.
In summary, while a relationship exist between Young modulus and breakthrough force (stiffer, higher Young modulus, materials generally require greater force to deform or break), the exact force required for breakthrough may depend on a combination of several material properties and the specific conditions of force application.
The influence of Hyp on the mechanical properties of our model membrane may not have a straightforward interpretation.

2.4 High speed AFM imaging

Conventional AFM imaging is known for being time-consuming in its imaging process, allowing for speed that are typically in the range of 0.5-2 lines/s; which means that an optimal imaging result requires several minutes. Specifically, in the context of capturing more insights of the dynamic behaviors of the effects of Hyp on our biological sample, conventional AFM temporal resolution is not sufficient.
For that reason, we performed high speed AFM imaging in tapping mode using a microscope capable of collecting lines at a speed up to 200 Hz, depending on the dimensions of the field of view.

2.4.1 AFM imaging with Hyp+light

In contrast to conventional AFM analysis, where multiple Hyp concentrations were used, to study the temporal dynamics of the activity of Hyp we employed only one concentration for each set of measurements.
Similarly to the previous experiments, we kept the light on during the measurement, using a wide-field illumination coupled with a similar 10x objective lens. However, instead of a mercury arc lamp used in 2.2.1, we utilized a 488 nm diode laser or, alternatively, a 470/20 nm LED for illumination.
The setup's complexity was increased by the arrangement of the high-speed AFM head and the sample placement beneath it. This condition made it more challenging to precisely add the solution with Hyp, leading to reduced control over the exact area of liquid injection. Consequently, there was a non-negligible chance that Hyp solution misplaces or to leaks into areas other than the intended sample surface.

Due to these operative factors, we decided to use a slightly higher concentration of the solution than what was described in paragraph 2.2.1.
The first experiment that I will show has been performed by imaging 5 different ROIs. Figure 2.11 is representing one of these (the other 4 are not shown), without the application of Hyp and/or light. The images were acquired at 20 lines/s, 10 x 10 µm, 1024 x 1024 px, therefore each acquisition lasted about 50 seconds. Besides the improvement in temporal resolution, we even have much better spatially resolved images.

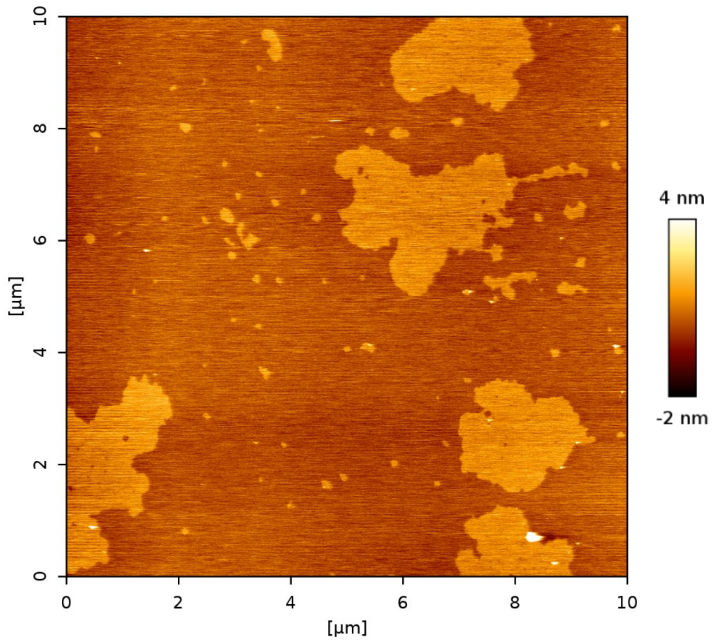

Figure *2.11: image of a region of the bilayer acquired with high-speed AFM.*

Two notable observations from Figure 2.11 were the absence of any detectable defect in the bilayer, and the involvement of only two lipid phases, L_d and L_o, without the presence of L_β. This scenario represents the "simplest" situation with our lipids mixture, as we discussed previously, contrasting with the results we obtained through the standard AFM imaging, which showed preexisting defects and all the three phases present. Being able to extract some results on a defect-free membrane like this one would give even more insights on the photoactivity of Hyp on membranes. Indeed, it is intriguing to determine whether the PS can induce an effect, especially in the formation of nanoholes, within a completely intact membrane. The utilization of high-speed imaging is particularly relevant for this purpose, as it enables the detection of small holes, which may be opening and closing reversibly.

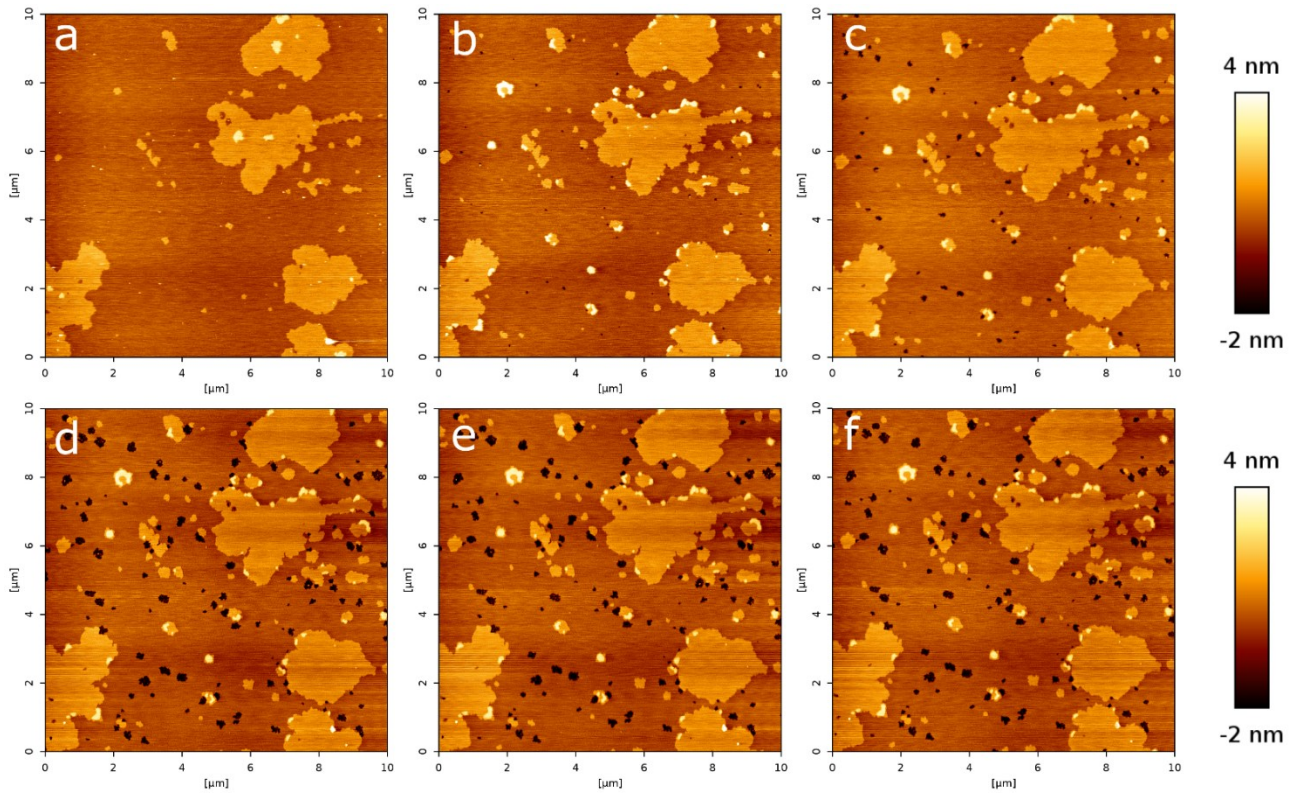

Figure *2.12: image of the bilayer with fixed concentration of Hyp during light irradiation. a) 1 min of light irradiation, b) 35 minutes, c) 70 minutes, d) 110 minutes, e) 125 minutes. f) was acquired after keeping the light off for 20 minutes to check if the holes were reversible to some extent. For the same ROI imaged at t=0 refer to* Figure *2.11.*

From Figure 2.12 we can qualitatively already notice two distinct dynamics involving the photoactivity of Hypericin. After only one minute of irradiation, we can already see something happening, concerning the appearance of the denser phase L_β. At first this phase is forming in correspondence of the middle of the lipid rafts, but after some minutes it "moves" in proximity of their edges.

The second dynamics is relative to the formation of tiny holes in the bilayer, mostly in the L_d phase, which is consistent with the fact that this phase is rich in unsaturated phospholipids, which are most likely to be affected by the action of O_2.

Differently from the third phase, these defects in the bilayer are forming at a much slower rate. The two dynamics should reflect a multimodal physical-chemical action of Hypericin on the sample.

In Figure 2.13 we sum up the results of this measurement, considering all the 5 ROIs analyzed. We performed some image analysis to check the time-dependent trend of the dimensions of the L_β denser phase and the holes, both induced by the combined action of Hyp and light.

The graph in Figure 2.13 is very explicative of the different dynamics involved.

Regarding the area of the patches in the denser phase, we can appreciate a fast growth in the very first minutes, while the dimensions reach a saturation value quite rapidly; we need a better sampling to acknowledge this fast effect.

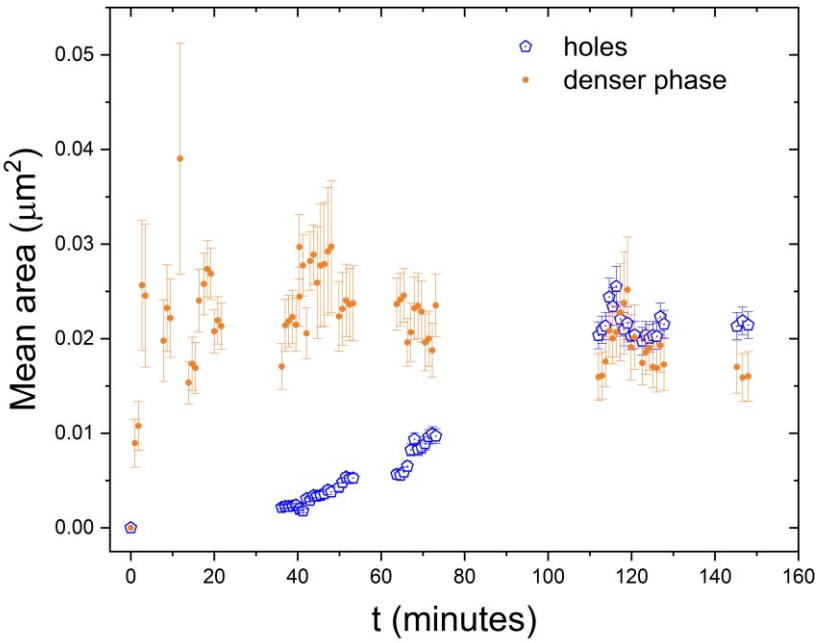

Figure *2.13: time evolution of the sample represented by the dimension of holes (blue) and the Lβ phase. t = 0 → **laser on**, t = 150 min → **laser off***

Conversely, hole formation occurred after more than 30 minutes of light exposure, indicating a slower process compared to the earlier one. The time interval preceding the defect formation should not be regarded as a fixed value. We previously mentioned the challenge in accurately determining the Hyp concentration in the bilayer for this particular measurement. Additionally, even if precise concentration estimation were feasible, the wavelength of the employed laser, while sufficient to excite the molecule, does not do so with optimal efficiency.
Presumably, the holes start to form when the concentration of ROS reaches a level capable of overcoming a certain energy barrier required to remove lipids from the bilayer.
Over time, both dynamics stabilize at saturation levels. Intriguingly, the saturation value for the creation of the third phase occurs a few minutes prior to the emergence of holes.
This observation further supports the notion that these two dynamics are separate processes. However, their continuous nature implies a potential correlation between the two phenomena. In any case, we will discuss the details of the two events separately.

Formation of pores in the bilayer

As we observed, even in defects free membranes, the combined effect of light + Hyp in creating and enlarging pores is present.

The first comment to make related to this is the shape of such defects, that is not spherical, particularly for the bigger ones, as it can be appreciated in Figure 2.14. Recent papers have investigated pore appearance in lipid bilayers with very similar shapes resembling fractal-like (see 2.4.2) patterns; this feature reflects the particular way they are formed, that shouldn't be influenced by the interactions between the membrane and the substrate or the substrate and Hypericin [119] [95]. The damage pattern is in fact suggesting a mechanism of lipid extraction that is progressing at the edges of the defects; in this region there should be more accessibility to the lipids, and it should be energetically more favorable to extract a lipid no more highly packed.

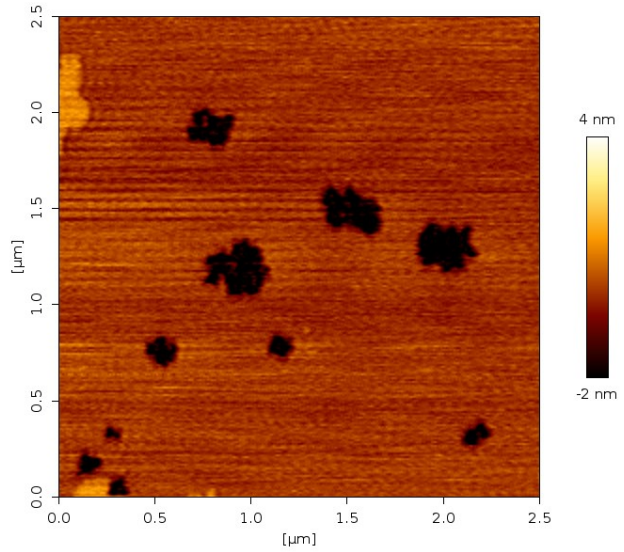

Figure *2.14: zoom of* Figure *2.12a highlighting pores in the bilayer. The irregular patterns are clearly noticeable, resembling a fractal-like object. Image size 256 x 256 px, pixel size ~10 nm.*

Since the defects are very tiny, they are not well enough spatially resolved to quantify the values of their fractal dimensions; however, it was possible to carry out a slightly different image analysis, investigating the "roundness" as a feature. This is defined as:

$$roundness = \frac{4\pi \cdot Area}{(Perimeter)^2} \tag{19}$$

Which is a value comprised in the interval [0,1], where 0 is a highly non-circular shape, and 1 is a perfect circle.

Moreover, we took the roundness of the defects of the bilayer in Figure 2.7a as a reference measurement. The process of formation of holes in this case was independent on the photodynamic action of Hyp, since the holes were "artificially" made by a strong rinsing.
They formed by mechanical stress induced by the water, which is a completely different process with respect to the Hypothetic single-lipid extraction induced by Hyp and ROS; as a result, we should expect a different value of roundness.

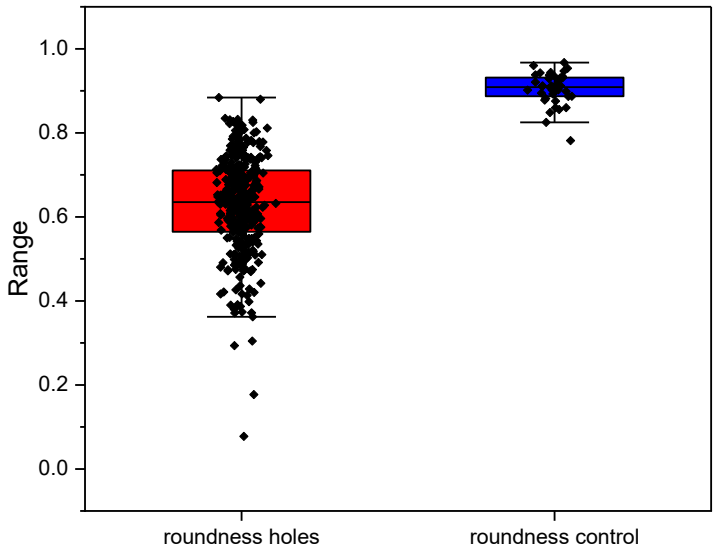

Figure *2.15: box plots representing the roundness of pores created by the photodynamic action of Hyp (red) and the control (blue) obtained by the images after the strong rinsing, in* Figure *2.7.*

In the chart (Figure 20), the dataset represented by the red box exhibits considerable variability, which is evidenced by the wide spread of data points and the vertical extent of the red box. This could be attributed to varying pore sizes affecting their roundness, with smaller pores tending towards greater circularity. The central tendency of this dataset is indicated by a median value of approximately 0.6, suggesting that the shapes are relatively less round, which aligns with our qualitative observations.
Conversely, the control dataset, as anticipated, presents less variation with data points more closely grouped around a median value that is near 0.9. This indicates that the pores in this group are nearly round, despite being a population dimensionally very diverse.
The second observation about these pores is about their peculiar deepness.
With reference to the measurements we performed to uncover the height of the bilayer (2.3.1), we obtained the value of ~5-6 nm, for respectively the L_d and L_o phase. Additionally, from the plot profiles in the bilayers with defects depicted in the 2.2 paragraph, the same height can be appreciated.

Meanwhile, in this experiment the depth disclosed is much less than the expected one, as depicted in the height distribution of Figure 2.16.
A gaussian distribution centered around 2 nm depth (with reference to the L_d phase) is found from the images.

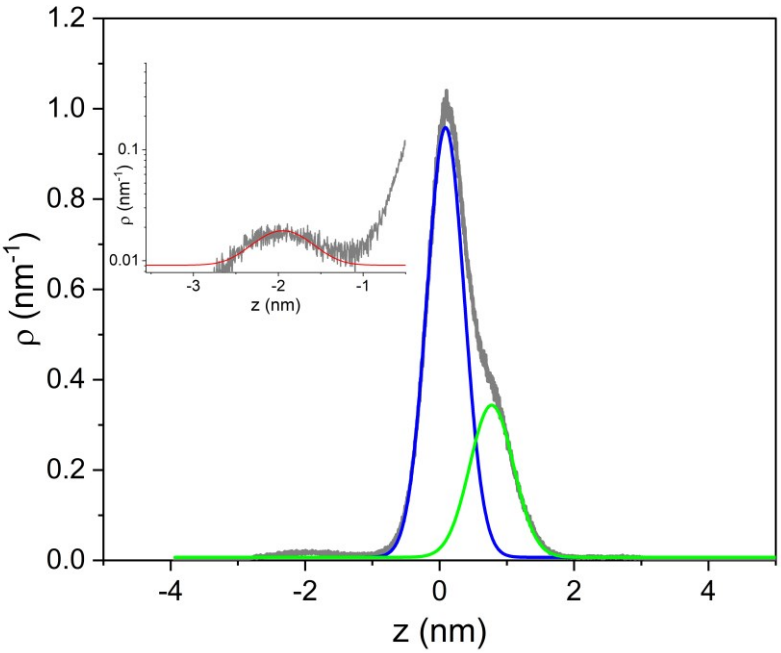

Figure *2.16: distribution of heights of* Figure *2.12f with Gaussian fits in blue and green representing the L_d and L_o phases of lipids, respectively. An inset within the graph shows the distribution of pore depth, with its fit illustrated in red.*

Apparently, this value is consistent with the thickness of a monolayer removed, which anyway yields to a difficult interpretation based on the structure of the bilayer. The small layer of water present over the mica substrate (0.5-1 nm thick) and the volume of water over the membrane, makes the bilayer very stable, exposing the hydrophilic heads on the opposite sides of the structure. The removal of one layer is instead exposing the hydrophobic tails to the water , which could cause instability to the structure.
Theoretical and experimental studies have predicted that rupture in phospholipid bilayers begins with the formation of a pore filled with water molecules [120], and this could be our case.
Our hypothesis is that the stabilization of the pore structure could be strangely given by Hypericin itself, which is possibly packing in correspondence of the water layer above the hydrophobic tails. This effect could be favored by the higher concentration of Hypericin that we used in these experiments with high-speed AFM.

Formation of the denser L_β phase

Due to the insufficient sampling in the initial stage of the first experiment, a second experiment was performed to describe better the dynamics of the formation of the third, more elevated phase.

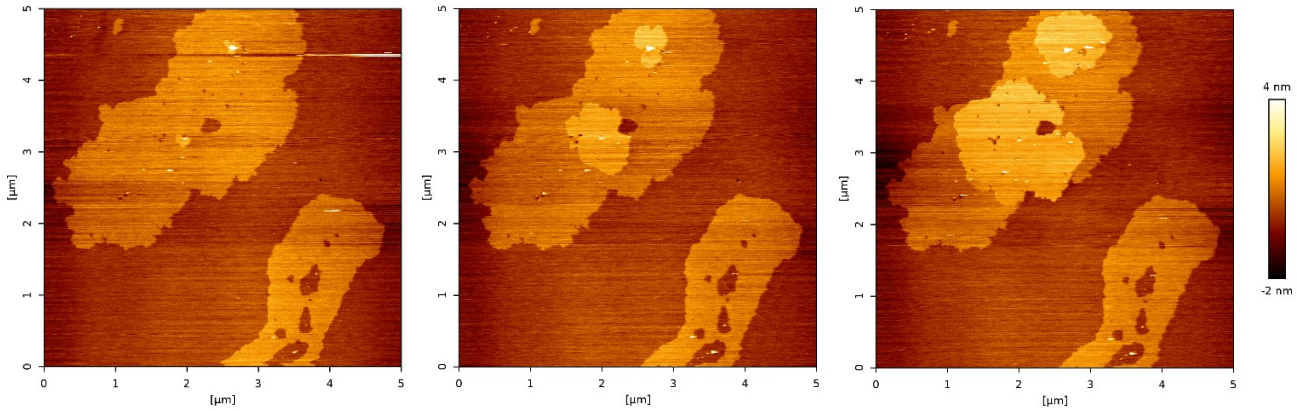

Figure *2.17: images of the Hyp-loaded bilayer during light irradiation at temporal intervals of 50 seconds. We can notice the increase of area in the L_β. The acquisition parameters here were 1024 x 1024 px, 20 lines/s, 5 x 5 µm.*

The images were collected with a smaller field of view, to allow faster imaging and to limit possible artifacts derived from the scanning at high rates.

The experiment was not trivial to perform, because we first had to find a region where an event of third phase formation where beginning, as shown in Figure 2.17, and be fast to switch to a smaller region that was allowing a faster acquisition without losing spatial resolution. In particular, the acquisition parameters of the subsequent images were 512 x 512 px, 50 lines/s, 3 x 3 µm, allowing a time of 10 seconds for each acquisition. A representative image acquired in these conditions is shown in Figure 2.18.

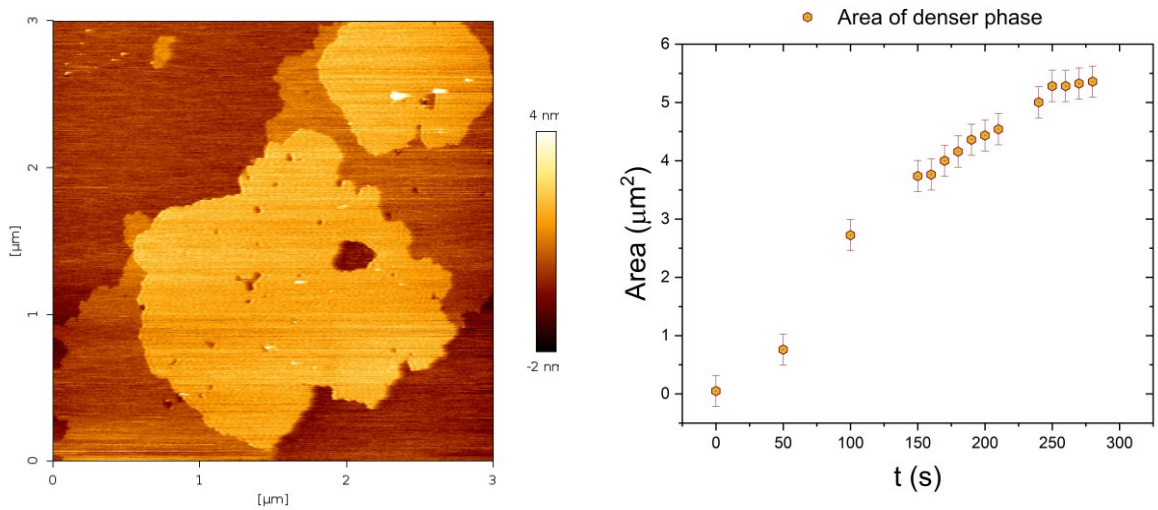

Figure *2.18: left) one of the 15 images of the bilayer used to measure the variation of the area of the denser phase. right) curve representing the time-dependent dimension of the L_β patches.*

The area values were obtained by image analysis on ImageJ and are plotted in the graph of Figure 2.18. The trend highlights a fast dynamic that reaches a saturation value, when, in this case, the lipid raft that was previously in L_o phase (Figure 2.19 a) phase becomes (almost) all L_β (Figure 2.19 b). The distributions of the corresponding heights in Figure 2.19c is in fact confirming that the main phases at the beginning of the measurements were separated by ~1 nm in height, in accordance with the coexistence of L_d and L_o phases; while by the end of the experiment almost all the lipids in L_o phase became L_β, as the difference raised to ~2 nm.

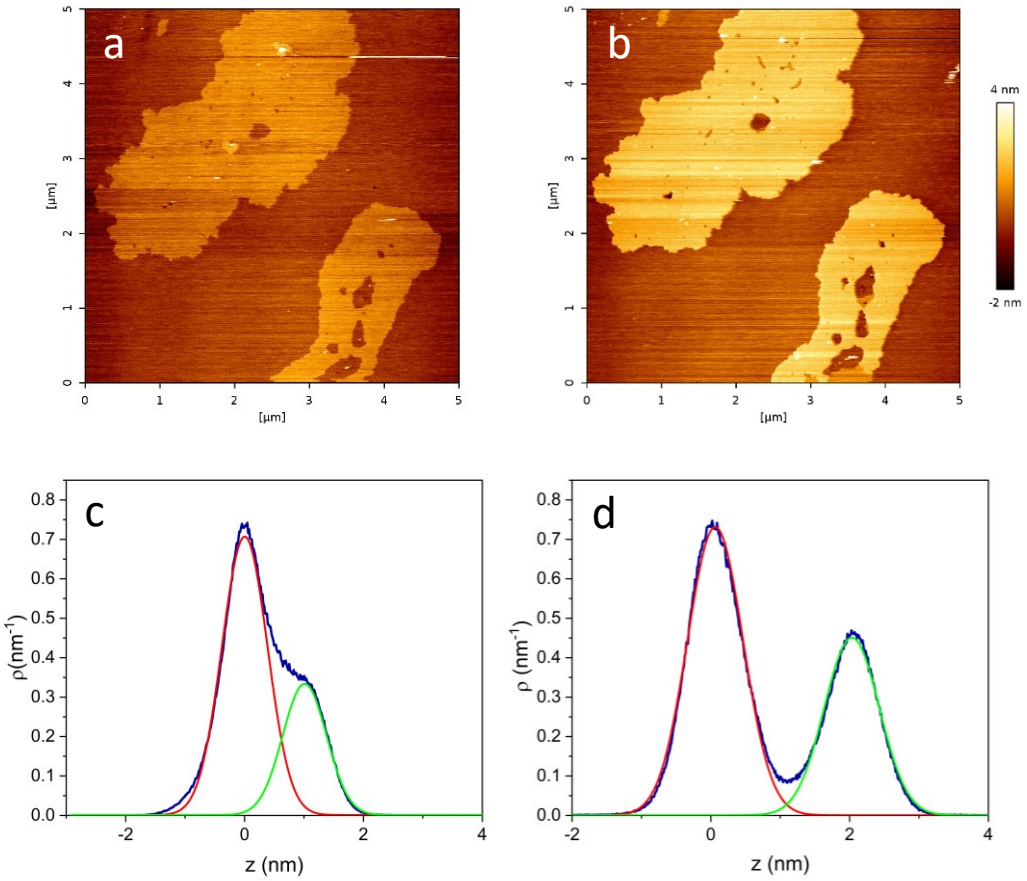

Figure *2.19: a) image at time zero from light irradiation, as previously depicted in* Figure *2.17. b) image after 90 minutes after the light irradiation began. c and d represent the respective height distributions.*
The red Gaussian fit in both graphs represents the distribution of the L_d phase for the initial and later states. The green fits illustrates the transition from the Lo to Lβ phase, providing a visual representation of the phase change.

Qualitatively, the lipid rafts in gel phase depicted in Figure 2.19b look very similar to those we showed in Figure 2.5, confirming the reproducibility of this result in different microscopes, at different concentration of Hyp and varied light dose; moreover, in this experiment we even showed the dynamics of the formation of the gel phase.
In any case, the interpretation of the result concerning the transition $L_o \rightarrow L_\beta$ is not straightforward, but it could be related to some effect on the local concentration of cholesterol.

Indeed, it has been investigated that Hyp and cholesterol in membranes stands in close relationship. Moreover, as highlighted by imaging, the transition begins from the L_o phase, which is the richer in cholesterol.

Hyp predominantly integrates into lipid structures with higher concentration of cholesterol, highlighting it as a critical factor for Hypericin's selective association, suggesting that cholesterol significantly influences Hypericin's selectivity in membrane environments. It has also been implied that Hypericin may form compact structures with cholesterol [46]. Lβ is typically characterized as a phase devoid of cholesterol. However, it seems improbable that cholesterol simply vanishes due to the photodynamic action of Hyp. Therefore, the exact mechanism of Hyp interaction remains unclear. It is uncertain whether Hypericin forms the previously mentioned compact structures that might hide cholesterol molecules from surrounding lipids, thereby mitigating cholesterol's effects, or if a complex involving Hypericin and cholesterol diffuses across the bilayer, leading to a decrease in cholesterol within lipid rafts. Another hypothesis is that singlet oxygen, generated during the process, could alter cholesterol molecules in a way that diminishes their effectiveness.

A potential solution to this issue would be to track the location of cholesterol during the transition phase. Unfortunately, we were unable to conduct such measurements in our study.

The time-dependent curves that showed the two dynamics in the bilayer revealed a trend that can be interpreted as a kinetics reflecting the action of a particular ligand and a response dependent on its concentration. As time progresses, it can be assumed that the production of $^1O_2$ and/or its action on lipids is growing, reaching a point when Hyp has exhausted the possibility to trigger new ROS.

$$^3O_2 + ^3Hyp \rightarrow {}^1O_2 \rightarrow response \tag{20}$$

This response could be either the formation of the gel phase, or the occurrence of pores on the bilayer.

The two dynamics can in fact be well fitted by a Hill equation [121] that highlights the relationship between concentration of a molecule A and effect E produced by it [122]:

$$E = E_{max} \frac{[A]^n}{[A]^n + [A]_{50}^n} \tag{21}$$

Where n denotes the Hill coefficient, which describes the steepness of the substance's dose-response curve, and $[A]_{50}$ represents the concentration of substance A that provides an effect equal to 50% of the maximum effect (*Emax*).

However, we are not able to access the direct information about the real concentration of $^1O_2$; we can only infer that there is a time-dependency of its production, therefore:

$$[^1O_2] \propto t \tag{22}$$

And Equation (21) can be written as:

$$E = E_{max} \frac{t^n}{t^n + t_{50}^n} \tag{23}$$

This equation is not linked to a precise reaction scheme; hence we can consider this as an empirical model that can describe qualitatively the phenomenology of the experiments. In any case, the fit with such equation is visualized in Figure *2.20 and the parameters it yields are reported in Table 4.*

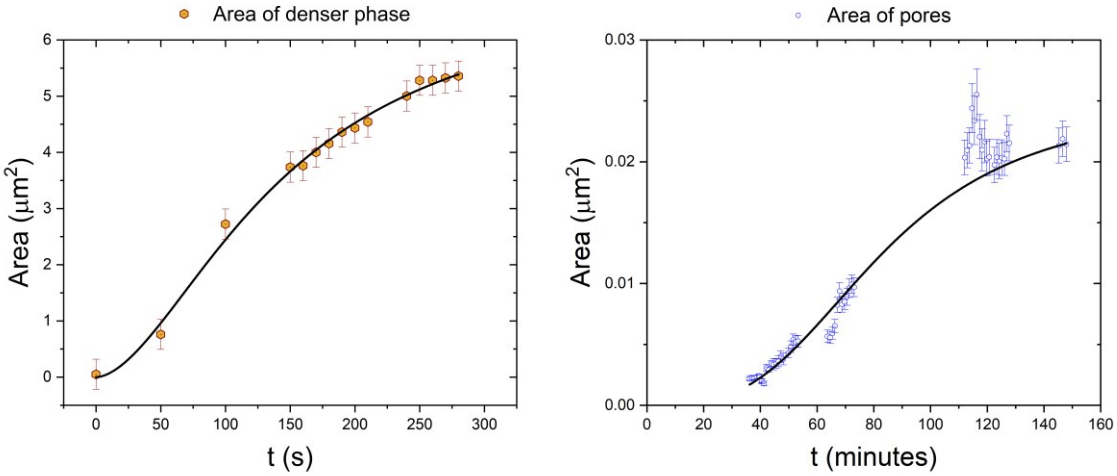

Figure *2.20: trends of time-dependent dimension of the L_8 patches (left) and of the newly formed holes (right). The black line represents the fit with a Hill equation*

Fitting parameters	*Denser phase*	*Pores*
t_{50}	144 ± 13 s	83.1 ± 1.5 minutes
n (Hill coefficient)	1.74 ± 0.17	3.15 ± 0.11

Table 4: results of the fitting with the empirical model of Equation (23) derived from the Hill equation.

The quality of the two fits in Figure 2.20 may indicate that the concentration of ROS indeed increases over time.

In general, the Hill coefficient is a parameter used in the Hill equation, which models how ligands bind to a macromolecule, such as an enzyme or a receptor. In this case it can indicate how effectively $^1O_2$ exerts its actions; both fits yield a value of the Hill coefficient, n, greater than 1 (Table 4).

A Hill coefficient greater than 1 is an indication of positive cooperativity in the ligand-binding process and reflects a scenario where the binding of one ligand increases the likelihood of subsequent ligand binding. Therefore, it can be assumed that the lipids are more inclined to be affected by the photodynamic action of $^1O_2$, which in turn increases its affinity to the phospholipids.

2.4.2 AFM imaging of Hyp + dark

Given the higher temporal and spatial resolution provided by the FastScan AFM, some measurement of imaging in dark were attempted. Our goal was to highlight if there was some reversible modification that wasn't detectable with conventional AFM.
However, even with the faster acquisition rate, no changes were detected in the dark for the untreated bilayer (data not shown). However, we did notice some peculiar difference between the untreated bilayers, and those with Hypericin in dark.
Qualitatively, whenever we added Hyp, we saw the borders of the lipid rafts being increasingly more rugged.

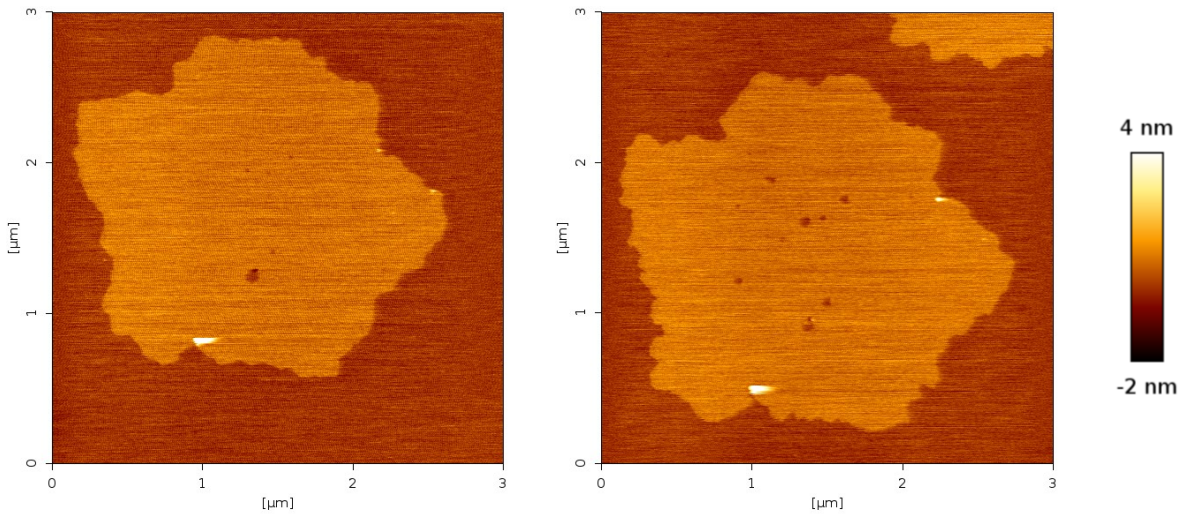

Figure *2.21: same region of the bilayer in the dark without the presence of Hyp (left) and after the addition of Hyp (right).*

We conducted a quantitative analysis of the edges of lipid rafts, which appeared to have fractal-like characteristics. For this purpose, we utilized a plugin in ImageJ designed to assess the fractal dimension of an image.
Fractal dimension is a way to describe the complexity of a fractal [123], which is a geometric shape that can be split into parts, each of which is a reduced-scale copy of the whole. This characteristic is known as self-similarity.
Fractal dimensions are applied in many fields, for example they are used to describe phenomena like the irregularities in coastlines [124].
Unlike the dimensions we are familiar with in everyday life (such as one-dimensional lines, two-dimensional squares, and three-dimensional cubes), fractal dimensions are not necessarily integer values. They can be fractional, which is where the term "fractal dimension" comes from.

This fractal dimension is linked to how jagged the structure is, and gives us a way to quantify how completely a fractal pattern fills the space as its size increases.
Mathematically, the fractal dimension is defined as it follows.
A straight-line segment possesses an inherent characteristic that, while obvious, merits explicit mention for the sake of broader generalization. Given an integer *N*, the length of a segment *L* is the sum of *N* segments of length *r=L/N*, the fractal dimension *D* of the segment L is [125]:

$$D = \frac{\log(N)}{\log(1/r)} \tag{24}$$

Which can be generalized for all shapes, yielding integer values for Euclid shapes and non-integer for more complex objects.
Operatively, what we did to calculate *D* of our lipid rafts, was to apply the box-counting method [126] which is a practical and common method, very often used in physics and environmental science [127].
It involves counting the number *N(ε)* of boxes of a certain lateral size *ε* needed to cover a fractal, and then seeing how this number changes as the size of the boxes is reduced (Figure 2.22):

$$D = \lim_{\varepsilon \to 0} \frac{\log N(\varepsilon)}{\log(1/\varepsilon)} \tag{25}$$

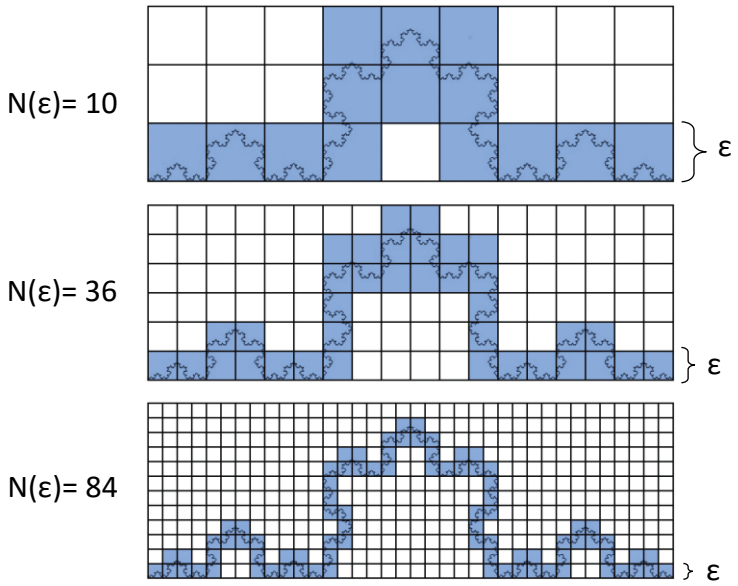

Figure *2.22: example of application of the box counting method on the well-known Koch curve. Adapted from* [128]. *Copyright © 2018 Ian Pilgrim and Richard P. Taylor. Licensee IntechOpen.*

The results of this analysis, involving 7 different ROIs, are shown in Figure 2.23a.
A representative ROI, before and after the injection of Hyp, is depicted in Figure 2.23b.
The first thing to notice from this analysis is that for either the control and the measurement with Hyp, we have a fractal dimension, which reflects the complexity of the objects. Secondly, we do notice a difference in the values of *D*, in particular there is a trend of a slight decrease of its value by adding Hyp. Although the variation is small (around 1-2%), it may indicate a difference in shapes, as also noted in prior studies [95]. Occasionally, the error bars overlap, which might be attributed to the algorithm used to calculate the D values, as well as potentially inadequate image edge quality for an effective plugin application.

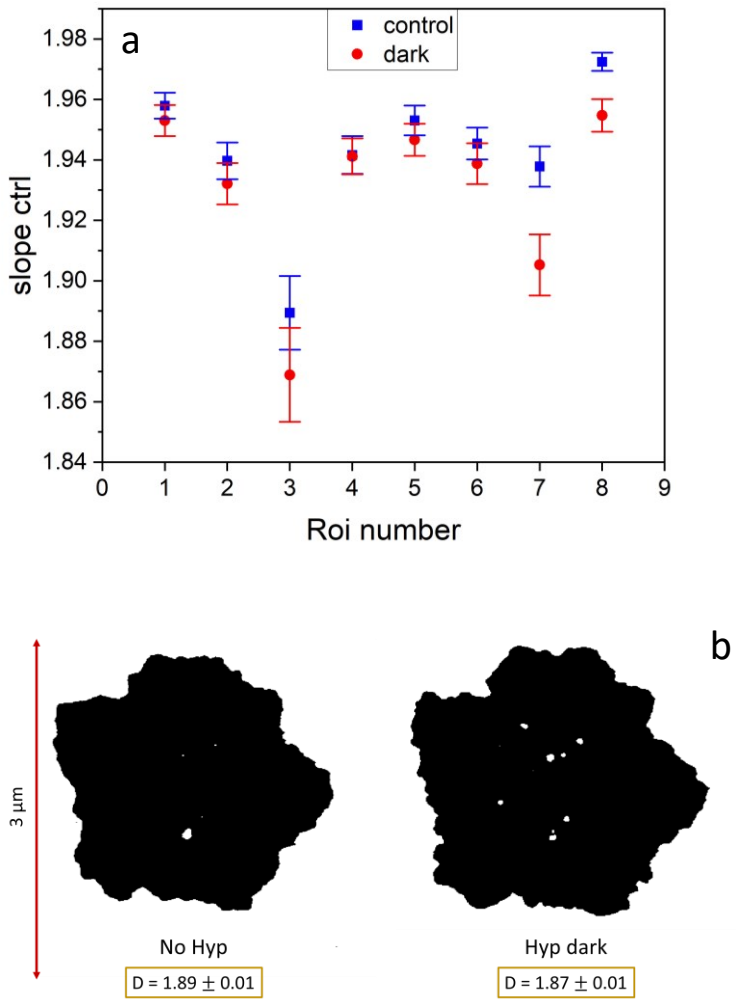

Figure *2.23: a) results of the analysis of fractal dimension using the Box counting method. The Roi number represent the area of a specific lipid raft. b) representation of the images processed from the software. The ROI is the same of* Figure *2.21: same region of the bilayer in the dark without the presence of Hyp (left) and after the addition of Hyp (right). The respective values of the fractal dimensions are depicted.*

The value we calculated considers the extent to which the raft domains can fill a two-dimensional space; stepping aside from the value of D=2, which would represent a Euclid 2D shape, the retrieved values further suggest that the topology of the system is affected.
Hence, it looks like Hyp is introducing some degree of instability to the system that is reflected in the shape complexity of the lipid raft.
One interpretation would be that Hyp is diffusing between the two phases, due to a gradient of affinity for either L_d or L_o. This movement can maybe induce tiny “pressure waves”, that results in an effect on the boundaries, causing the more pronounced corrugations of the lipid rafts. Nonetheless, it is reasonable to infer that Hyp's interaction with the membrane, being influenced by cholesterol presence, suggests a higher affinity for partitioning into lipid rafts, known for their cholesterol richness. However, this hypothesis requires confirmation, which can be achieved by using the fluorescence properties of Hyp.

2.5 Correlative AFM-fluorescence

The results obtained so far gave us some insights into the activity of Hypericin on membranes, but they don't account completely for the specific interactions involving the PS. Integrating fluorescence imaging with AFM would provide additional information, complementing the results outlined so far with morphological and mechanical properties of Hyp loaded membranes. The combined use of the two techniques compensates for each other's limitations, making them a powerful tool for studying interactions at the molecular level [91] [129].

For instance, with this approach we can address the question that was posed in the end of the last paragraph. Specifically, it allows us to examine whether Hyp molecules demonstrate a selective interaction with a particular lipid phase, thereby revealing their specificity towards the constituents of these phases.

This is relevant if we consider what we discussed about the interaction of Hyp and cholesterol. In addition to that, it was recently disclosed that some lipids have a role in enveloped virus infection, in the process that can be called "viral apoptotic mimicry". This strategy is defined by the viruses exposing phosphatidylserine, a marker for apoptosis, on their surface. This mimicry plays a crucial role in the viruses' ability to infect host cells and evade immune responses [130]. We might speculate if the antiviral properties of Hyp are derived not only from its stiffening effect but also from a particular interaction with phosphatidylserine, which is found in the L_d phase of our composition. Our hypothesis is that by combining fluorescence imaging with AFM, we can collect insights into this specific aspect, as well.

In addition to imaging, various fluorescence-based techniques, including FCS, can be integrated with AFM. This combination enhances the structural details provided by AFM with rapid acquisition of lipid dynamics information [131][132][133]. For our purpose, this technique could be beneficial for supplementing information about the dynamics involving Hypericin in the membrane, but also to confirm the results of the AFM mechanical measurements.

A change in the Young's modulus within the bilayer would indeed influence the diffusion coefficient, as both these physical properties are linked to the membrane's viscosity. To monitor potential differences in viscosity caused by Hyp using FCS, it's necessary to employ an additional fluorophore that operates in a distinct spectral excitation range from Hyp. This approach is crucial for differentiating the effects prompted by PS in darkness and under light irradiation.

2.5.1 Combined Confocal and AFM imaging in lipid bilayers

The initial step was to confirm the feasibility of using both techniques concurrently, which required a fluorophore that could provide clear contrast between the two phases. To achieve this, we used a phospholipid, dipalmitoyl-phosphatidylethanolamine (DPPE), labeled with a fluorophore, Atto647N from Atto-Tec. This fluorophore has been shown to partition distinctly between the two phases, L_d, and L_o. Moreover, it exhibits two different diffusion coefficients, each corresponding to one of these phases [134].

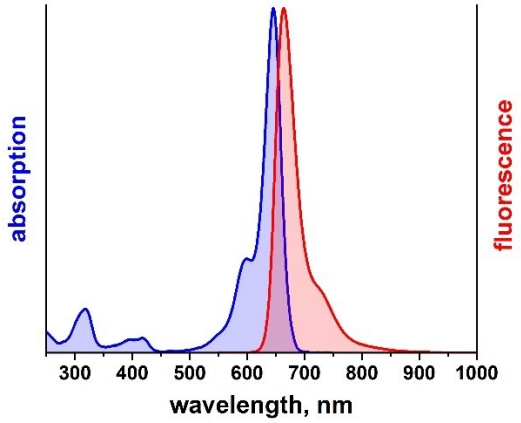

Figure *2.24: absorption and emission spectra of Atto647N from ATTO-TEC GmbH.*

Aside from the inclusion of the DPPEAtto647N, we decided to maintain the conditions as close as possible to those employed in the AFM measurements, to obtain a comparable bilayer, being consistent with the results previously obtained.

This means that, among all the kept conditions, we had to stick with the substrate we already used, i.e. mica. This substrate is ideal to grow very thin organic films (we will discuss in more detail in the Material and Methods), but it is not optically transparent, and it's birefringent too [135]; thus, it is not the best option for an inquiry with optical methods.

A possible solution to that would be to exfoliate the mica layer as much as possible to reduce its thickness, hence its optical density, and use it that way.

Despite numerous attempts, it proved impossible to achieve a stable environment for growing and utilizing bilayers on just a thin mica layer. The issue was primarily the substrate's increasing softness as layers reduced, causing excessive bending when placed on a microscope.

This made it difficult to contain the lipid solution and posed significant challenges for imaging, both optical and AFM.

To circumvent these problems, we adopted a more stable approach: placing a thin mica layer on a glass coverslip, bonded with transparent glue. This method, previously validated in studies [136][137], proved effective. However, this "handcrafted" support brings its own problems, such as optical aberrations and reduced transparency, leading to lower photon detection efficiency.

The main challenge, however, lies in the support's thickness. Many high numerical aperture objectives, used in confocal and STED microscopy, have a short working distance (typically under 150 µm), restricting the use of such high-quality objectives. Producing reliably thin supports with such thickness was problematic due to their fragility and the difficulty in peeling off the mica layer, essential for sample growth.

Given these constraints, for high-resolution studies, growing bilayers directly on glass appears to be the best option, despite its complexity and the need for more intricate sample preparation.
For the sake of the first steps of our inquiry, we didn't really have the urge to obtain super resolved images, since from AFM images we noticed that lipid rafts had remarkable dimensions, hardly below 1 µm.
Therefore, we employed the substrate of mica glued with glass coverslip by using an 40x water dipping objective with long working distance (3.3 mm) but low numerical aperture, 0.8. the maximum achieved resolution based on the Abbe's law would be:

$$d = \frac{\lambda}{2NA} = \frac{633\ nm}{2 \cdot 0.8} \cong 395\ nm \tag{26}$$

For the wavelength 633 nm used for the excitation of the DPPEAtto647N.
The images were acquired in the same system used for the AFM imaging, in 2.2.1, a JPK NanoWizard II coupled with a Leica Stellaris SP5.
The imaging process began with the acquisition of a confocal image focused on a particular area of the sample. This step was performed following a calibration of the optical system with the position of the cantilever, which will be detailed subsequently. Only at a later stage, the AFM images were performed. It is important to note that the measurements of AFM and confocal are spatially correlated, but they are not made at the same time; the reasons for that are multiple.

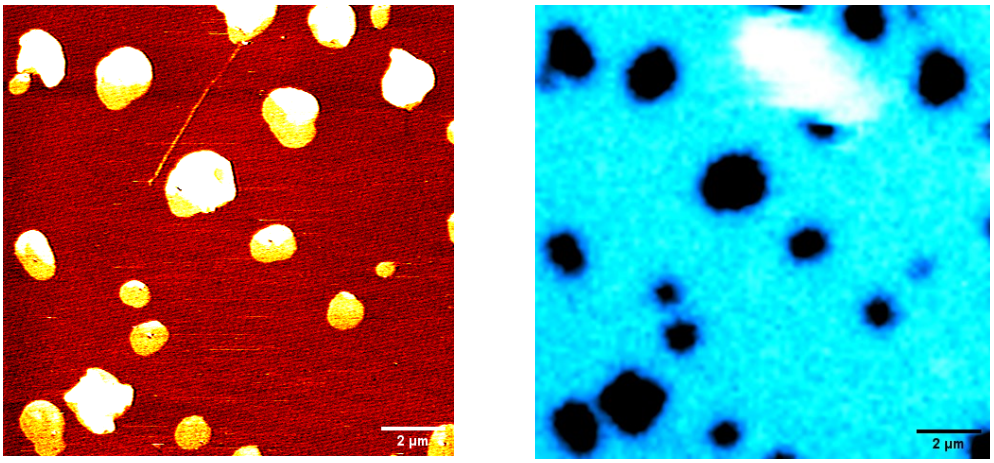

Figure *2.25: images of the same area of the bilayer, AFM on the left, confocal on the right, fluorophore used DPPEAtto647N. A gaussian blur with σ=300 nm was performed on the confocal image.*

The first is to secure the integrity of the sample, since there is a very high chance of breaking it while operating with the microscopes. This eventuality would also be detrimental for the microscopes themselves since pieces of glass could damage the objective and/or the AFM head.
The second reason is related to fact that the point light illumination of confocal can induce a high

electromagnetic density around the nanometric tip, that can have an impact on the interactions between the atoms of the sample and the tip itself.
After the acquisition we applied the ImageJ plugin StackReg to find the best correlation and to correct the possible spherical aberration of the confocal image. The images shown in Figure 2.25 are already corrected with the plugin.
Looking at the images we notice an almost complete correlation between the lipid rafts on the AFM image and the darker regions in fluorescence: this is confirming that, even with our mixture of lipids, the labeled DPPE partitions differently with the different lipid phases [134]. This is a very important result, because it confirmed that our bilayer can be studied with a multimodal and correlative approach, using indistinctly AFM and fluorescence techniques, depending on the purpose of the measurement.

2.5.2 Two color Confocal imaging

By means of correlative imaging, we demonstrated that areas with less concentration of DPPEAtto647N corresponds to the lipid rafts, confirming that such fluorophore has a different partition coefficient depending on the lipid phase. This feature is not directly linked to the native partitioning that the lipid should have, but mostly by the presence of the bulky fluorophore [134]; the lipid tagged with the fluorophore can move more freely in a less dense region of the bilayer, i.e. the L_d phase.
Based on this knowledge, we performed some two-color confocal imaging, labeling the bilayer with Hyp as well. This type of measurement is expected to provide information on the partitioning of Hyp. Indeed, a colocalization of fluorescence of Hyp with the dark region on the DPPE channel would be a proof that the PS is binds with higher affinity the denser lipid phase, or vice versa.

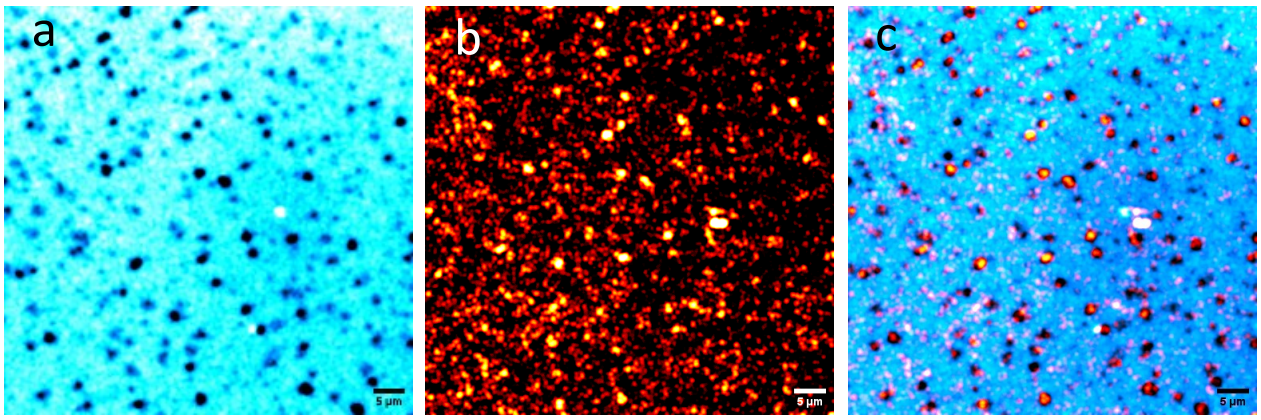

Figure *2.26: confocal images of the bilayer with a) DPPEAtto647N as a fluorophore, λ_{ex} = 633 nm, λ_{det} = (650-750) nm and b) with 1 µM Hypericin λ_{ex} = 561, λ_{det} = (570-620) nm. c) merge of the two channels. A gaussian blur of σ=180 nm was performed. Images are 512 x 512 px, with pixel size 125 nm.*

Figure 2.26 shows the fluorescence image of the bilayer in the two detection channels. We notice from the composite image in Figure 2.26c that a considerable percentage of the Hypericin fluorescence colocalized with the dark regions in the other channel, representing the lipid rafts.
To quantify that, we performed a statistical analysis, yielding the Mander's coefficients.
This value is a statistical measure used to quantify the degree of colocalization between two different fluorescent markers. In practical terms, Mander's coefficients helps in determining how much of one fluorescent signal overlaps with another signal: it measures how many pixels in channel 1 are above a certain threshold in channel 2, and vice versa.
The coefficient ranges from 0 to 1, where 0 indicates no colocalization and 1 indicates complete colocalization.
To obtain such coefficients we used an ImageJ plugin, which is called JACoP (Just Another Colocalization Plugin).
First, we inverted the image of the channel of DPPE (Figure 2.27a) so that the algorithm could analyze the correlation between the objects. Secondly, we set a proper threshold (Figure 2.27 d,e) and let the plugin do the calculation.

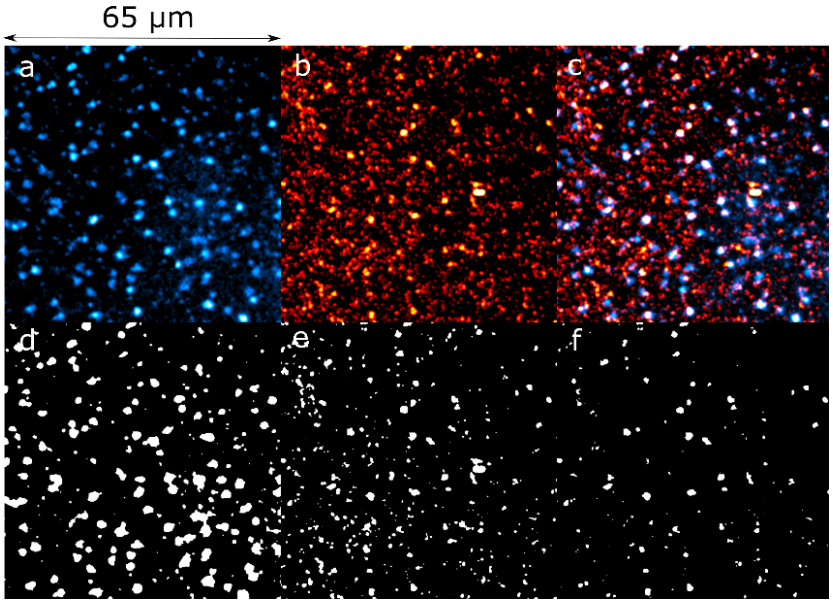

Figure *2.27: images used by JACoP for deriving Manders' Coefficients M1 and M2. a) inverted fluorescence image of DPPEAttO647N, b) fluorescence signal of Hyp and c) composite of a) and b). Additionally, d), e), and f) represent the respective masks of a), b), and c) that were generated following the application of a thresholding.*

We obtained two coefficients: M1=0.18, M2=0.5, representing respectively the degree of overlap of the first channel (the fluorescent lipid) over the second (Hypericin) and vice versa.
The value of M2 is therefore the most interesting, telling which is the fraction of Hypericin fluorescence colocalizing with the lipid rafts, that is 50%. This outcome suggests that interpreting the affinity of Hypericin for the phases of our bilayer is complex. The observed multivalent interaction with lipid rafts might be influenced by the formation of L_β regions within some rafts.

This formation could decrease Hypericin's affinity, possibly due to the lack of cholesterol in these regions. Unfortunately, we don't have the concurrent AFM data that would confirm this possibility.
During the same set of measurements, we realized that after a few minutes from the addiction of the photosensitizer, its fluorescence pattern was changing pretty much with respect to what was disclosed in Figure 2.26, as revealed by Figure 2.28. It is unequivocal that most of the fluorescence is coming from the disordered phase L_d and this event may be caused by either one of the following explanations, or a combination of them.

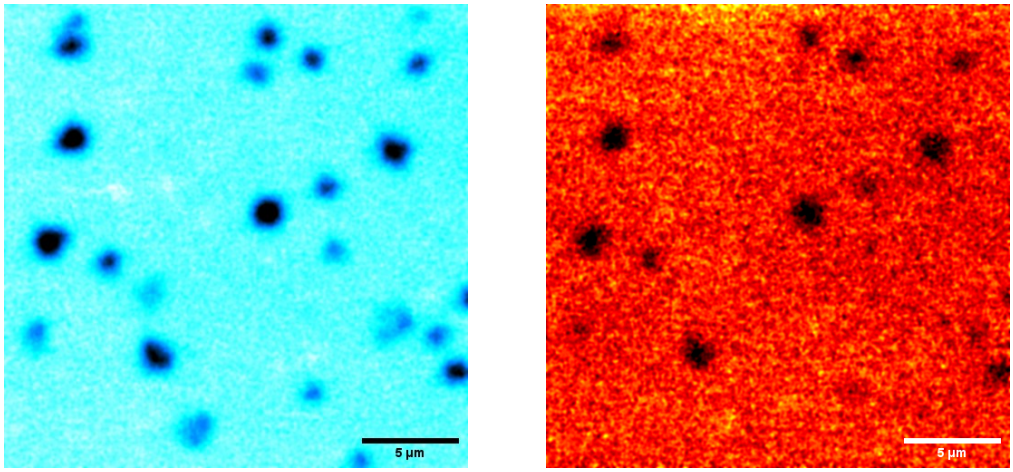

Figure *2.28: bilayer seen by using DPPEAtto647N (left) and 1 µM Hypericin (right). 512 x 512 px images. These images were acquired approx. 20 minutes later those shown in* Figure *2.26.*

The molecule may highly pack inside the lipid rafts, and for that reason there could be some self-quenching effect of the PS. This event occurs when fluorophores are in close proximity to each other, leading to non-radiative energy transfer between them, and as a result limiting the fluorescence emission. Another explanation is possibly in accordance with the previous AFM data. In fact, we saw that the effects of Hyp had two distinct dynamics, a faster one involving the lipid rafts and a slower one involving the production of holes in the disordered phase. In light of the new confocal data, such temporal division can be explained as a presence of Hyp in a specific lipid phase. In the first minutes after the injection of Hyp and irradiation, represented in Figure 2.26, L_o is the preferential phase where we find the photosensitizer, reflecting the specificity Hyp possesses for cholesterol. Later on (Figure 2.28) the specificity moves towards the disordered phase, reflecting an exchange between the two phases. The possible formation of compact and bulkier structures with cholesterol [46], as we stated **above**, could be the driving force of this mechanism.

2.5.3 Fluorescence correlation spectroscopy - preliminary measurements

More insights regarding the dynamics of Hypericin could be provided by Fluorescence Correlation Spectroscopy. The formation of compact structures of Hyp with cholesterol would be possible to trace due to an increase of the hydrodynamic radius that reflects in a reduced diffusion coefficient of Hyp when bound to cholesterol.
Moreover, FCS could be very informative on the effects of the PS on the environment of the bilayer. As stated **above**, many studies have highlighted the possibility to analyze lipid bilayer models systems with FCS [138], and sensitive enough to distinguish distinct lipid phases based on the diffusion coefficient [134].
The Stokes-Einstein equation relates the diffusion coefficient D with the viscosity η and the hydrodynamic radius r_H

$$D = \frac{k_B T}{6\pi\eta r_H} \tag{27}$$

Where k_B is the Boltzmann constant, and T is the temperature in K.
Even a small alteration in the viscosity of the environment is detectable through FCS. Therefore if the photosensitizers IMPACT on the viscosity of the bilayer, it become observable using a proper fluorescent probe, such as DPPEAtto647N. This molecule is particularly appropriate because it can be excited with wavelengths in the red where Hyp does not absorb any light. In this way it is possible to differentiate between the case of Hyp with and without light irradiation.
However, when FCS is applied to measure fluorophores in membranes, we faces more challenges than when used in solution. In membrane environments, diffusion tends to be slower, necessitating additional precautions. To prevent photobleaching, the use of very low excitation powers is essential. Additionally, to ensure a statistically significant number of independent events, long measurement are required. Ultimately, the length of the measurements is limited by the stability of both the experimental setup and the system under investigation.
Scanning FCS [139] serves as a significant example in this context. Its fundamental concept revolves around moving the excitation volume by scanning over the sample, effectively shortening the residence times on the fluorophores and enhances the statistical accuracy of the measurements.
Hence, it is essential to perform this kind of measurements on a laser scanning microscope such as our Leica SP5 confocal/STED setup.
In our application, we performed line-scan FCS measurements in which, instead of analyzing a fixed small volume, a line is rapidly scanned by the microscope. Apart from the reduced photobleaching, this method provides enhanced spatial information compared to traditional FCS. It captures molecular dynamics across a line, giving a more comprehensive view of molecular movements and interactions over time.

We chose line-scan FCS since the expected diffusion rate is a few $\mu m^2/s$ [134], accurately resolvable using the resonant scanner at 8 kHz. This approach also offers the advantage of time-resolved spatial information, enabling us to determine whether the raft is moving slowly during the acquisition process or if there has been a change in focus. Such insights are crucial for distinguishing actual data from artifacts. Additionally, this method allows for the simultaneous measurement of the diffusion coefficients of both components (L_o and L_d phases) in a single experiment. This is highly beneficial, ensuring that the focal volume remains consistent for both components, thereby guaranteeing the same point spread function (PSF) for each.

Unfortunately, our experiments with these measurements encountered numerous issues, leading to inconclusive results, which is why they will not be presented. More specifically, we faced challenges in differentiating the two phases based on diffusion coefficients, even in the absence of Hypericin. In most cases, a dominant fast component overshadowed the slower one, the latter associable with lipid diffusing on the membrane.

Previous studies have indicated that excessive substrate thickness can be the cause of poor results [132], causing spherical aberrations and distortion of the PSF, further exacerbated by the use of mica. Indeed, in the focal plane, the PSF deviates substantially from a Gaussian shape, complicating the application of standard FCS formulas that correlate the characteristic time with the diffusion coefficient. Additionally, the scattering effect of mica leads to a further reduction in the quantity of detectable fluorescence.

Clearly, refining the sample preparation and substrate engineering is a vital step to address these encountered problems. Opting for glass as a substrate seems to be the most suitable choice for such measurements. While our goal was to establish a robust and reliable platform for studying the effects of Hypericin on supported lipid bilayers, these effects should also be observable in other model lipid bilayer systems. For example, giant unilamellar vesicles (GUV), which have been thoroughly investigated using FCS [140] [141], are simpler to place on glass. Taking all these factors into account, our future FCS studies will most likely focus on this direction.

2.6 Conclusions

In this chapter we extensively analyzed the behavior of SLBs mimicking viral envelopes when the photosensitizer Hypericin is loaded. Through conventional AFM imaging, we observed a concentration-dependent detrimental impact of Hyp on SLBs with pre-existing defects upon light irradiation, attributed to the generation of $^1O_2$. Additionally, high-speed measurements conducted in Madrid enabled us to delineate the dynamics of the degradation induced by Hyp in defect-free bilayers, providing precise insights into the lipid extraction mechanism from the SLB. A denser lipid phase emerged when Hyp and light were involved, a phenomenon whose mechanism remains unclear; our hypothesis suggests that cholesterol redistribution in the bilayer could be a contributing factor. Correlative AFM-Fluorescence imaging provided valuable insights into the extent of the overlap between Hypericin fluorescence signals and lipid rafts, once again highlighting the multifaceted and dynamic nature of the photosensitizer.

The impact of Hyp in the absence of light appeared less conspicuous in the images, with the primary difference being the altered shape of the edges of lipid rafts, appearing more rugged.

Atomic force spectroscopy was employed to unveil the effect of Hyp on the nanomechanical properties of the SLB, through the measurement of the Young modulus and the breakthrough force. We observed an increase in the rigidity of the bilayer induced by Hyp, consistent with the aforementioned hypothesis. This effect was observable both with and without light for the case of the Young modulus but not for the breakthrough experiments. This instance provided evidence that Hyp has a distinct action towards elastic (indentations) and plastic (penetration) properties of the bilayer.

2.7 Materials and Methods

2.7.1 SLBs sample preparation

The bilayers preparation adhered to the same protocol consistently in all the measurements presented in this chapter. It follows the steps that I am going to discuss.

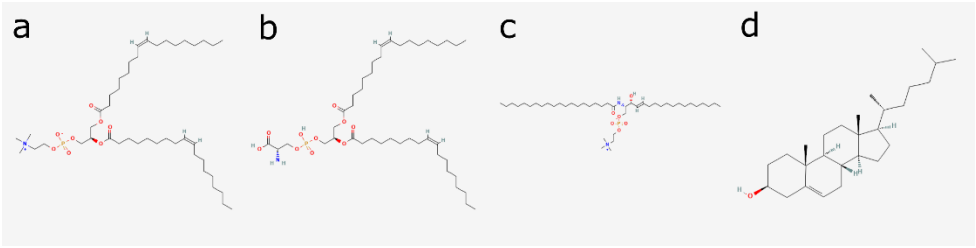

Figure *2.29: 2D-Structure images of a) DOPC, b) DOPS, c) Sphingomyelin and d) Cholesterol. Images obtained from PubChem; a) https://pubchem.ncbi.nlm.nih.gov/compound/10350317#section=2D-Structure - CID 10350317, b) https://pubchem.ncbi.nlm.nih.gov/compound/6438639#section=2D-Structure - CID 6438639, c) https://pubchem.ncbi.nlm.nih.gov/compound/44260124#section=2D-Structure - CID 44260124, d) https://pubchem.ncbi.nlm.nih.gov/compound/5997#section=2D-Structure - CID 5997.*

The constituents we used were:

- DOPC (1,2-Dioleoyl-sn-Glycero-3-PhosphoCholine), M_w = 786.1 g/mol - **66%** (unsaturated)
- DOPS (1,2-Dioleoylphosphatidylserine), M_w = 788 g/mol - **13%** (unsaturated)
- SM (Sphingomyelin), M_w = **20%** (saturated)
- Cholesterol, M_w = 388.5 - **1%**

The rationale behind the choice of the components of the bilayer was a compromise between choosing the real components of the viral envelope and having a sufficiently complex but stable system. Particularly, we carefully chose 4 out of 6 components of the viral envelope [52], first by maintaining a concentration ratio of 2:1 between DOPC and DOPS, which assures a certain stability of the L_d phase. Secondly, we chose the exact concentration of DOPS considering its negative net charge at neutral pH. In the viral envelope, the percentage of PS plus another negatively charged phospholipids PI (Phosphatidylinositol) is exactly 13%; hence by keeping DOPS at that concentration we ensured the correct polarity of the bilayer.
The remaining concentrations of Cholesterol and SM were chosen to secure the formation of lipid rafts with sufficiently large areas, to allow the investigation with imaging methods.

Preparation of the lipid suspension. We started with the stock suspensions of the single components already dissolved in chloroform and we prepared the solution with the chosen concentrations inside a glass vial, having a total of 1 mg of mixed lipids dissolved. We let the solvent evaporate with the help of a continuous flow of nitrogen, for about 10 minutes. After this process, a film of lipids was formed at the bottom of the vial which was ready to be used. We added 1 mL of ultrapure MilliQ water, in order to have a final concentration of 1 mg/mL. The addiction of water allowed the formation of LUV (large unilamellar vesicles) with eterogenous diameters.

Vesicle extrusion. In order to have the formation of a good homogeneous bilayer without defects it is necessary to have vesicles with the same size. A very well-established protocol to fulfill this is to perform a vesicle extrusion.

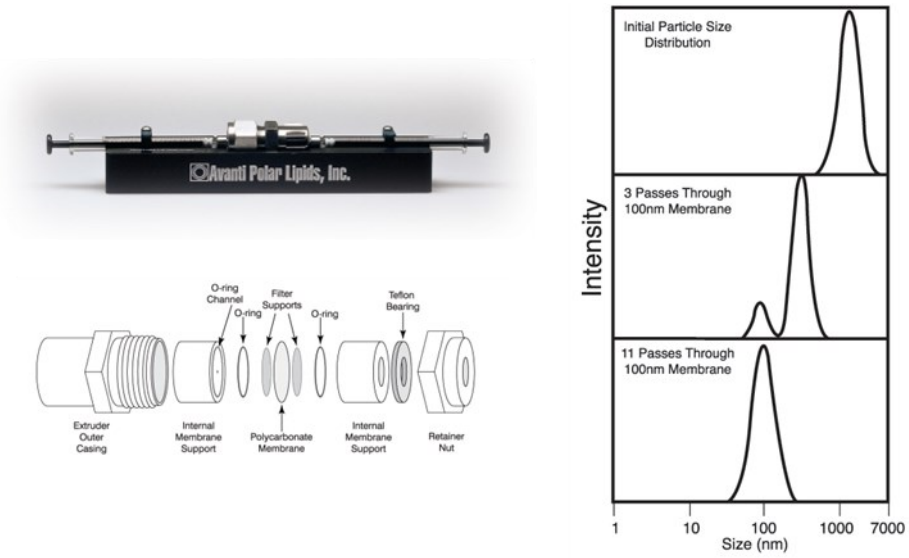

Figure *2.30: Avanti Mini-extruder, Avanti Polar Lipids, Inc. The images on the right represent DLS spectra of the size of the vesicles depending on the number of passes through the membrane. Copyright © 2024 Croda International Plc. All rights reserved.*

This protocol was based on the use of a Mini extruder (Figure 2.30). With the help of two Hamilton syringes of 1 mL volume, we let the suspension pass through a membrane with 100 nm size diameter pores. To reduce any variability in the protocol, we performed 19 passes through the membrane in each sample we prepared. Even though the company ensures that the mean size of the vesicles after 11 passes has already the desired value (Figure 2.30, right). The extrusion was performed over a hot plate at a temperature of about 60°, to have a gel-sol phase transition of the saturated lipids and to facilitate the formation of vesicles with multiple components.

After the extrusion, the lipid vesicles are ready to be used, at a conserved concentration of 1 mg/mL.

Deposition of the vesicles and formation of the bilayer. We followed a methodology in which the bilayer forms after the vesicles rupture and fuse onto the substrate [92], Figure 2.31.

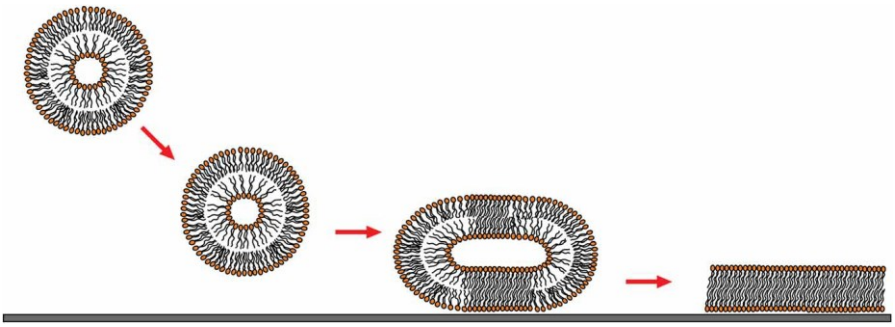

Figure *2.31: schematic representation of the SLBs formation by vesicle fusion. Adapted with permission from* [142]. *Copyright © 2008, Springer Nature Limited.*

For each bilayer we used a certain volume of the vesicle suspension in combination with fresh $CaCl_2$ solution, which facilitates the deposition. The exact volumes of the two solutions was chosen considering the area of the support, but in any case we kept constant their volume ratio:

- Lipid suspension (50 µL, 0.5 mg/mL) and $CaCl_2$ (8 µL, 10 mM) - For measurements of sections 2.1 - 2.4 with the exception of 2.3.2**.**
- Lipid suspension (25 µL, 0.1 mg/mL) and $CaCl_2$ (4 µL, 10 mM) - For measurement 2.3.2**.**
- Lipid suspension (25 µL, 0.5 mg/mL) and $CaCl_2$ (4 µL, 10 mM) - For measurements of sections 2.5.

Every sample were deposited on freshly cleaved mica foil, previously glue to a standard microscope slide (75 mm x 25 mm) or, for the case of 1 measurements, on a glass coverslip (ø = 25 mm, 100 µm thickness).

Muscovite Mica is a naturally occurring mineral, a silicate crystal with a peculiar, layered structure of sheets weakly bound together that exhibits perfect cleavage, i.e. they can be easily split into thin foils.

Using mica as a substrate is advantageous for several reasons. The first is that, by exerting a cleavage for each experiment, a fresh layer can be exposed, ensuring a consistently clean surface, ready to be used. Secondly, it provides a highly smooth and uniform surface, with atomic level flatness, (0.37 ± 0.02) nm [143] which ensures that the lipid bilayers stably form and spread evenly across its surface.

Following the deposition, the samples were placed in a humid chamber to inhibit evaporation during the preparation process.

They were kept at room temperature for 10 min and then incubated for 15 min at 60°C in a laboratory stove. The samples were then maintained at room temperature for 2 hours and then gently rinsed with MilliQ ultrapure water, to remove non deposited vesicles.
In the experiment shown in Figure 2.7a, we deliberately amplified this process to intentionally determine the bilayer's height.

2.7.2 Standard AFM imaging

AFM standard imaging that we reported in the section 2.2 was performed with a JPK NanoWizard II (Bruker, MA, USA) mounted on a Leica SP5 (Leica, Germany) inverted laser scanning microscope, placed on an active vibration isolation table. The stage of the light microscope has been substituted with a stage compatible with AFM, with minimal mechanical noise.

The chosen modality of AFM imaging was **tapping** (or intermittent) mode in liquid. In tapping mode, the cantilever oscillates at its resonance frequency. As the tip approaches the sample surface, it lightly "taps" the surface at the bottom of its oscillation cycle. This technique offers advantages over traditional contact mode AFM, where the tip continuously drags across the surface, potentially damaging delicate samples such as the bilayers we used.

We used V-shaped DNP silicon nitride cantilevers (Bruker, MA, USA) with nominal spring constant k=0.24 N/m and tip radius r=20 nm, while the resonance frequencies in air are in range (40 - 75) kHz, with a nominal peak at 56 kHz. In liquid conditions resonance frequencies shift to lower values, typically one quarter of those in air; indeed, the values in which we operated were in the range (13 - 15) kHz. We typically acquired 256 x 256 px or 512 x 512 px images at line rates 0.5-1 Hz; all those shown in the section 2.2 are 256 x 256 px images. All the images were analyzed with the JPKSPM software.

The light irradiation was obtained by means of a mercury arc lamp (Leica EL6000) and a bandpass filter at (515-560) nm focused on the sample with a Leica PLAN APO 10x objective, NA=0.4. The light power that was ~ 29 mW (with reference to its peak at 546 nm) and based on the illumination area we estimated a density of $\sim 0.2\ \mathrm{W/cm^2}$. Typically, the measurements started at max after 5 minutes of irradiation and then they were performed with continuous illumination.

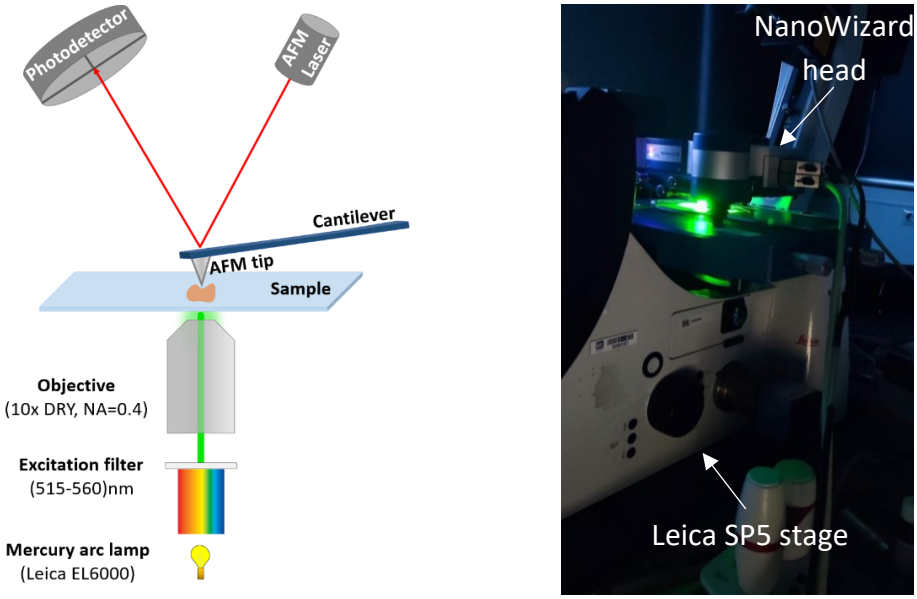

Figure *2.32: schematical representation of the configuration used (left). Actual picture of the setup (right).*

2.7.3 Mechanical properties by AFM: Young Modulus

AFM experiments to measure the Young Modulus were performed on a JPK NanoWizard III (Bruker, MA, USA) mounted on a Axio Observer D1 (Carl Zeiss, Germany) inverted optical microscope Figure 2.33, with a EXFO X-Cite 120Q 120W Metal Halide Lamp with a 550/20 filter for excitation. The measured power density was $\sim 2\ mW/cm^2$.

The measurements with light started after 20 minutes of irradiation and then they were performed with continuous irradiation. Differently from the NanoWizard II, this microscope allowed for imaging in QI (Quantitative Imaging), whose theoretical framework we discussed **above.** We used the same V-shaped cantilevers DNP mentioned earlier.

For the acquisition of reliable spectroscopic data, also comparable across different measurements, it was essential to precisely calibrate the cantilever. This ensured accurate knowledge of its sensitivity (a parameter that determines how effectively the cantilever can detect forces, in unit $[\mathrm{nm}]/[\mathrm{V}]$) and spring constant values:

- **Sensitivity:** after approaching the tip to the sample, we performed a force-distance curve of 1 µm total excursion in 1 second. The slope of the linear part of the curve yields the value of the sensitivity. Knowledge of the sensitivity is fundamental because it allows to relate the electrical signal output, measured by the photodetectors, to the real deflection of the cantilever. We found typical values of 12-15 nm/V.
- **Spring constant:** in order to obtain the real value of this parameter we performed the contact-free thermal noise calibration method [144]. We typically found value in the interval 0.3-0.4 N/m.

We acquired 128 x 128 px images of very small regions (0.5-1 µm), either inside or outside lipid rafts. The setpoint corresponding to the maximum force load was 1 nN, and the z-length of each F-D curve was 200 nm, and the residency time for each point was (3.8-4.2) ms, yielding a scanning speed of 2 Hz.

Figure *2.33: picture of the setup used for the nanomechanical measurements. It is placed on an active vibration isolation optical table as well as in an acoustic enclosure.*

Data analysis. To process the F-D curves (128 x 128 = 16384) we used the JPKSPM Data Processing software. For each curve we first applied some data smoothing and background subtraction. Subsequently we performed a fit on the linear part of the curve to set the zero, which would be the final point of the elasticity fit. Ultimately, we calculated the vertical tip position which automatically corrects the height signal coming from the displacement of piezo into the real position of the tip with respect to the sample. After this preliminary stage, we performed a batch processing of all the curves, setting the parameters for the Hertz-Sneddon fit (Equation (17)) to extract the Young Modulus. We set the radius of the tip as the theoretical value of R=20 nm, spherical shape, and we performed the fit on the initial part of the curve (Figure 2.34), that is when the deflection of the cantilever starts to rise, reflecting the contact with the bilayer. Fitting the whole curve wouldn't be meaningful because, after a certain rate of indentation, the contribution of the substrate would be prominent. Operatively, after setting the zero with the linear fit process, we ran the fit in the interval [0,5] nm, which we can see from the (Figure 2.34). The fitting process also determines the contact point value, which is identified as the point where the curve's slope begins to increase, marking the start of indentation. This value coincides with the indentation depth, δ.

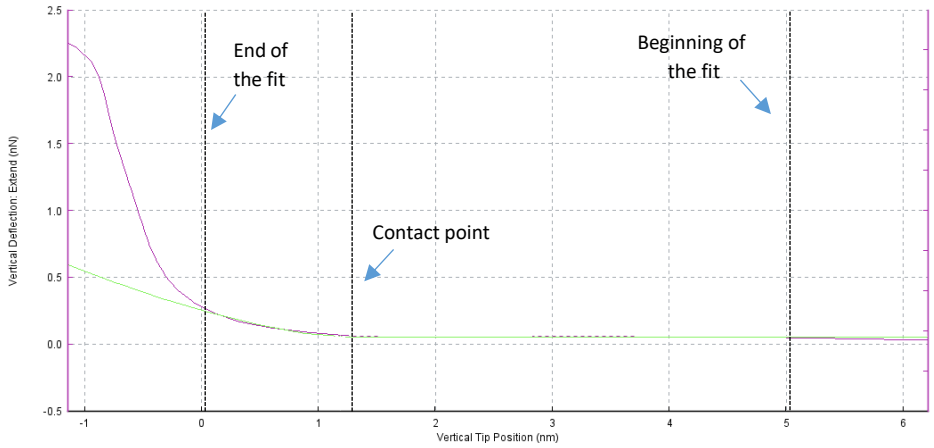

Figure *2.34: image from the JPKSPM software. The purple line represents an acquired F-D curve, while the green is represented the Hertz-Sneddon fit. The extremities of the fit are shown as vertical black lines, as well as the contact point.*

Accurately knowing the indentation depth is crucial for two reasons: firstly, to verify the fit's quality; typically, a depth of 1-1.5 nm suggests an accurate fit, whereas larger values might indicate that the fit erroneously includes excessive substrate influence. Secondly, the indentation depth is necessary for applying the Garcia correction to the Hertz Model (Equation (18)).
We already discussed that the uncorrected Hertz-Sneddon model provides a Young modulus that we can call "apparent", E_{app}. Such value should be corrected for the thickness of the sample, yielding the final value E_{true}. Unfortunately, in the JPKSPM software we can't fit by using

Equation (18) and directly obtain E_{true}; instead, we can only have information about E_{app}, and we need to make some extra passages to extract the value of E_{true}.

The force described by the Hertz-Sneddon model that we used in the fit is:

$$F_{meas} = \frac{16}{9} E_{app} \sqrt{\delta^3 R} \tag{28}$$

We can say that the measured force is equal to the sum of the contribution to the force which comes only by the interaction with the sample plus the force given by the substrate:

$$F_{meas} = F_{true} + F_{substrate} \tag{29}$$

Which equals, by definition, to the Garcia corrected force, F_g.
Equation (29) therefore becomes:

$$F_{meas} = \frac{16}{9} E_{app} \sqrt{\delta^3 R} = \frac{16}{9} E_{true} \sqrt{\delta^3 R}\,(1 + A + B + C + D) = F_G \tag{30}$$

$$\text{Where } A = \frac{1.133\sqrt{\delta R}}{h^1}, B = \frac{1.497\delta R}{h^2}, C = \frac{1.469\delta R\sqrt{\delta R}}{h^3}, D = \frac{0.755(\delta R)^2}{h^4}$$

From which we can calculate the value of E_{true} :

$$E_{true} = \frac{E_{app}}{\left(1 + \frac{1.133\sqrt{\delta R}}{h^1} + \frac{1.497\delta R}{h^2} + \frac{1.469\delta R\sqrt{\delta R}}{h^3} + \frac{0.755(\delta R)^2}{h^4}\right)} \tag{31}$$

For each QI image we obtained the E_{true} value by means of this correction formula. As already mentioned E_{app} and δ are rendered by the analysis in the JPKSPM software, R=20 nm, while h is given by the values of page 62. The height distribution of page 62 was obtained by means of the Statistical Functions tool of the software Gwyddion. The distributions of E_{true} were plotted in OriginPro.

2.7.4 Mechanical properties by AFM: breakthrough measurements

Breakthrough measurements were conducted on a Nanotec Cervantes AFM (Nanotec, Madrid, Spain) in jumping mode in liquid, by using the same V-shaped DNP cantilevers.
In jumping mode AFM, the cantilever is brought into contact with the sample surface for a very short duration and then retracted. This process is repeated as the cantilever scans across the

sample surface. The cantilever "jumps" or "taps" on the surface, spending most of its time away from the sample. The force exerted on the sample can be precisely controlled and minimized, which is crucial for studying soft biological samples, as well as highly detachable objects. Indeed, in addition to setting the force applied at each point during imaging, there is an option to define a maximum force threshold. If this threshold is reached due to various reasons such as debris contacting the tip or surface irregularities, the tip quickly retracts to avoid any damage.
Both the data acquisition and data analysis were conducted using the free software WSxM [145]. Before each experiment the sensitivity of the tip was calibrated by performing a F-D curve and fitting the linear part of the curve, equivalently to the methodology of the standard AFM. The value of the spring constant was kept at k = 0.3 N/m, a typical value for our cantilevers (2.7.3).
We acquired some images at low resolution (128 pixels per 1.5 µm - 3 µm) and low force (0.5 nN), to rapidly select a ROI with both L_d and L_o phases. Secondly, F-D curves were executed on the chosen phase. These curves, measuring 80 nm in terms of z-piezo displacement, commenced 20 nm from the bilayer. We sampled them at either 128 or 256 pixels, moving at speeds of 40 nm/s or 80 nm/s. Every Force vs. z-piezo displacement curve underwent analysis to derive force vs indentation curves, which provided the actual tip-sample distance on the x-axis. This process required calibrating the curves using previously determined values of sensitivity and the spring constant. Eventually, the values of the breakthrough force F_B were plotted in OriginPro, to obtain the distributions of Figure 2.10.
As a source of irradiation, we employed the ACE 1 Halogen Light Source with EKE Lamp, A20500 (Schott, UK), using a 475/35 filter. In this case the power measured was P_{490} = 2.5 mW, and the density was $\sim 1.5 \cdot 10^{-2}\ W/cm^2$. The measurements with light started after 15 minutes of irradiation and then they were performed with continuous irradiation.

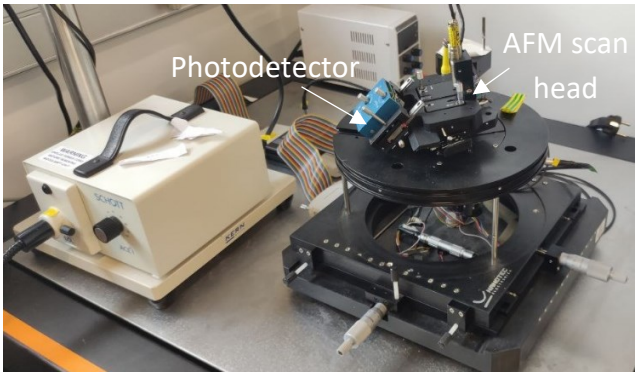

Figure *2.35: picture of the Nanotec setup that we used.*

2.7.5 High-speed AFM

AFM High-speed measurements were performed on a JPK NanoWizard V, with a Fast scanner to allow up to 150 lines/second. The AFM was mounted on a Nikon Eclipse Ti inverted optical microscope. All the set-up was placed on an active vibration isolation optical table. We employed

tapping mode in water at speed in the range 20Hz-80Hz depending on the image size. We typically acquired 512 x 512 px or 1024 x 1024 px images with pixel size never larger than 10 nm. We used FastScan D cantilevers, with tiny dimensions (16 µm length), resulting in extremely low inertia. The nominal tip size is 5 nm radius, which could provide very high spatial resolution. Sensitivity and spring constant were always measured for any experiment by the Sader's method [146], yielding typical values of, respectively, 8 nm/V and 0.1 N/m. The piezo z-range were reduced from 15 µm height (typical for standard AFM) to 1.5 µm, that allowed for improved speed and z-resolution.

In this case, we used a laser for the irradiation of the sample, a diode laser @488 nm, LuxX Omicron (100 mW-CW), focused with a 10x Nikon E Plan 10X, NA=0.25 objective lens. The typical power that we measured at the sample was $\sim$ 8 mW, yielding a density of $\sim 0.1 - 0.2\ W/cm^2$.

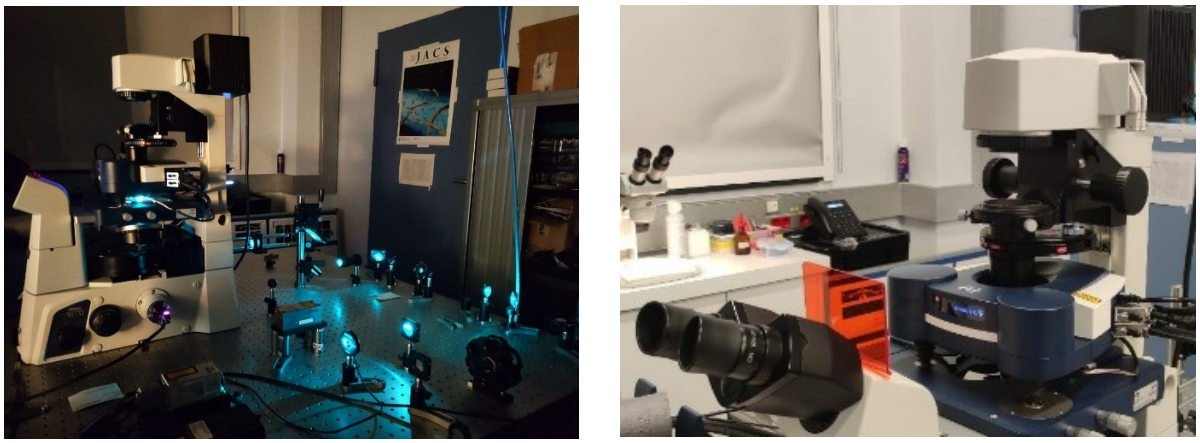

Figure 2.36: pictures of the setup. On the left we see the configuration that we used. On the right the detail of the AFM microscope head.

Image analysis. The images were acquired with the JPK Acquisition software installed, and treated with the latest version of the JPK Data Processing software by performing a plane subtraction and a line leveling. They were then saved in TIFF file, to allow the analysis in ImageJ. The dimensions of the areas of the defects and of the gel phase, as well as the perimeter of the defects, were in fact calculated in ImageJ.

We set an appropriate treshold value and then used the "analyze particle" command with a lower minimum of 9 pixels of size (Figure 2.37) before measuring the desired properties (area or perimeter).

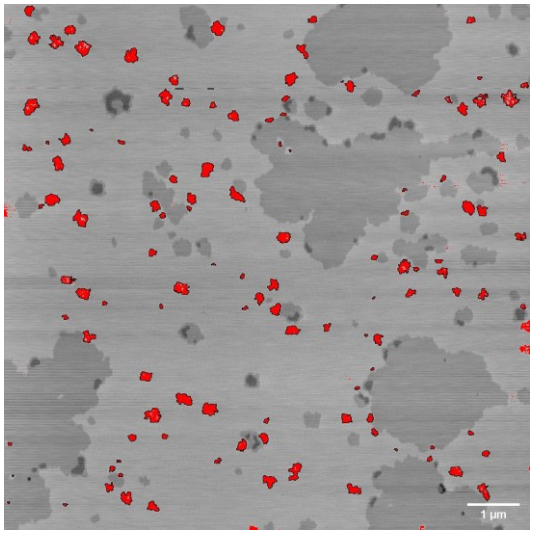

Figure *2.37: representative image of a sample after applying the particle analysis in ImageJ. The red spots are pores of the bilayer whose areas have been measured. The image is inverted in intensity to facilitate the application of the threshold (see* Figure *2.12f).*

The fractal dimensions were obtained by the box counting method, as we previously anticipated. Particularly, we performed a "2D B&W fractal dimension box counting" in the ImageJ plugin Multifrac [147] after the application of a FFT bandpass filter in the range [3-512] pixels. Such passage ensured the elimination of any horizontal inhomogeneous line, possible residual from the AFM scanning. The Multifrac plugin then selects N(ε) boxes of size ε to fill the Figures, and yields a line plot (Figure 2.38). The slope of the line plot yields the fractal dimension D, based on the Equation (25).

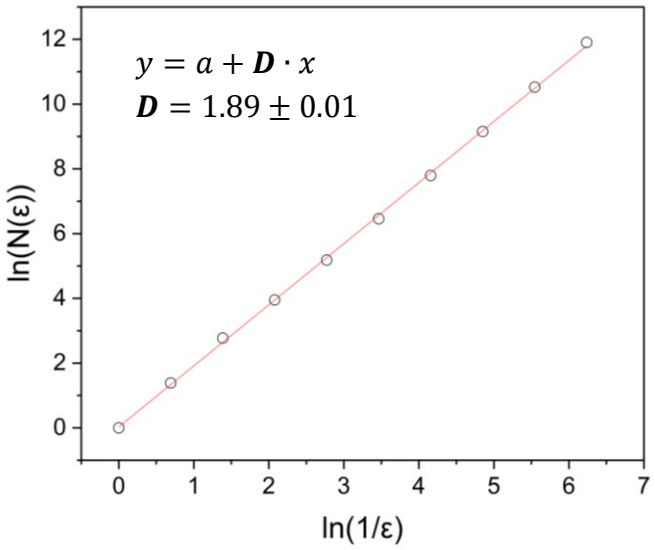

Figure *2.38: illustrative result of one fractal analysis by Multifrac.*

2.7.6 Correlative microscopy

The setup we used for the correlative measurements is the very same of 2.7.2**,** as well as the parameters for AFM imaging. The confocal imaging was performed by using the supercontinuum laser SuperK extreme (NKT Photonics) and selecting λ_{exc} = 633 nm as excitation source. We performed the experiment on a Leica 40x APO objective, NA=0.8, water dipping. We detected the fluorescence through a Leica HyD detector in the spectral region 650 -750 nm. An additional notch filter at 633/10 nm was employed, to eliminate any shot noise coming from the excitation laser. The imaging parameters were: 512 px x 512 px, and pixel size 154 nm, scan speed 1000 lines/s, 64 line averages, with pinhole size = 1 AU.

The process of correlation between the two microscope requires a calibration procedure that involves the employment of a module called DirectOverlay, available in the software of the NanoWizard II AFM; by performing the calibration it was possible to overlay the two images.

This manual calibration is based on the following steps:

- We captured a series of cantilever images in reflection mode using the confocal microscope. These images were taken at nine distinct positions within a 75 µm x 75 µm calibration area. The imaging was done with 488 nm at very low laser excitation, to prevent any photobleaching of the fluorophores. These images in reflection were acquired with a PMT in the spectral range 460-520 nm, with no notch filter activated. The scanning were performed at 1000 lines/s, with 16 line averages, to obtain 512 px x 512 px images.
- Confocal images were acquired over the same calibration area, with the parameters mentioned above.

At a later stage we imported the 9 images of the tip and the confocal image in the AFM software positions. Using the DirectOverlay method, we could set the tip position in each of the nine calibration images, which corrected the optical aberrations introduced by the optical microscope. The linearized optical image, now in AFM coordinates, was introduced into the AFM software's background and served as a reference for selecting sub-regions for AFM scanning. Ideally, this method should enable the merging of confocal images with AFM topographic images directly within the instrument's software. However, in practice, the tendency of bilayers to experience slight drift over time represented a challenge. Even a minor misalignment of a few nanometers was sufficient to prevent the accurate identification of lipid rafts for correlation analysis. Subsequently, we performed the overlay process on ImageJ software. Utilizing the StackReg plugin, known for its ability to correct various misalignments such as translation, rotation, etc., we successfully achieved the precise correlation needed for our study.

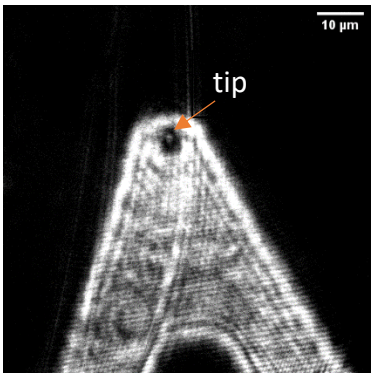

Figure *2.39: example of image in reflection of the cantilever. The tip is the small bright spot inside the dark circular area, indicated by the arrow.*

Sample Preparation of the DPPE labeled bilayer. In the correlative measurements we needed to label the bilayers**,** hence we had to change slightly the preparation described in the section **2.7.1.** We added 0.1% of the labeled phospholipid inside the lipid suspension, and then proceeded with the usual deposition. This concentration was sufficient to produce a strong fluorescence signal without altering the bilayer's behavior. [Hyp] = 1 µM.

2.7.7 Confocal microscopy

To image the bilayer with two color confocal we used the same setup configuration in the Leica SP5 microscope. We performed a frame-sequential scan with the two channels, acquiring first the signal for the DPPE (λ_{exc} = 633 nm, λ_{det} = (650 - 750) nm, channel 1) and then the Hypericin one (λ_{exc} = 561 nm, λ_{det} = (570 - 620) nm, channel 2). We employed two notch filters at 633 nm and 561 nm respectively. The imaging parameters were: 512 px x 512 px, pixel size from 50 nm to 125 nm, scan speed 1400 lines/s, 64 line averages for channel 1, 96 or 128 line averages for channel 2, pinhole size = 1 Airy unit.
For the bilayer preparation please refer to the previous section; [Hyp] = 1 µM.

2.7.8 Hypericin dilution and injection

Hyp was always prepared starting from the same stock of 1 mM in DMSO. The dilutions of the molecule were always carried out by using MilliQ ultrapure water. Each time we added 70 µL of Hyp solution, of a desired concentration on the side of the AFM prism, that allowed the deposition on the sample. Some of the concentrations that we used were already reported in the previous sections. For the high-speed AFM we employed 200 nM to 4 µM concentrations. It is to note that such values are referred to the concentration of the solution that is being injected, but it is not the real concentration on the sample. The bilayer is in fact covered in water during the acquisitions, which volume depends on the entity of evaporation. As a result, we typically ended up adding the 70 µL of Hyp solution in 100-200 µL of water, already above the sample; the actual concentration is lower than the nominal one.

3. AFM measurements of SARS-CoV-2

Throughout this thesis, we extensively discussed the interaction of Hypericin with SARS-CoV-2 and its photodynamic action on the viral particles, in an attempt to understand the underlying molecular mechanisms, and elucidate the antiviral activity in light- and dark conditions, by using model membranes. However, an enveloped virus represents a more complex system than a phospholipid bilayer, and it is crucial to study it in its entirety to confirm the previously obtained results. For the application on viruses, AFM was primarily used for examining the morphology in a liquid environment [148], even though its capabilities extend far beyond just surface imaging. The AFM cantilever enables manipulation of matter at an atomic level and the pulling of individual biomolecules. Recent years have seen significant research into the mechanical properties of virus shells. Studies have linked virus mechanics to factors like densely packed genomes, the maturation process, incorporation of artificial cargo, and structural changes [149] [150] [151]. Among the more informative experiments involving AFM on viruses we can mention:

- **Mechanical Fatigue experiments:** in general, fatigue measurements refer to the methods and techniques used to quantify the level of fatigue experienced by a material. Mechanical fatigue in virus shells refers to their ability to withstand a maximum force before undergoing structural collapse [152]. Not only this breaking force is critical, but also the way the virus disassemble can be very informative; for instance, the uncoating pathway of viruses can be replicated. It is for this reason that this methodology is applied in the context of AFM imaging. Indeed, it is performed by applying continuous AFM imaging for observing any structural changes in the protein shell under repeated low-force load cycles (usually 100 - 150 pN per pixel), demonstrating the stability of the shell against multiple deformations at such forces.
- **Nanoindentation:** this spectroscopic method, involves observing the deflection of the AFM tip when it interacts with individual protein shells. Once the tip makes contact with the particle, a Force-Distance (F-D) curve is registered, therefore indicating the mechanical properties of the virus. Usually, a linear behavior corresponds to the elastic response of the shell, that undergoes a deformation as it's being compressed. Nonetheless, when a critical point is exceeded, the indentation leads to particle breakage. The maximum bearable force can be called, also in this case, the breakthrough force. Once this force is applied, the virus typically undergoes large and uncontrollable changes in its structure. The structure changes after breaking can be visible from the difference in the F-D curves, e.g. the deformation shifts from linear to Hertzian if the virus shell is filled (Figure 3.1). In any case the curves can be fitted to obtain values of the Young modulus. Interpreting breakthrough and Young modulus is interesting to evaluate the stability properties of the virus. Finally, nanoindentation also reveals the potential self-recovery abilities of protein cages after breakage.

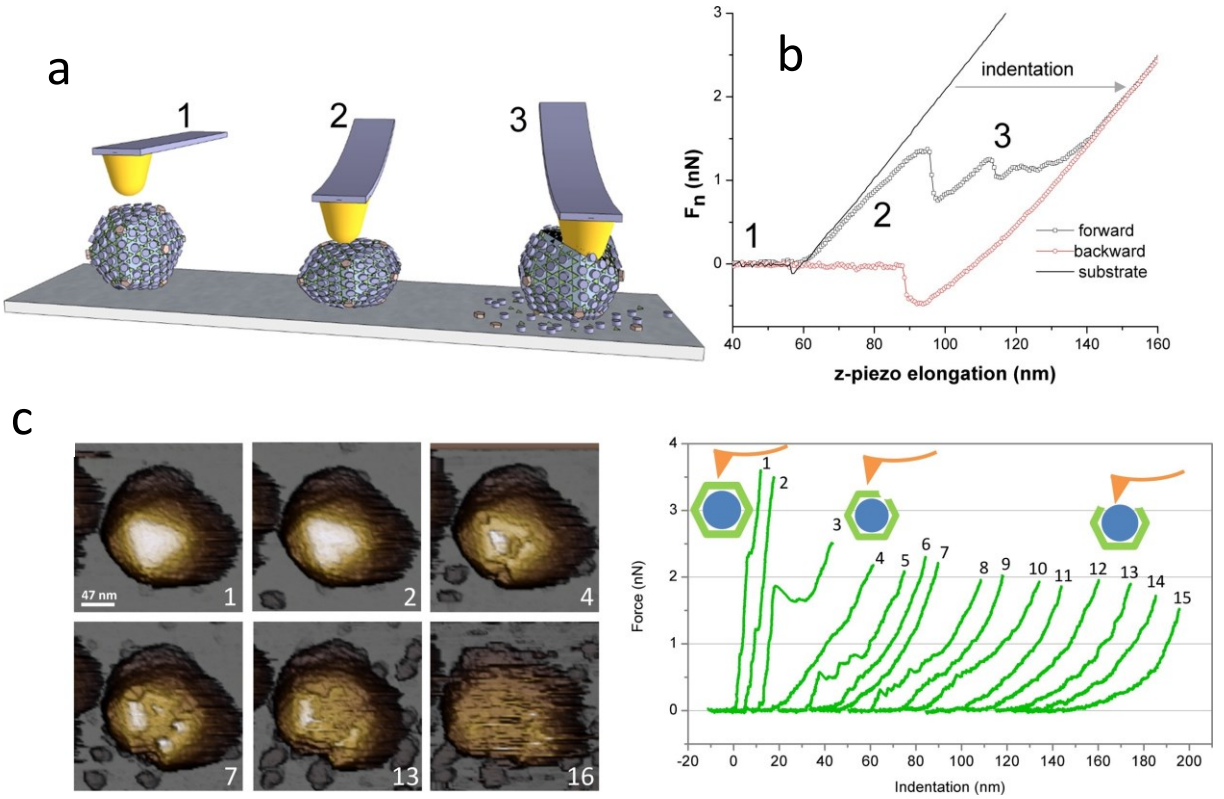

Figure *3.1: a) different moment of an indentation experiment, 1-before contact, 2-deformation, 3-after breaking. b) Force-Distance curve representing the stages described in a). c) images of a virus in different moments during a real nanoindentation measurement (left), and relative F-D curves (right). It's noticeable the behavioral change in the mechanics after breakage (happening in curve n°3) from the curves, and the corresponding disassembly in the images. Adapted with permission from* [116]. *Copyright © 2017 Elsevier Ltd. All rights reserved.*

All these things considered, we initiated a study focusing on nanomechanical properties and imaging of single SARS-CoV-2 viral particles by using AFM to uncover key characteristics. Our aim was, once again, to reveal the changes induced by the presence of Hyp, with and without light irradiation, with particular interest on the mechanical properties of the external layer, the viral envelope. Our hope was to be able to obtain coherent results with respect to those previously obtained with lipid bilayers.

All the experiments discussed in the following section were performed with the Nanotec Cervantes that we described **above**. This setup proves to be highly advantageous because of the possibility of applying jumping mode, especially useful for handling delicate and easily detachable samples viral particles [153], since it reduces drastically the lateral/dragging forces.

Another key aspect of this microscope is its scan head, which is tailored for optimal performance with extremely small fields of view (less than 500 nm). This makes it especially suitable for capturing images of individual viral particles.

Due to safety requirements, working with the active SARS-CoV-2 virus was not possible as it requires Biosafety Level 3 conditions. As a result, we decided to use an inactivated virus, which was different from the one discussed in **chapter 1.** The change was necessary because the chemical inactivation with paraformaldehyde introduces crosslinks that irreversibly alter the virus's mechanical structure. An alternative method we considered was heat inactivation. This approach partially degrades the viral RNA and membrane proteins, but it might also compromise the virus's structural integrity, including the envelope, as indicated in previous studies [154]. However, there is existing research on heat-inactivated viruses [155] that suggests it is possible to maintain intact viral particles, although this requires careful preparation of the sample.

3.1 AFM imaging

The initial experiments focused on assessing the basic characteristics of the viruses, including their shape, height, and overall conditions. In general, we expected intact and rounded object [155], coherent with the structure of SARS-CoV-2.

Imaging the spike glycoproteins on the virus's surface and determining their height relative to the envelope is improbable. This limitation stems from the imaging technique used, where a scanning tip likely sweeps over and displaces the proteins instead of accurately recording their heights. Nevertheless, it is feasible to identify potential debris of these proteins around the virus's rounded structure [156] (Figure 3.2).

Additionally, it's crucial to note that the observed height of the particles not only reflects their inherent structure but also their interaction with the underlying substrate. This aspect is particularly relevant for enveloped viruses, where the envelope imparts additional flexibility to the structure.

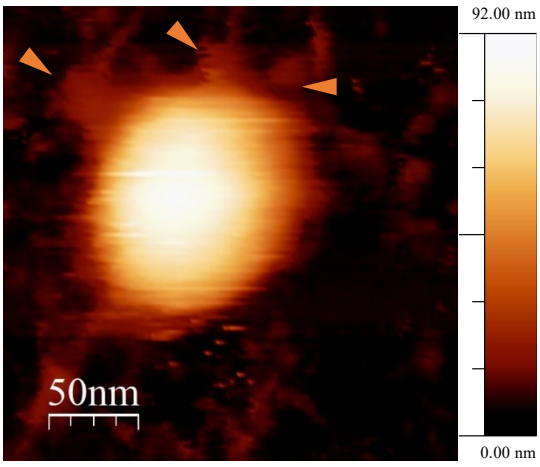

Figure *3.2: image of an intact viral particle deposited on mica. The orange arrows indicate possible spike leftovers.*

Figure 3.2 presents a typical Atomic Force Microscopy (AFM) image of an intact viral particle, which conforms to our expectations in terms of shape. Near the particle, there appears to be remnants of spike proteins. Further away, we observe other irregular formations that could be debris from damaged particles, such as proteins, RNA, or fragments of the viral envelope, possibly resulting from the inactivation process. It is unlikely that these irregular objects are caused by the poly-L-lysine substrate, as we have confirmed its surface to be quite flat and smooth, with very few impurities, typically measuring less than 5 nm in height.

The experiment of Figure 3.3 I am going to describe was aimed to investigate the resistance of samples to repeated imaging, i.e. a **fatigue experiment**. The outcomes of numerous fatigue experiments were consistent with those presented in Figure 3.3, which effectively represents the findings from several similar tests. Specifically, Figure 3.3a shows the initial image, and Figure 3.3b displays the final image from the fatigue experiment. These images were captured at a force of 50 pN, and the experiment spanned approximately 70 minutes, during which 24 images were obtained. Analysis of the images and the line profile in Figure 3.3c reveals that the virus did not completely disassemble. Instead, it appears to have lost some material, as indicated by a height difference of about 10 nm. This observation is particularly noteworthy as viruses with protein shells typically disassemble more clearly in such experiments. On the contrary, the presence of a phospholipidic envelope is believed to impart a degree of pleomorphism to the virions, allowing them to alter their structure under mechanical stress, not collapsing completely.

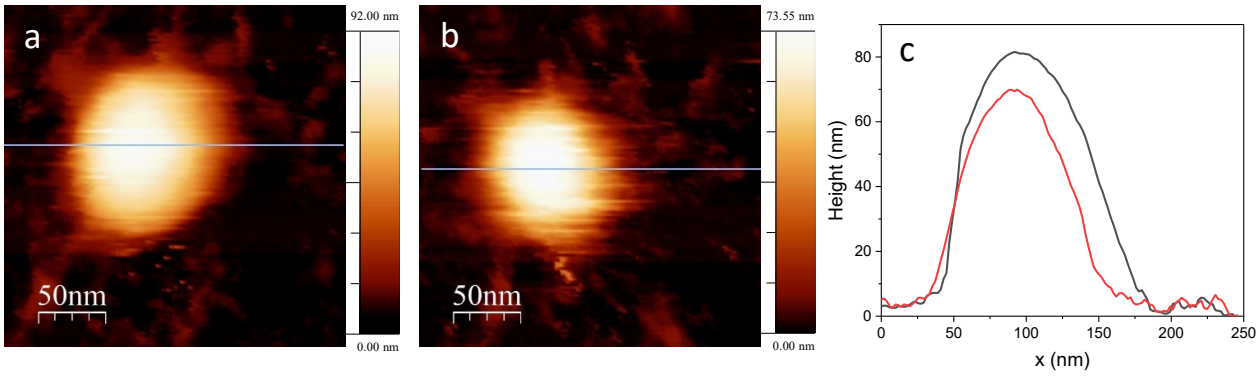

Figure *3.3: an example of fatigue experiment is visualized. The height difference between a) the first image and b) the last is plotted on the line profile c).*

There is an increasing evidence that such structural adaptability is relevant from an evolutionary point of view. Indeed, virions can be exposed to physical forces that have the potential to deform or fracture them, whether they are outside or inside cells. These forces encompass shear stresses encountered as they move through viscous fluids, or during extrusion through nuclear pores or similar constrictions, osmotic influences, pressure resulting from the packaging of double-

stranded DNA, hydrostatic pressures, and capillary forces, etc experienced during desiccation, among others.
It is plausible to suggest that viruses may have developed distinct mechanical characteristics as an evolutionary response to the various selection pressures exerted by different forces. This adaptation would serve to either endure these forces or potentially leverage them for their own benefit [157].
Additionally, the stiffness of some enveloped viruses like MuLV or HIV-1 have been studied in different conditions and different stages of the maturation cycle, central for understanding the virus's infectivity and interaction with host cells. Interestingly, it has been disclosed that the immature virions are much stiffer than the mature ones , which are in turn more infective [158] [159]. This reveals that the mechanical properties of viruses envelopes/shells are metastable, and their function is governed by the biolophysical process the virion must endure.
Therefore, as we already reported, the behavior of the SARS-CoV-2 virions exposed to fatigue measurements that we showed in Figure 3.3 may reveal the structural adaptability and softness of such virus. As a consequence, we might have considered to perform some mechanical measurements extracting the value of the Young modulus, by adding Hypericin as well. Anyway, our goal was to underline the differences that Hyp is introducing in relation only to the viral envelope, by itself.
The question that we asked ourselves at this point was: can we say that the adaptability of these viruses is given only by the presence of the viral envelope, and more specifically of the phospholipidic bilayer? The answer is, most likely, that the conformational changes that the virions undergo are more complex. Hence, it would be an over simplification to say that the mechanical properties are governed only by the presence of the envelope. The RNA packing, as well as membrane proteins [159] have a role.
Additionally, as we reported in the paragraph 2.3.1, correct evaluation of the Young modulus requires the knowledge of the thickness of the sample. Given the variability of heights of the viral particles (40 - 100 nm), would have required a lot more statistics than the available one.
These are the reasons why we didn't perform any measurement with the purpose of knowing the Young moduli of our viruses.

3.2 AFM nanomechanical properties

A more direct measurement to assess the mechanical properties (only) of the viral envelope is the evaluation of the breakthrough force. Such force is, in fact, related to the properties of the more external layer of the virus, i.e. the envelope, and it's not dependent on the height of the dimension of the virus. The measurements were performed in the three conditions of **no Hyp**, **Hyp in dark** and **Hyp under light irradiation**, with the aim of detecting the possible changes induced by the molecule, similarly to what we measured in 2.7.4**.** Being able to compare the F_b values of the viral envelope with what we obtained with the bilayer model system would be ideal.

However, our study used cantilevers that differed from those used in the above cited measurements, featuring sharper tips and a with a distinct shape.
Consequently, directly comparing the absolute force values was not feasible. Additionally, to ensure effective Hyp incorporation into viral particles, we mixed the PS and the virus in an Eppendorf and then applied the solution onto the substrate, as detailed in the Materials and methods section. This approach precluded the possibility of directly comparing the same viral particle before and after Hyp administration. At the same time, even if we had chosen to administer Hyp directly onto the sample, it is highly improbable that we would have been able to identify and select the exact same virion for observation.
The measurements were not easy to carry out, because we didn't always obtain "clear" breakthrough, revealing tip penetration on an intact structure. That instance was due to indentation on already broken virions, not immediately distinguishable from imaging, most likely due to the inactivation process that introduced many inhomogeneities on the sample. Moreover, even with intact particles, we obtained breaking of the structure after several indentation cycles (typically 5-10 indentations) in accordance with previous results [155], and once again revealing the resistance of the viral envelope of SARS-CoV-2.

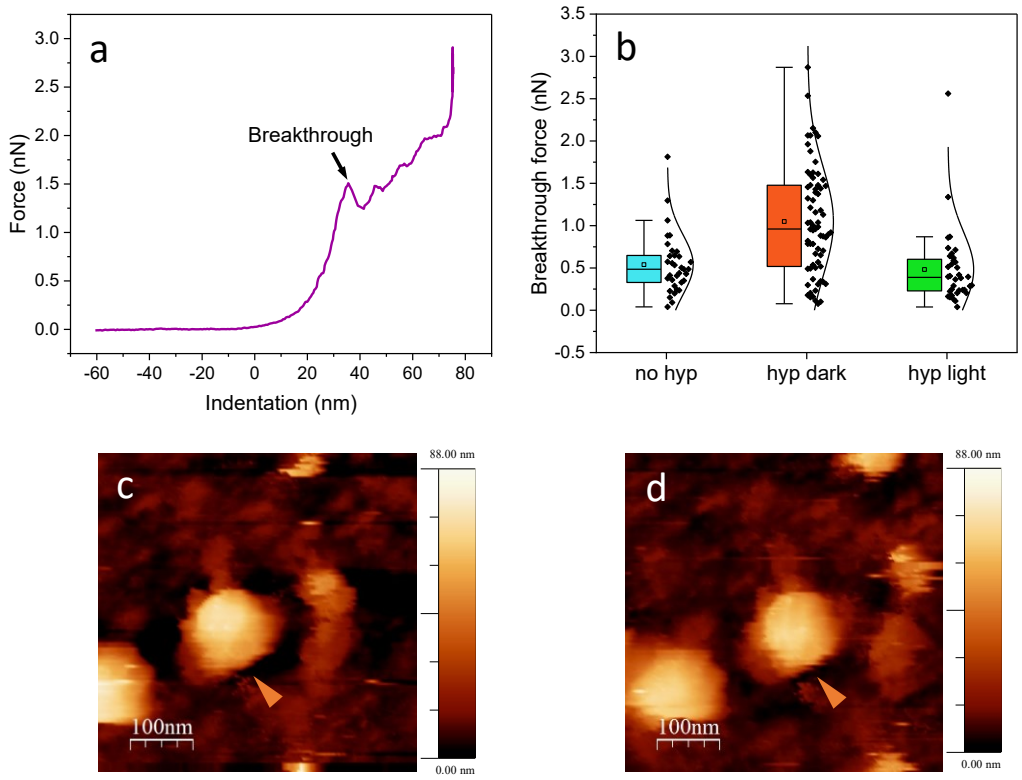

Figure *3.4: a) typical F-D curve in which a penetration in the envelope is visible; b) distributions of the detected breakthrough forces in the three conditions, [Hyp]=1µM; c) image of the viral particle (indicated with the orange arrow) before indentation and d) after 15 indentation cycles.*

Typical F-D curves we used for the analysis with a clear breakthrough are represented in Figure 3.4a; analogous curves served for the analysis depicted in the chart of Figure 3.4b. Apparently the F_b of the pure virus yielded a value of around 500 pN (Table 5) reflecting a very soft layer, in accordance with the phenomenology of enveloped viruses which was previously discussed.

[Hyp]	*N° of curves*	*Breakthrough force*
0 µM	34	(0.54 ± 0.03) nN
1 µM in dark	71	(1.05 ± 0.06) nN
1 µM in light	36	(0.48 ± 0.04) nN

Table 5: the results of the analysis showed in Figure *3.4b are summarized here.*

In the presence of Hypericin, we observe a change in the sample's properties, which varies under light and dark conditions. Intriguingly, this trend seems to align with our previous findings for bilayers (section **2.3.2**), where Hypericin only caused the virus to stiffen in the absence of light. However, there is considerable variability in the sample, as evidenced by the data dispersion for the "Hyp in dark" condition shown in Figure 3.4b, and on the number of curves analyzed, as detailed in Table 5. As mentioned earlier, breaking the viruses, or finding intact viral particles was not always possible, leading to a discrepancy in the number of curves across the three conditions. Ideally, we would have a similar number of curves for each condition to equally account for data fluctuations.

However, the dispersion of the data showed in the Hyp in dark condition, could also be related to the uneven distributions of the number of Hyp molecules in the virions, similarly to what we reported in Figure 1.4b. In that scenario, the distribution of fluorescence intensity was inhomogenous, indicating that certain virions contained a higher number of Hyp molecules, while others had fewer, for a same concentration. The observed decrease in dispersion upon illumination might be connected to the phenomena described in Section 2.3.2 regarding the rupture of bilayers. It is possible that Hyp has a more significant structural impact in darkness than under light exposure. In the latter case, processes such as lipid peroxidation and the breaking of double bonds might come into play, potentially altering the plastic material's properties to a state similar to when Hyp is absent.

Lastly, by conducting imaging before and after the indentation cycles, we found that the particles did not disassemble post-breakthrough, which is quite remarkable Figure 3.4c, d). This might suggest that the mechanical damages inflicted on the external layer of the SARS-CoV-2 viruses could be reversible [160].

3.3 Conclusions

From the data collected in our experiments, we have obtained some initial insights into the behavior of heat-inactivated SARS-CoV-2 viral particles when subjected to mechanical stress. The fatigue experiments suggest that the virus has an extremely adaptable structure, which aligns with characteristics typical of highly infectious viruses. The initial results upon applying Hypericin indicate the potential to monitor induced changes in the virus's stiffness, though these findings are still at a preliminary stage. The extent to which heat inactivation may negatively affect our measurements remains unclear; the sample's variability currently prevents us from making conclusive statements about the effects of Hyp on its nanomechanical properties. Thus, additional data are needed to develop a more comprehensive understanding and offset the sample's heterogeneity.

3.4 Materials and methods

Sample preparation. The SARS-CoV-2 stock of viral particles were prepared in the BSL3 laboratories at Istituto Zooprofilattico Sperimentale della Lombardia e dell'Emilia Romagna in Brescia, similarly to what we discussed in 1.6.5. The inactivation was performed by heat-inactivation at 65°C for 30 minutes in MEM culture medium. The samples were neither ultra-centrifugated nor resuspended in PBS. The viral suspensions were stored at -80°C until the measurements. The protocol used for the preparation of the samples was the following:

1. Application of 40 µL of poly-L-lysine onto a freshly cleaved mica piece (0.5 cm x 0.5 cm), which was previously attached to a circular metallic support with a diameter of 18 mm.
2. Waiting for 15 minutes, then rinsing thoroughly with ultrapure MilliQ water three times. After each rinse, a nitrogen gas flow was used to dry the surface.
3. To disperse any aggregate, the Eppendorf containing the viral particles was vortexed five times, with each vortexing lasting for 5 seconds.
4. Placement of 50 µL of the vortexed particles onto the mica surface.
5. After another 15 minutes, addiction of 20 µL of TRIS buffer (5 mM) mixed with NaCl (150 nM) at pH 7.4, to maintain appropriate osmotic pressure and pH levels.
6. Following 15 minutes, three rinses with the same buffer to remove all unattached virions and debris, and addiction of the right amount of liquid for the measurement (usually 40-50 µL).

For the experiments with Hyp, we prepared the Eppendorf with the virus by adding the PS so that the total concentration would have been 1 µM. We let it incubate in Eppendorf for 15 minutes. after this passage, we proceeded with the same protocol.

3.4.1 Imaging

The jumping mode in water was used for the experiments. We chose the rectangular qp-BioAC cantilevers from NanoAndMore, characterized by a nominal spring constant of 0.1 N/m and tip radii of less than 10 nm. The calibration process followed was the same as described in section 2.7.4, resulting in typical sensitivity values around 6-7 nm/V. As with previous experiments, both data acquisition and analysis were performed using the WSxM free software. The images were captured at a resolution of 128 pixels within very small fields of view (200-500 nm) and using very low forces (less than 100 pN) to preserve the integrity of the virions. We conducted the fatigue measurements under the same conditions with forces ranging from 50 to 150 nN.

3.4.2 Nanomechanics

For the nanomechanical measurements, we began by selecting an appropriate virion and centering the ROI on the midpoint of the particle. We then performed F-D curves with the aim of obtaining at least one breakthrough event. These curves started 40 - 60 nm away from the sample. The total z-piezo displacement length varied depending on the viral particle's size, typically ranging between 100 – 160 nm. We recorded these at resolutions of either 128 or 256 pixels, with speeds between 100 – 150 nm/s. After the set of F-D curves, we performed an image of the viral particle to assess its integrity, checking if damage, collapse, etc. had occurred.
The analysis involved selecting only the clear breakthrough forces, which constituted less than 50% of the total curves acquired. We first calibrated the curves in WSxM to obtain the actual tip-sample distance. Then, the breakthrough force values (FB) were plotted in OriginPro to analyze the distributions.
For these measurements, we used the same source of irradiation as in the experiments with the bilayers (refer to 2.7.4).

4. Conclusions and future perspectives

Overall, this thesis presented a comprehensive study on the interaction and the effects of the photosensitizer Hypericin with a model of enveloped virus, i.e. SARS-CoV-2, and lipid bilayers resembling the viral envelope. We employed multiple biophysical techniques, either optical or scanning probe methods, also used in a correlative way.

When Hyp is bound to SARS-CoV-2 and exposed to light, it demonstrates significant antiviral effects by generating reactive oxygen species. Intriguingly, even in the absence of light, Hypericin induces an antiviral response, suggesting an additional mechanism. This secondary mechanism, while requires a higher concentration, appears to involve Hypericin embedding into the viral envelope, potentially altering its fluidity.
Ultimately, Hyp emerges as an effective antiviral agent operating both light-dependent and independent mechanisms, each requiring further characterization for a comprehensive understanding.

For this purpose, we employed Supported Lipid Bilayers (SLBs) that simulate viral envelopes.
We observed concentration-dependent detrimental effects of Hypericin on SLB morphology, particularly in pre-existing defect regions under light exposure. We also noted similar effects in defect-free bilayers, but at higher concentrations. We provided detailed insights into the degradation process, including lipid extraction and the appearance of a denser lipid phase, through high-speed AFM imaging. Such effect consisted in the appearance of a denser lipid phase, likely due to the redistribution of cholesterol within the bilayer, although the exact mechanism is not fully understood.
We revealed the spatial overlap of Hypericin fluorescence signals and lipid rafts within the bilayer was revealed through correlative AFM and confocal imaging. In this way we revealed the spatial overlap between Hypericin fluorescence signals and lipid rafts. The diffusion of Hypericin in the bilayer was emphasized as the fluorescence signal anticorrelated with lipid rafts over time. In the absence of light, morphological effects were less pronounced, primarily altering the shape of lipid rafts to appear more rugged and fractal-like.
Nanomechanical properties of the bilayer were analyzed by measuring the Young modulus and the breakthrough force. Such experiments revealed that Hyp increases the rigidity of the bilayer, which aligns with the hypothesis mentioned earlier. This increase in rigidity was observed with and without light in the case of the Young modulus, but not in the breakthrough force experiments. This discrepancy suggests that Hyp affects the elastic (indentation) and plastic (penetration) properties of the bilayer differently.
To further characterize the effects of Hyp on the mechanical properties, we aim to test its impact on viscosity using FCS or FLIM with lipid vesicles as a model system. In fact, FLIM can be carried

on exploiting viscosity sensitive probes like Thioflavin, or Laurdan. However, such delicate measurements needs to be implemented in a glass substrate that we can hardly use with bilayers.

Experimental data on heat-inactivated SARS-CoV-2 viral particles revealed some insights about their structure. The mechanical fatigue experiments hinted at the virus's highly adaptable structure, commonly associated with highly infectious viruses. Initial nanomechanical experiments involving the application of Hypericin (Hyp) suggested the possibility of monitoring changes in the virus's stiffness, aligning with SLB breakthrough measurements. However, these findings are still in the early stages, and there is uncertainties arise from the impact of heat inactivation on experimental outcomes, introducing potential heterogeneities. This factor could potentially interfere with the accuracy of the results, and it’s preventing the drawing of conclusive statements about the effects of Hyp on the virus's nanomechanical properties. Another possibility is that the heterogeneity of the sample when Hyp is involved may be due to the uneven loading of Hyp molecules on the virions.
To gain a more comprehensive understanding of the virus's behavior and the impact of Hyp, further data collection and analysis are therefore necessary.

I am confident that this work provided new insights on the antiviral activity of Hyp, and I do believe that we could contribute to the progress of the research in the context of characterizing a new effective antiviral agent.

5. Aknowledgements

The work of this thesis wouldn't have been possible without the precious help and support of my supervisors Dr. Paolo Bianchini in IIT, and Prof. Cristiano Viappiani in Parma that I greatly thank.
I would like to thank Prof. Alberto Diaspro who directs the group of Nanoscopy in IIT, where I carried out my research for most of the three years of my PhD, to Manuela for her kindness and patience and to all the technicians of the group that are always willing to help and ready to solve any issues in the lab.
During the first year my friend and colleague Dr. Eleonora Uriati helped me greatly to set the pace for my PhD. She was very supportive on so many levels and taught me many things, even though she was at a very busy stage of her PhD path. I will always be grateful to her for everything.
I would also like to thank for the fruitful collaboration and for the contribution on my work all the group in Parma, Manuela Maria Alampi, Dr. Andrea Mussini, Dr. Pietro Delcanale, and especially Prof. Stefania Abbruzzetti who always believed in me during these years. The spectroscopic measurements presented in the PART2 - Section 1 of the thesis were carried out by them at the Università di Parma. I would like to thank the virology group at IZSLER in Brescia, particularly Dr Ana Moreno Martin, for providing the SARS-CoV-2 viruses and for the inactivation measurements with Hypericin.
I am very grateful to Dr. Silvia Dante for helping me to gain expertise on the SLBs sample preparation and for the fruitful discussions about my research.
I would like to thank Prof. Cristina Flors in Madrid, for kindly hosting me in her group for a few months, and to all the members of her group, especially Dr. Patricia Pedraz and Dr. Johann Mertens that were very helpful and willing to share their knowledge and experience with me. The measurements of High-Speed AFM, as well as the measurements with the Nanotec Cervantes were performed in their lab.
These three years of PhD were a rollercoaster of emotions, and they would not have been the same without the people I met with which I shared the everyday struggles and joys as well as amazing experiences in conferences or schools. I was very lucky to meet amazing people, like Alberta, Andrea, Francesco, Simone, Fabio, Francesca, Isotta, Elena, Sabrina, Eleonora, Lisa, Chantal, Luca, Francesco, Alessandro, Giacomo, Sanket and all the many others in Nanoscopy/MMS and in IIT. I really love all of you and I will always bring with me all the best memories we had together; the trip in the van in California with Andrea and Simone stands out as one of the best experiences of my life.
Despite staying for a short time, I met some great people in Madrid that I want to thank for inspiring me in many ways and for the special connection that we built, especially Paula and Federico.

Il ringraziamento più importante va alla mia famiglia, che mi ama e mi supporta da sempre senza condizioni: i miei genitori Luca e Daniela, mio fratello Leonardo, Carla e Cristiano, i miei nonni e i miei zii, e tutti quanti i membri della mia famiglia allargata; ai miei amici di una vita e ai più nuovi, senza i quali la vita perderebbe il suo colore; e infine a Dalila che è la mia luce, il cui amore e supporto è la mia fonte di felicità più grande.

6. Bibliography

[1] M. Wainwright, T. Maisch, S. Nonell, K. Plaetzer, A. Almeida, G. P. Tegos, M. R. Hamblin, "Photoantimicrobials—are we afraid of the light?," *Lancet Infect Dis*, vol. 17, no. 2, pp. e49–e55, 2017, doi: 10.1016/S1473-3099(16)30268-7.

[2] A. Kubin, F. Wierrani, U. Burner, G. Alth, and W. Grunberger, "Hypericin - The Facts About a Controversial Agent," *Curr Pharm Des*, vol. 11, no. 2, 2005, doi: 10.2174/1381612053382287.

[3] Edinburgh Instruments, "A typical Jablonski diagram showing the possible radiative and non-radiative transitions.". Available : https://www.edinst.com/us/blog/jablonski-diagram-2/

[4] O. Raab, "Uber die wirkung fluoreszierender stoffe auf infusorien," *Zeitschr Biol*, vol. 39, pp. 524–546, 1900.

[5] M. R. Hamblin, "Photodynamic Therapy for Cancer: What's Past is Prologue," *Photochemistry and Photobiology*, vol. 96, no. 3. 2020. doi: 10.1111/php.13190.

[6] F. Cieplik, D. Deng, W. Crielaard, W. Buchalla, E. Hellwig, A. Al-Ahmad, T. Maisch, "Antimicrobial photodynamic therapy–what we know and what we don't," *Critical Reviews in Microbiology*, vol. 44, no. 5. 2018. doi: 10.1080/1040841X.2018.1467876.

[7] D. Bartusik-Aebisher, A. Żołyniak, E. Barnaś, A. Machorowska-Pieniążek, P. Oleś, A. Kawczyk-Krupka, D. Aebisher, "The Use of Photodynamic Therapy in the Treatment of Brain Tumors—A Review of the Literature," *Molecules*, vol. 27, no. 20. 2022. doi: 10.3390/molecules27206847.

[8] R. V. Huis in 't Veld, J. Heuts, S. Ma, L. J. Cruz, F. A. Ossendorp, and M. J. Jager, "Current Challenges and Opportunities of Photodynamic Therapy against Cancer," *Pharmaceutics*, vol. 15, no. 2. 2023. doi: 10.3390/pharmaceutics15020330.

[9] D. Pezzuoli, M. Cozzolino, C. Montali, L. Brancaleon, P. Bianchini, M. Zantedeschi, S. Bonardi, C. Viappiani, S. Abbruzzetti, "Serum albumins are efficient delivery systems for the photosensitizer hypericin in photosensitization-based treatments against Staphylococcus aureus," *Food Control*, vol. 94, pp. 254–262, Dec. 2018, doi: 10.1016/j.foodcont.2018.07.027.

[10] F. Wilkinson, W. P. Helman, and A. B. Ross, "Rate Constants for the Decay and Reactions of the Lowest Electronically Excited Singlet State of Molecular Oxygen in Solution. An Expanded and Revised Compilation," *J Phys Chem Ref Data*, vol. 24, no. 2, 1995, doi: 10.1063/1.555965.

[11] C. Schweitzer and R. Schmidt, "Physical mechanisms of generation and deactivation of singlet oxygen," *Chem Rev*, vol. 103, no. 5, 2003, doi: 10.1021/cr010371d.

[12] J. Sandland and R. W. Boyle, "Photosensitizer Antibody-Drug Conjugates: Past, Present, and Future," *Bioconjug Chem*, vol. 30, no. 4, 2019, doi: 10.1021/acs.bioconjchem.9b00055.

[13] M. Warszyńska, P. Repetowski, and J. M. Dąbrowski, “Photodynamic therapy combined with immunotherapy: Recent advances and future research directions,” *Coordination Chemistry Reviews*, vol. 495. 2023. doi: 10.1016/j.ccr.2023.215350.

[14] G. Shafirstein, A. Battoo, K. Harris, H. Baumann, S.O. Gollnick, J. Lindenmann, C.E. Nwogu, “Photodynamic therapy of non-small cell lung cancer narrative review and future directions,” *Annals of the American Thoracic Society*, vol. 13, no. 2. 2016. doi: 10.1513/AnnalsATS.201509-650FR.

[15] A. P. Castano, P. Mroz, and M. R. Hamblin, “Photodynamic therapy and anti-tumour immunity,” *Nature Reviews Cancer*, vol. 6, no. 7. 2006. doi: 10.1038/nrc1894.

[16] I. Mellman, G. Coukos, and G. Dranoff, “Cancer immunotherapy comes of age,” *Nature*, vol. 480, no. 7378. 2011. doi: 10.1038/nature10673.

[17] S. Farkona, E. P. Diamandis, and I. M. Blasutig, “Cancer immunotherapy: The beginning of the end of cancer?,” *BMC Medicine*, vol. 14, no. 1. 2016. doi: 10.1186/s12916-016-0623-5.

[18] M. Darvishi, F. Tosan, P. Nakhaei, D. A. Manjili, S. A. Kharkouei, A. Alizadeh, S. Ilkhani, F. Khalafi, F. A. Zadeh, S-G. Shafagh, “Recent progress in cancer immunotherapy: Overview of current status and challenges,” *Pathology Research and Practice*, vol. 241. 2023. doi: 10.1016/j.prp.2022.154241.

[19] P. Delcanale, S. Abbruzzetti, and C. Viappiani, “Photodynamic treatment of pathogens,” *Rivista del Nuovo Cimento*, vol. 45, no. 6, pp. 407–459, Jun. 2022, doi: 10.1007/s40766-022-00031-4.

[20] A. Wiehe, J. M. O’brien, and M. O. Senge, “Trends and targets in antiviral phototherapy,” *Photochemical and Photobiological Sciences*, vol. 18, no. 11, 2019, doi: 10.1039/c9pp00211a.

[21] J. Arentz and H. J. von der Heide, “Evaluation of methylene blue based photodynamic inactivation (PDI) against intracellular B-CoV and SARS-CoV2 viruses under different light sources in vitro as a basis for new local treatment strategies in the early phase of a Covid19 infection,” *Photodiagnosis Photodyn Ther*, vol. 37, 2022, doi: 10.1016/j.pdpdt.2021.102642.

[22] “W.H. Organization, Guidelines on viral inactivation and removal procedures intended to assure the viral safety of human blood plasma products,” *WHO technical report series*, vol. 924. 2004.

[23] J. A. Willis, V. Cheburkanov, G. Kassab, J.M. Soares, K.C. Blanco, V.S. Bagnato, V.V. Yakovlev, “Photodynamic viral inactivation: Recent advances and potential applications,” *Applied Physics Reviews*, vol. 8, no. 2. 2021. doi: 10.1063/5.0044713.

[24] V. V. Zverev, O.V. Makarov, A.Z. Khashukoeva, O.A. Svitich, Y.E. Dobrokhotova, E.A. Markova, P.A. Labginov, S.A. Khlinova, E.A. Shulenina, and L.V. Gankovskaya, "In vitro studies of the antiherpetic effect of photodynamic therapy," *Lasers Med Sci*, vol. 31, no. 5, 2016, doi: 10.1007/s10103-016-1912-0.

[25] S. Teitelbaum, L. H. Azevedo, and W. E. Bernaola-Paredes, "Antimicrobial Photodynamic Therapy Used as First Choice to Treat Herpes Zoster Virus Infection in Younger Patient: A Case Report," *Photobiomodul Photomed Laser Surg*, vol. 38, no. 4, 2020, doi: 10.1089/photob.2019.4725.

[26] G. B. Kharkwal, S. K. Sharma, Y. Y. Huang, T. Dai, and M. R. Hamblin, "Photodynamic therapy for infections: Clinical applications," *Lasers in Surgery and Medicine*, vol. 43, no. 7. 2011. doi: 10.1002/lsm.21080.

[27] E. Alves, M. A. F. Faustino, M. G. P. M. S. Neves, Â. Cunha, H. Nadais, and A. Almeida, "Potential applications of porphyrins in photodynamic inactivation beyond the medical scope," *Journal of Photochemistry and Photobiology C: Photochemistry Reviews*, vol. 22. 2015. doi: 10.1016/j.jphotochemrev.2014.09.003.

[28] M. Cossu, L. Ledda, and A. Cossu, "Emerging trends in the photodynamic inactivation (PDI) applied to the food decontamination," *Food Research International*, vol. 144. 2021. doi: 10.1016/j.foodres.2021.110358.

[29] A. A. Foggiato, A. S. Garcez, A. Fuziy, and D. F. Silva, "Photodynamic therapy: alternative in decontamination of surfaces," 2020. doi: 10.1117/12.2542918.

[30] D. W. Kimberlin and R. J. Whitley, "Antiviral resistance: Mechanisms, clinical significance, and future implications," *Journal of Antimicrobial Chemotherapy*, vol. 37, no. 3. 1996. doi: 10.1093/jac/37.3.403.

[31] K. K. Irwin, N. Renzette, T. F. Kowalik, and J. D. Jensen, "Antiviral drug resistance as an adaptive process," *Virus Evol*, vol. 2, no. 1, 2016, doi: 10.1093/ve/vew014.

[32] Y. Y. Huang, M. Tanaka, D. Vecchio, M. Garcia-Diaz, J. Chang, Y. Morimoto, and M. R. Hamblin, "Photodynamic therapy induces an immune response against a bacterial pathogen," *Expert Review of Clinical Immunology*, vol. 8, no. 5. 2012. doi: 10.1586/eci.12.37.

[33] E. Reginato, "Immune response after photodynamic therapy increases anti-cancer and anti-bacterial effects," *World J Immunol*, vol. 4, no. 1, 2014, doi: 10.5411/wji.v4.i1.1.

[34] P. Delcanale, E. Uriati, M. Mariangeli, A. Mussini, A. Moreno, D. Lelli, L. Cavanna, P. Bianchini, A. Diaspro, S. Abbruzzetti, and C. Viappiani, "The Interaction of Hypericin with SARS-CoV-2 Reveals a Multimodal Antiviral Activity," *ACS Appl Mater Interfaces*, vol. 14, no. 12, pp. 14025–14032, Mar. 2022, doi: 10.1021/acsami.1c22439.

[35] P. Delcanale, F. Pennacchietti, G. Maestrini, B. Rodríguez-Amigo, P. Bianchini, A. Diaspro, A.o Iagatti, B. Patrizi, P. Foggi, M. Agut, S. Nonell, S. Abbruzzetti & C. Viappiani, "Subdiffraction localization of a nanostructured photosensitizer in bacterial cells," *Sci Rep*, vol. 5, 2015, doi: 10.1038/srep15564.

[36] M. Woźniak and M. Nowak-Perlak, "Hypericin-Based Photodynamic Therapy Displays Higher Selectivity and Phototoxicity towards Melanoma and Squamous Cell Cancer Compared to Normal Keratinocytes In Vitro," *Int J Mol Sci*, vol. 24, no. 23, Dec. 2023, doi: 10.3390/ijms242316897.

[37] N. Choudhary, T. E. Collignon, D. Tewari, and A. Bishayee, "Hypericin and its anticancer effects: From mechanism of action to potential therapeutic application," *Phytomedicine*, vol. 105. 2022. doi: 10.1016/j.phymed.2022.154356.

[38] J. nan Zhang, F. Zhang, Q. juan Tang, C. shan Xu, and X. hong Meng, "Effect of photodynamic inactivation of Escherichia coli by hypericin," *World J Microbiol Biotechnol*, vol. 34, no. 7, 2018, doi: 10.1007/s11274-018-2464-1.

[39] N. Kashef, Y. S. Borghei, and G. E. Djavid, "Photodynamic effect of hypericin on the microorganisms and primary human fibroblasts," *Photodiagnosis Photodyn Ther*, vol. 10, no. 2, 2013, doi: 10.1016/j.pdpdt.2012.11.007.

[40] L. Souza Amaral, A. Orzari Ribeiro, and J. Rodrigues Perussi, "Evidence of hypericin photoinactivation of E. faecalis: From planktonic culture to mammalian cells selectivity up to biofilm disruption," *Photodiagnosis Photodyn Ther*, vol. 31, 2020, doi: 10.1016/j.pdpdt.2020.101759.

[41] J. B. Hudson', I. Lopez-Bazzocchf, and G. H. N. Towers, "Antiviral activities of hypericin," 1991.

[42] J. B. Hudson, L. Harris, and G. H. N. Towers, "The importance of light in the anti-HIV effect of hypericin," 1993.

[43] P. Miskovsky, "Hypericin - A New Antiviral and Antitumor Photosensitizer: Mechanism of Action and Interaction with Biological Macromolecules," *Curr Drug Targets*, vol. 3, no. 1, 2005, doi: 10.2174/1389450023348091.

[44] J. Lenard, A. Rabson, and R. Vanderoef, "Photodynamic inactivation of infectivity of human immunodeficiency virus and other enveloped viruses using hypericin and rose bengal: Inhibition of fusion and syncytia formation," *Proc Natl Acad Sci U S A*, vol. 90, no. 1, 1993, doi: 10.1073/pnas.90.1.158.

[45] E. S. E. Eriksson, D. J. V. A. dos Santos, R. C. Guedes, and L. A. Eriksson, "Properties and permeability of hypericin and brominated hypericin in lipid membranes," *J Chem Theory Comput*, vol. 5, no. 12, 2009, doi: 10.1021/ct9002702.

[46] Y. F. Ho, M. H. Wu, B. H. Cheng, Y. W. Chen, and M. C. Shih, "Lipid-mediated preferential localization of hypericin in lipid membranes," *Biochim Biophys Acta Biomembr*, vol. 1788, no. 6, pp. 1287–1295, Jun. 2009, doi: 10.1016/j.bbamem.2009.01.017.

[47] T. Singhal, “A Review of Coronavirus Disease-2019 (COVID-19),” *Indian Journal of Pediatrics*, vol. 87, no. 4. 2020. doi: 10.1007/s12098-020-03263-6.

[48] F. Li, “Structure, Function, and Evolution of Coronavirus Spike Proteins,” *Annual Review of Virology*, vol. 3. 2016. doi: 10.1146/annurev-virology-110615-042301.

[49] A. E. Gorbalenya, S. C. baker , R. S. Baric , R. J. de Groot , C. Drosten, A. A. Gulyaeva, B. l. Haagmans , C. Lauber , A. M. Leontovich , B. W. Neuman, D. Penzar, S. Perlman, L. l. M. Poon, D. V. Samborskiy, I. A. Sidorov, I. Sola and J. Ziebuhr, “The species Severe acute respiratory syndrome-related coronavirus: classifying 2019-nCoV and naming it SARS-CoV-2,” *Nature Microbiology*, vol. 5, no. 4. 2020. doi: 10.1038/s41564-020-0695-z.

[50] C. Sohrabi, Z. Alsafi, N. O'Neill, M. Khan, A. Kerwan, A. Al-Jabir, C. Iosifidis, and R. Aghad, “World Health Organization declares global emergency: A review of the 2019 novel coronavirus (COVID-19),” *International Journal of Surgery*, vol. 76. 2020. doi: 10.1016/j.ijsu.2020.02.034.

[51] B. Malone, N. Urakova, E. J. Snijder, and E. A. Campbell, “Structures and functions of coronavirus replication-transcription complexes and their relevance for SARS-CoV-2 drug design.,” *Nat Rev Mol Cell Biol*, vol. 23, no. 1, pp. 21–39, Jan. 2022, doi: 10.1038/s41580-021-00432-z.

[52] V. B. O’donnell, V. B. O’Donnell, D. Thomas, R. Stanton, J-Y. Maillard, R. C. Murphy, S. A. Jones, I. Humphreys, M.J.O. Wakelam, C. Fegan, M.P. Wise, A. Bosch, S. A. Sattar, “Potential Role of Oral Rinses Targeting the Viral Lipid Envelope in SARS-CoV-2 Infection,” *Function*, vol. 1, no. 1. Oxford University Press, 2020. doi: 10.1093/function/zqaa002.

[53] D. Wrapp, N. Wang, K. S. Corbett, J. A. Goldsmith, C-L. Hsieh, O. Abiona, B. S. Graham, and J. S. McLellan, “Cryo-EM structure of the 2019-nCoV spike in the prefusion conformation,” *Science (1979)*, vol. 367, no. 6483, 2020, doi: 10.1126/science.aax0902.

[54] M. Hoffmann, H. Kleine-Weber, S. Schroeder, N. Krüger, T. Herrler, S. Erichsen, T. S. Schiergens, G. Herrler, N-H. Wu, A. Nitsche, M. A. Müller, C. Drosten, S. Pöhlmann, “SARS-CoV-2 Cell Entry Depends on ACE2 and TMPRSS2 and Is Blocked by a Clinically Proven Protease Inhibitor,” *Cell*, vol. 181, no. 2, 2020, doi: 10.1016/j.cell.2020.02.052.

[55] Y. Huang, C. Yang, X. feng Xu, W. Xu, and S. wen Liu, “Structural and functional properties of SARS-CoV-2 spike protein: potential antivirus drug development for COVID-19,” *Acta Pharmacologica Sinica*, vol. 41, no. 9. 2020. doi: 10.1038/s41401-020-0485-4.

[56] E. T. Castellana and P. S. Cremer, “Solid supported lipid bilayers: From biophysical studies to sensor design,” *Surface Science Reports*, vol. 61, no. 10. 2006. doi: 10.1016/j.surfrep.2006.06.001.

[57] L. K. Tamm and H. M. McConnell, “Supported phospholipid bilayers,” *Biophys J*, vol. 47, no. 1, 1985, doi: 10.1016/S0006-3495(85)83882-0.

[58] G. M'Baye, Y. Mély, G. Duportail, and A. S. Klymchenko, "Liquid ordered and gel phases of lipid bilayers: Fluorescent probes reveal close fluidity but different hydration," *Biophys J*, vol. 95, no. 3, 2008, doi: 10.1529/biophysj.107.127480.

[59] R. Oropesa-Nuñez, S. Seghezza, S. Dante, A. Diaspro, R. Cascella, C. Cecchi, M. Stefani, F. Chiti, and C. Canale, "Interaction of toxic and non-toxic HypF-N oligomers with lipid bilayers investigated at high resolution with atomic force microscopy," *Oncotarget*, vol. 7, no. 29, 2016, doi: 10.18632/oncotarget.10449.

[60] L. Redondo-Morata, M. I. Giannotti, and F. Sanz, "Influence of cholesterol on the phase transition of lipid bilayers: A temperature-controlled force spectroscopy study," *Langmuir*, vol. 28, no. 35, 2012, doi: 10.1021/la302620t.

[61] K. Simons and E. Ikonen, "Functional rafts in cell membranes," *Nature*, vol. 387, no. 6633. pp. 569–572, Jun. 05, 1997. doi: 10.1038/42408.

[62] D. A. Brown and E. London, "Functions of lipid rafts in biological membranes," *Annual Review of Cell and Developmental Biology*, vol. 14. 1998. doi: 10.1146/annurev.cellbio.14.1.111.

[63] "https://en.wikipedia.org/wiki/Airy_disk".

[64] E. Abbe, "Beiträge zur Theorie des Mikroskops und der mikroskopischen Wahrnehmung," *Archiv für Mikroskopische Anatomie*, vol. 9, no. 1, 1873, doi: 10.1007/bf02956173.

[65] Rayleigh, " XXXI. Investigations in optics, with special reference to the spectroscope ," *The London, Edinburgh, and Dublin Philosophical Magazine and Journal of Science*, vol. 8, no. 49, 1879, doi: 10.1080/14786447908639684.

[66] "https://en.wikipedia.org/wiki/Fluorescence_microscope".

[67] C. J. R. Sheppard and A. Choudhury, "Image formation in the scanning microscope," *Opt Acta (Lond)*, vol. 24, no. 10, 1977, doi: 10.1080/713819421.

[68] A. ed Diaspro, *Confocal and Two-Photon Microscopy: Foundations, Applications and Advances*. Wiley, 2001.

[69] T. Wilson, "Resolution and optical sectioning in the confocal microscope," *Journal of Microscopy*, vol. 244, no. 2. 2011. doi: 10.1111/j.1365-2818.2011.03549.x.

[70] C. J. R. Sheppard and T. Wilson, "Imaging properties of annular lenses," *Appl Opt*, vol. 18, no. 22, 1979, doi: 10.1364/ao.18.003764.

[71] C. J. R. Sheppard and M. Gu, "Improvement of axial resolution in confocal microscopy using an annular pupil," *Opt Commun*, vol. 84, no. 1–2, 1991, doi: 10.1016/0030-4018(91)90019-A.

[72] G. Tortarolo, A. Zunino, F. Fersini, M. Castello, S. Piazza, C. J. R. Sheppard, P. Bianchini, A. Diaspro, S. Koho, and G. Vicidomini "Focus image scanning microscopy for sharp and gentle super-resolved microscopy," *Nat Commun*, vol. 13, no. 1, 2022, doi: 10.1038/s41467-022-35333-y.

[73] "https://www.britannica.com/technology/microscope/Confocal-microscopes".

[74] A. Diaspro ed., *Nanoscopy and Multidimensional Optical Fluorescence Microscopy*. Chapman and Hall/CRC, 2010.

[75] E. Betzig, E. Betzig, G. H. Patterson, R. Sougrat, O. W. Lindwasser, S. Olenych, J. S. Bonifacino, M. W. Davidson, J. Lippincott-Schwartz, and H. F. Hess, "Imaging intracellular fluorescent proteins at nanometer resolution," *Science (1979)*, vol. 313, no. 5793, 2006, doi: 10.1126/science.1127344.

[76] M. J. Rust, M. Bates, and X. Zhuang, "Sub-diffraction-limit imaging by stochastic optical reconstruction microscopy (STORM)," *Nat Methods*, vol. 3, no. 10, 2006, doi: 10.1038/nmeth929.

[77] S. T. Hess, T. P. K. Girirajan, and M. D. Mason, "Ultra-high resolution imaging by fluorescence photoactivation localization microscopy," *Biophys J*, vol. 91, no. 11, 2006, doi: 10.1529/biophysj.106.091116.

[78] S. W. Hell and J. Wichmann, "Breaking the diffraction resolution limit by stimulated emission: stimulated-emission-depletion fluorescence microscopy," *Opt Lett*, vol. 19, no. 11, p. 780, Jun. 1994, doi: 10.1364/OL.19.000780.

[79] M. G. L. Gustafsson, "Nonlinear structured-illumination microscopy: Wide-field fluorescence imaging with theoretically unlimited resolution," *Proc Natl Acad Sci U S A*, vol. 102, no. 37, 2005, doi: 10.1073/pnas.0406877102.

[80] "https://www.nobelprize.org/prizes/chemistry/2014/summary/."

[81] "https://angtech.com/2022/12/18/understanding-absorption-emission-and-excitation-in-fluorescence/."

[82] S. Galiani, B. Harke, G. Vicidomini, G. Lignani, F. Benfenati, A. Diaspro, and P. Bianchini, "Strategies to maximize the performance of a STED microscope," *Opt Express*, vol. 20, no. 7, 2012, doi: 10.1364/oe.20.007362.

[83] K. Hiersemenzel, E. R. Brown, and R. R. Duncan, "Imaging large cohorts of single ion channels and their activity," *Frontiers in Endocrinology*, vol. 4, no. SEP. 2013. doi: 10.3389/fendo.2013.00114.

[84] D. Magde, E. Elson, and W. W. Webb, "Thermodynamic fluctuations in a reacting system measurement by fluorescence correlation spectroscopy," *Phys Rev Lett*, vol. 29, no. 11, 1972, doi: 10.1103/PhysRevLett.29.705.

[85] L. Yu, Y. Lei, Y. Ma, M. Liu, J. Zheng, D. Dan, and P. Gao, "A Comprehensive Review of Fluorescence Correlation Spectroscopy," *Frontiers in Physics*, vol. 9. 2021. doi: 10.3389/fphy.2021.644450.

[86] G. Binnig and H. Rohrer, "Scanning tunneling microscopy," *Surf Sci*, vol. 126, no. 1–3, 1983, doi: 10.1016/0039-6028(83)90716-1.

[87] "https://www.nobelprize.org/prizes/physics/1986/press-release/."

[88] G. Binnig, C. F. Quate' ', E. L. Gi, and C. Gerber, "Atomic Force Microscope."

[89] G. Binnig, C. Gerber, E. Stoll, T. R. Albrecht, and C. F. Quate, "Atomic resolution with atomic force microscope," *Surf Sci*, vol. 189–190, no. C, 1987, doi: 10.1016/S0039-6028(87)80407-7.

[90] M. Pfreundschuh, D. Martinez-Martin, E. Mulvihill, S. Wegmann, and D. J. Muller, "Multiparametric high-resolution imaging of native proteins by force-distance curve-based AFM," *Nat Protoc*, vol. 9, no. 5, 2014, doi: 10.1038/nprot.2014.070.

[91] B. Harke, J. V. Chacko, H. Haschke, C. Canale, and A. Diaspro, "A novel nanoscopic tool by combining AFM with STED microscopy," 2012. [Online]. Available: http://www.optnano.com/content/1/1/3

[92] E. I. Goksu, J. M. Vanegas, C. D. Blanchette, W. C. Lin, and M. L. Longo, "AFM for structure and dynamics of biomembranes," *Biochimica et Biophysica Acta - Biomembranes*, vol. 1788, no. 1. pp. 254–266, Jan. 2009. doi: 10.1016/j.bbamem.2008.08.021.

[93] C. Canale, M. Jacono, A. Diaspro, and S. Dante, "Force spectroscopy as a tool to investigate the properties of supported lipid membranes," *Microsc Res Tech*, vol. 73, no. 10, pp. 965–972, 2010, doi: 10.1002/jemt.20834.

[94] H. M. Wu, Y. H. Lin, T. C. Yen, and C. L. Hsieh, "Nanoscopic substructures of raft-mimetic liquid-ordered membrane domains revealed by high-speed single-particle tracking," *Sci Rep*, vol. 6, 2016, doi: 10.1038/srep20542.

[95] T. Logan, J. Bendor, C. Toupin, K. Thorn, and R. H. Edwards, "α-Synuclein promotes dilation of the exocytotic fusion pore," *Nat Neurosci*, vol. 20, no. 5, pp. 681–689, May 2017, doi: 10.1038/nn.4529.

[96] Á. Zolcsák, T. Bozo, B. Kiss, J. Somkuti, M. S. Kellermayer, and L. Herenyi, "Structural and nanomechanical assessment of photosensitization induced membrane disruption," *Biophys J*, vol. 121, no. 3, 2022, doi: 10.1016/j.bpj.2021.11.912.

[97] P. D. Garcia, C. R. Guerrero, and R. Garcia, "Nanorheology of living cells measured by AFM-based force-distance curves," *Nanoscale*, vol. 12, no. 16, pp. 9133–9143, Apr. 2020, doi: 10.1039/c9nr10316c.

[98] J. W. Harding and I. N. Sneddon, "The elastic stresses produced by the indentation of the plane surface of a semi-infinite elastic solid by a rigid punch," *Mathematical Proceedings of the Cambridge Philosophical Society*, vol. 41, no. 1, 1945, doi: 10.1017/S0305004100022325.

[99] I. N. Sneddon, "The relation between load and penetration in the axisymmetric boussinesq problem for a punch of arbitrary profile," *Int J Eng Sci*, vol. 3, no. 1, 1965, doi: 10.1016/0020-7225(65)90019-4.

[100] A. Renger, "Johnson, K. L., Contact Mechanics. Cambridge etc., Cambridge University Press 1985. XII, 452 pp., £ 17.50 P/B. ISBN 0521347963," *ZAMM - Journal of Applied Mathematics and Mechanics / Zeitschrift für Angewandte Mathematik und Mechanik*, vol. 69, no. 7, 1989, doi: 10.1002/zamm.19890690713.

[101] O. Et-Thakafy, F. Guyomarc'h, and C. Lopez, "Young modulus of supported lipid membranes containing milk sphingomyelin in the gel, fluid or liquid-ordered phase, determined using AFM force spectroscopy," *Biochim Biophys Acta Biomembr*, vol. 1861, no. 9, pp. 1523–1532, Sep. 2019, doi: 10.1016/j.bbamem.2019.07.005.

[102] R. Garcia, "Nanomechanical mapping of soft materials with the atomic force microscope: Methods, theory and applications," *Chemical Society Reviews*, vol. 49, no. 16. Royal Society of Chemistry, pp. 5850–5884, Aug. 21, 2020. doi: 10.1039/d0cs00318b.

[103] G. N. Greaves, A. L. Greer, R. S. Lakes, and T. Rouxel, "Poisson's ratio and modern materials," *Nature Materials*, vol. 10, no. 11. 2011. doi: 10.1038/nmat3134.

[104] N. Gavara and R. S. Chadwick, "Determination of the elastic moduli of thin samples and adherent cells using conical atomic force microscope tips," *Nat Nanotechnol*, vol. 7, no. 11, 2012, doi: 10.1038/nnano.2012.163.

[105] E. K. Dimitriadis, F. Horkay, J. Maresca, B. Kachar, and R. S. Chadwick, "Determination of elastic moduli of thin layers of soft material using the atomic force microscope," *Biophys J*, vol. 82, no. 5, 2002, doi: 10.1016/S0006-3495(02)75620-8.

[106] S. Chiodini, S. Ruiz-Rincón, P. D. Garcia, S. Martin, K. Kettelhoit, I. Armenia, D. B. Werz, P. Cea, "Bottom Effect in Atomic Force Microscopy Nanomechanics," *Small*, vol. 16, no. 35, 2020, doi: 10.1002/smll.202000269.

[107] P. D. Garcia and R. Garcia, "Determination of the Elastic Moduli of a Single Cell Cultured on a Rigid Support by Force Microscopy," *Biophys J*, vol. 114, no. 12, pp. 2923–2932, Jun. 2018, doi: 10.1016/j.bpj.2018.05.012.

[108] L. Chopinet, C. Formosa, M. P. Rols, R. E. Duval, and E. Dague, "Imaging living cells surface and quantifying its properties at high resolution using AFM in QI^{TM} mode," *Micron*, vol. 48, 2013, doi: 10.1016/j.micron.2013.02.003.

[109] V. Franz, S. Loi, H. Mü Ller, E. Bamberg, and H.-J. Rgen Butt, "Tip penetration through lipid bilayers in atomic force microscopy," 2002. [Online]. Available: www.elsevier.com/locate/colsurfb

[110] S. Loi, G. Sun, V. Franz, and H. J. Butt, "Rupture of molecular thin films observed in atomic force microscopy. II. Experiment," *Phys Rev E Stat Phys Plasmas Fluids Relat Interdiscip Topics*, vol. 66, no. 3, 2002, doi: 10.1103/PhysRevE.66.031602.

[111] S. Seghezza, A. Diaspro, C. Canale, and S. Dante, "Cholesterol drives Aβ(1-42) interaction with lipid rafts in model membranes," *Langmuir*, vol. 30, no. 46, pp. 13934–13941, Nov. 2014, doi: 10.1021/la502966m.

[112] T. Miyatani, M. Horii, A. Rosa, M. Fujihira, and O. Marti, "Mapping of electrical double-layer force between tip and sample surfaces in water with pulsed-force-mode atomic force microscopy," *Appl Phys Lett*, vol. 71, no. 18, 1997, doi: 10.1063/1.120162.

[113] P. J. De Pablo, J. Colchero, J. Gómez-Herrero, and A. M. Baró, "Jumping mode scanning force microscopy," *Appl Phys Lett*, vol. 73, no. 22, 1998, doi: 10.1063/1.122751.

[114] F. Moreno-Herrero, P. J. De Pablo, M. Álvarez, J. Colchero, J. Gómez-Herrero, and A. M. Baró, "Jumping mode scanning force microscopy: A suitable technique for imaging DNA in liquids," in *Applied Surface Science*, 2003. doi: 10.1016/S0169-4332(02)01473-3.

[115] F. Moreno-Madrid, N. Martín-González, A. Llauró, A. Ortega-Esteban, M. Hernando-Pérez, T. Douglas, I. A.T. Schaap, P. J. de Pablo, "Atomic force microscopy of virus shells," *Biochemical Society Transactions*, vol. 45, no. 2. 2017. doi: 10.1042/BST20160316.

[116] P. J. de Pablo, "Atomic force microscopy of virus shells," *Seminars in Cell and Developmental Biology*, vol. 73. 2018. doi: 10.1016/j.semcdb.2017.08.039.

[117] P. J. de Pablo, "The application of atomic force microscopy for viruses and protein shells: Imaging and spectroscopy," in *Advances in Virus Research*, vol. 105, 2019. doi: 10.1016/bs.aivir.2019.07.006.

[118] F. Moreno-Herrero, J. Colchero, J. Gómez-Herrero, and A. M. Baro, "Atomic force microscopy contact, tapping, and jumping modes for imaging biological samples in liquids," *Phys Rev E Stat Nonlin Soft Matter Phys*, vol. 69, no. 3 1, 2004, doi: 10.1103/PhysRevE.69.031915.

[119] I. Gözen, P. Dommersnes, I. Czolkos, A. Jesorka, T. Lobovkina, and O. Orwar, "Fractal avalanche ruptures in biological membranes," *Nat Mater*, vol. 9, no. 11, 2010, doi: 10.1038/nmat2854.

[120] T. Shigematsu, K. Koshiyama, and S. Wada, "Effects of stretching speed on mechanical rupture of phospholipid/cholesterol bilayers: Molecular dynamics simulation," *Sci Rep*, vol. 5, 2015, doi: 10.1038/srep15369.

[121] H. Prinz, "Hill coefficients, dose-response curves and allosteric mechanisms," *J Chem Biol*, vol. 3, no. 1, 2010, doi: 10.1007/s12154-009-0029-3.

[122] R. R. Neubig, M. Spedding, T. Kenakin, and A. Christopoulos, "International Union of Pharmacology Committee on Receptor Nomenclature and Drug Classification. XXXVIII. Update on Terms and Symbols in Quantitative Pharmacology," *Pharmacological Reviews*, vol. 55, no. 4. 2003. doi: 10.1124/pr.55.4.4.

[123] Benoit. B. Mandelbrot, *The Fractal Geometry of Nature*. W. H. Freeman and Co., 1982.

[124] B. B. Mandelbrot, "Stochastic models for the Earth's relief, the shape and the fractal dimension of the coastlines, and the number area rule for islands," *Proc Natl Acad Sci U S A*, vol. 72, no. 10, 1975, doi: 10.1073/pnas.72.10.3825.

[125] I. J. Good and B. B. Mandelbrot, "Fractals: Form, Chance, and Dimension.," *J Am Stat Assoc*, vol. 73, no. 362, 1978, doi: 10.2307/2286682.

[126] G. Gonzato, "A practical implementation of the box counting algorithm," *Comput Geosci*, vol. 24, no. 1, 1998, doi: 10.1016/S0098-3004(97)00137-4.

[127] A. Maria and S. Carey, "Using fractal analysis to quantitatively characterize the shapes of volcanic particles," *J Geophys Res Solid Earth*, vol. 107, no. B11, Nov. 2002, doi: 10.1029/2001jb000822.

[128] I. Pilgrim and R. P. Taylor, “Fractal Analysis of Time-Series Data Sets: Methods and Challenges,” in *Fractal Analysis*, S.-A. Ouadfeul, Ed., Rijeka: IntechOpen, 2018. doi: 10.5772/intechopen.81958.

[129] A. Monserrate, S. Casado, and C. Flors, “Correlative atomic force microscopy and localization-based super-resolution microscopy: Revealing labelling and image reconstruction artefacts,” *ChemPhysChem*, vol. 15, no. 4, 2014, doi: 10.1002/cphc.201300853.

[130] A. Amara and J. Mercer, “Viral apoptotic mimicry,” *Nat Rev Microbiol*, vol. 13, no. 8, pp. 461–469, Jul. 2015, doi: 10.1038/nrmicro3469.

[131] S. Chiantia, N. Kahya, J. Ries, and P. Schwille, “Effects of ceramide on liquid-ordered domains investigated by simultaneous AFM and FCS,” *Biophys J*, vol. 90, no. 12, pp. 4500–4508, 2006, doi: 10.1529/biophysj.106.081026.

[132] S. Chiantia, J. Ries, N. Kahya, and P. Schwille, “Combined AFM and two-focus SFCS study of raft-exhibiting model membranes,” *ChemPhysChem*, vol. 7, no. 11, pp. 2409–2418, Nov. 2006, doi: 10.1002/cphc.200600464.

[133] S. Chiantia, J. Ries, G. Chwastek, D. Carrer, Z. Li, R. Bittman, P. Schwille, “Role of ceramide in membrane protein organization investigated by combined AFM and FCS,” *Biochim Biophys Acta Biomembr*, vol. 1778, no. 5, pp. 1356–1364, May 2008, doi: 10.1016/j.bbamem.2008.02.008.

[134] A. Honigmann, C. Walter, F. Erdmann, C. Eggeling, and R. Wagner, “Characterization of horizontal lipid bilayers as a model system to study lipid phase separation,” *Biophys J*, vol. 98, no. 12, pp. 2886–2894, Jun. 2010, doi: 10.1016/j.bpj.2010.03.033.

[135] M. S. El-Bahrawi, N. N. Nagib, S. A. Khodier, and H. M. Sidki, “Birefringence of muscovite mica,” *Opt Laser Technol*, vol. 30, no. 6, 1998, doi: 10.1016/S0030-3992(98)00074-7.

[136] J. Ries, S. Chiantia, and P. Schwille, “Accurate determination of membrane dynamics with line-scan FCS,” *Biophys J*, vol. 96, no. 5, pp. 1999–2008, 2009, doi: 10.1016/j.bpj.2008.12.3888.

[137] A. Honigmann, V. Mueller, S. W. Hell, and C. Eggeling, “STED microscopy detects and quantifies liquid phase separation in lipid membranes using a new far-red emitting fluorescent phosphoglycerolipid analogue,” *Faraday Discuss*, vol. 161, pp. 77–89, Dec. 2012, doi: 10.1039/c2fd20107k.

[138] J. Korlach, P. Schwille, W. W. Webb, and G. W. Feigenson, “Characterization of lipid bilayer phases by confocal microscopy and fluorescence correlation spectroscopy,” *Proc Natl Acad Sci U S A*, vol. 96, no. 15, 1999, doi: 10.1073/pnas.96.15.8461.

[139] J. Ries and P. Schwille, “New concepts for fluorescence correlation spectroscopy on membranes,” *Physical Chemistry Chemical Physics*, vol. 10, no. 24. 2008. doi: 10.1039/b718132a.

[140] Q. Ruan, M. A. Cheng, M. Levi, E. Gratton, and W. W. Mantulin, “Spatial-temporal studies of membrane dynamics: Scanning fluorescence correlation spectroscopy (SFCS),” *Biophys J*, vol. 87, no. 2, 2004, doi: 10.1529/biophysj.103.036483.

[141] P. Schwille, J. Korlach, and W. W. Webb, “Fluorescence correlation spectroscopy with single-molecule sensitivity on cell and model membranes,” *Cytometry*, vol. 36, no. 3, 1999, doi: 10.1002/(SICI)1097-0320(19990701)36:3<176::AID-CYTO5>3.0.CO;2-F.

[142] M. P. Mingeot-Leclercq, M. Deleu, R. Brasseur, and Y. F. Dufrêne, “Atomic force microscopy of supported lipid bilayers,” *Nat Protoc*, vol. 3, no. 10, 2008, doi: 10.1038/nprot.2008.149.

[143] R. Bellotti, G. B. Picotto, and L. Ribotta, “AFM Measurements and Tip Characterization of Nanoparticles with Different Shapes,” *Nanomanufacturing and Metrology*, vol. 5, no. 2, 2022, doi: 10.1007/s41871-022-00125-x.

[144] J. L. Hutter and J. Bechhoefer, “Calibration of atomic-force microscope tips,” *Review of Scientific Instruments*, vol. 64, no. 7, 1993, doi: 10.1063/1.1143970.

[145] I. Horcas, R. Fernández, J. M. Gómez-Rodríguez, J. Colchero, J. Gómez-Herrero, and A. M. Baro, “WSXM: A software for scanning probe microscopy and a tool for nanotechnology,” *Review of Scientific Instruments*, vol. 78, no. 1, 2007, doi: 10.1063/1.2432410.

[146] J. E. Sader, J. W. M. Chon, and P. Mulvaney, “Calibration of rectangular atomic force microscope cantilevers,” *Review of Scientific Instruments*, vol. 70, no. 10, 1999, doi: 10.1063/1.1150021.

[147] I. G. Torre, R. J. Heck, and A. M. Tarquis, “MULTIFRAC: An ImageJ plugin for multiscale characterization of 2D and 3D stack images,” *SoftwareX*, vol. 12, 2020, doi: 10.1016/j.softx.2020.100574.

[148] Y. G. Kuznetsov and A. McPherson, “Atomic Force Microscopy in Imaging of Viruses and Virus-Infected Cells,” *Microbiology and Molecular Biology Reviews*, vol. 75, no. 2, 2011, doi: 10.1128/mmbr.00041-10.

[149] C. Carrasco, A. Carreira, I. A. T. Schaap, P. A. Serena, J. Gomez-Herrero, M. G. Mateu, and P. J. de Pablo, “DNA-mediated anisotropic mechanical reinforcement of a virus,” *Proc Natl Acad Sci U S A*, vol. 103, no. 37, 2006, doi: 10.1073/pnas.0601881103.

[150] M. Hernando-Pérez, E. Pascual, M. Aznar, A. Ionel, J. R. Castón, A. Luque, J. L. Carrascosa, D. Reguera, and P. J. de Pablo, “The interplay between mechanics and stability of viral cages,” *Nanoscale*, vol. 6, no. 5, 2014, doi: 10.1039/c3nr05763a.

[151] W. H. Roos, I. Gertsman, E. R. May, C. L. Brooks, J. E. Johnson, and G. J. L. Wuite, “Mechanics of bacteriophage maturation,” *Proc Natl Acad Sci U S A*, vol. 109, no. 7, 2012, doi: 10.1073/pnas.1109590109.

[152] A. Ortega-Esteban, A. J. Pérez-Berná, R. Menéndez-Conejero, S. J. Flint, C. San Martín, and P. J. De Pablo, “Monitoring dynamics of human adenovirus disassembly induced by mechanical fatigue,” *Sci Rep*, vol. 3, 2013, doi: 10.1038/srep01434.

[153] J. Mertens, P. Bondia, C. Allende-Ballestero, J. L. Carrascosa, C. Flors, and J. R. Castón, "Mechanics of Virus-like Particles Labeled with Green Fluorescent Protein," *Biophys J*, vol. 115, no. 8, 2018, doi: 10.1016/j.bpj.2018.08.035.

[154] S. Lyonnais, M. Hénaut, A. Neyret, P. Merida, C. Cazevieille, N. Gros, C. Chable-Bessia, and D. Muriaux, "Atomic force microscopy analysis of native infectious and inactivated SARS-CoV-2 virions," *Sci Rep*, vol. 11, no. 1, Dec. 2021, doi: 10.1038/s41598-021-91371-4.

[155] R. Cardoso-Lima, P. F. N. Souza, M. I. F. Guedes, R. Santos-Oliveira, and L. M. Rebelo Alencar, "SARS-CoV-2 Unrevealed: Ultrastructural and Nanomechanical Analysis," *Langmuir*, vol. 37, no. 36, pp. 10762–10769, Sep. 2021, doi: 10.1021/acs.langmuir.1c01488.

[156] M. Cantero, D. Carlero, F. J. Chichón, J. Martín-Benito, and P. J. De Pablo, "Monitoring SARS-CoV-2 Surrogate TGEV Individual Virions Structure Survival under Harsh Physicochemical Environments," *Cells*, vol. 11, no. 11, 2022, doi: 10.3390/cells11111759.

[157] P. J. de Pablo and M. G. Mateu, "Mechanical properties of viruses," *Subcell Biochem*, vol. 68, 2013, doi: 10.1007/978-94-007-6552-8_18.

[158] N. Kol, M. Gladnikoff, D. Barlam, R. Z. Shneck, A. Rein, and I. Rousso, "Mechanical properties of murine leukemia virus particles: Effect of maturation," *Biophys J*, vol. 91, no. 2, 2006, doi: 10.1529/biophysj.105.079657.

[159] N. Kol, Y. Shi, M. Tsvitov, D. Barlam, R. Z. Shneck, M. S. Kay, and I. Rousso, "A stiffness switch in human immunodeficiency virus," *Biophys J*, vol. 92, no. 5, pp. 1777–1783, 2007, doi: 10.1529/biophysj.106.093914.

[160] A. Llauró, P. Guerra, N. Irigoyen, J. F. Rodríguez, N. Verdaguer, and P. J. De Pablo, "Mechanical stability and reversible fracture of vault particles," *Biophys J*, vol. 106, no. 3, 2014, doi: 10.1016/j.bpj.2013.12.035.